January 2018

Heat Transfer And Pressure Drop Measurements In A High-Solidity Pin-Fin Array With Variable Hole Size Incremental Impingements

Abdulqadir Sheikhmohamed

HEAT TRANSFER AND PRESSURE DROP MEASUREMENTS IN A HIGH-SOLIDITY PIN-FIN ARRAY WITH VARIABLE HOLE SIZE INCREMENTAL IMPINGEMENTS

by

Abdulqadir Sheikhmohamed
Bachelor of Science, University of North Dakota, 2014

A Thesis

Submitted to the Graduate Faculty

of the

University of North Dakota

in partial fulfillment of the requirements

for the degree of

Master of Science

Grand Forks, North Dakota

May
2018

This thesis, submitted by Abdulqadir Sheikhmoahmed in partial fulfillment of the degree of Master of Science from the University of North Dakota, has been read by the Faculty Advisory Committee under whom the work has been done and is hereby approved.

Dr. Forrest Ames

Date

Dr. Clement Tang

Date

Dr. Nanak Grewal

Date

This thesis is being submitted by the appointed advisory committee as having met all of the requirements of the School of Graduate Studies at the University of North Dakota and is hereby approved.

Dr. Grant Mcgimpsey
Dean of the School of Graduate Studies

Date

PERMISSION

Title Heat Transfer and Pressure Drop Measurements IN A High-Solidity Pin-Fin Array with Variable Hole Size Incremental Impingements

Department Mechanical Engineering

Degree Master of Science

In presenting this thesis in partial fulfillment of the requirements for a graduate degree from the University of North Dakota, I agree that the library of the University shall make it freely available for inspection. I further agree that the permission for extensive copying for scholarly purposes may granted by the professor who supervised my thesis work or, in his or her absence, by the Chairperson of the department or the dean of the School of Graduate Studies. It is understood any copying or publication or other use of this thesis or part thereof for financial gain shall not be allowed without my written permission. It is also understood that due recognition shall be given to me and to the University of North Dakota in any scholarly use which may be made of any material in my thesis.

Abdulqadir Sheikhmohamed
May 8, 2018

TABLE OF CONTENTS

LIST OF FIGURES

Figure Page

LIST OF TABLES

Table Page

NOMENCLATURE

S	Spanwise Distance (cm)
X	Streamwise Distance (cm)
D	Diameter of the Pin (cm)
H	Flow Channel Height (cm)
Re	Reynold number of flow (dimensionless)
X/D	Streamwise spacing distance (dimensionless)
S/D	Spanwise Spacing distance (dimensionless)
H/D	Channel Height to Pin Diameter Ratio (dimensionless)
h_{ave}	average heat transfer coefficient (W/m^2*k)
q_{net}	Heat Flux (W/m^2)
k	Thermal Conductivity (W/m*k)
N_{Uo}	Re based Nusselt number (dimensionless)
NuD	Pin Diameter Base Nusselt number (dimensionless)
T_b	Bulk Temperature (°C)

T_s	Surface Temperature(°C)
T_∞	Inlet Temperature(°C)
ε	The effective heat transfer (dimensionless)$\varepsilon=\frac{T_b - T_\infty}{T_s - T\infty}$
ξ	Cooling Parameter (dimensionless) $\xi = \frac{\mathrm{NuD}}{\mathrm{NUo}}(1-\varepsilon)$
f	Friction factor or pressure loss coefficient

ACKNOWLEDGEMENTS

First and foremost, I have to acknowledge the endless support my family provided me throughout my time of study. Indeed, my family was and always is the cornerstone of my strength. The moral and material support my mother continues to give me has made this achievement possible. Also, I am indebted with gratitude and a deep appreciation to my strong and caring wife, Fartun Hussien. Surely you are my role model that I continuously admire throughout my life. I have to appreciate my great advisor, Professor Forrest Ames. I could not finish the journey without his endless support and mentoring. I deeply thank you for the professional guidance you gave me throughout this process. I must also recognize my follow graduate students, Loran Soma and Justin Varty, who I shared the same lab with for a long time. The friendship and the help you guys provide me is something that I cannot forget in my entire live. Finally, I would like to thank the UND mechanical engineering faculty members for providing me and many other students with a friendly environment to learn.

ABSTRACT

Gas turbines play a very critical role in the current energy sector in both power generation and in propulsion for almost the entire commercial and military aviation industry. Higher efficiencies can be developed from gas turbines, either land based or aero-propulsion by raising both the pressure and the temperature of combustion gases which discharge into the turbine section, which is also known as the Turbine Entry Temperature (TET). Turbine blade materials simply cannot operate safely at current TET's of 3000 °F without implementing comprehensive cooling schemes developed in the industry over the years. Normally some of the compressed air is extracted from the compressor discharge and forced into internal cooling passages including serpentine passages in blades to cool the hottest engine components to a safer range in metal temperatures. Often, a portion of air is forced out from an array of tiny holes concentrated in the leading edge of blade aimed to provide internal cooling and a thin layer of protection from hot combustion gases while the rest of the coolant is delivered internally for convection to cool component surfaces to a sustainable temperature. However, the leading edge is quite susceptible to deposition of contaminants from the combustion products which can buildup and plug film cooling discharge holes. In addition, the surface of the leading region experiences intense turbulence, and the turbulence disrupts the film cooling layer from forming stably and protecting the blade surfaces.

The current study was aimed to provide the designers ability to control and distribute the coolant more efficiently using variable hole size impingement jets and high solidity arrays configurations. Initially, 21 different incremental impingement variable hole configurations were tested using combinations of hole sizes which included large (D=.417 inch), medium (D=0.315 inch) and small (D=0.295 inch). Using these 21 configurations, around 103 sets of variable Reynolds number data were acquired and analyzed during this phase. Additionally another 9 test extra configurations were added by introducing the smallest hole size named (petite) with a diameter of 0.25 inches to enhance the distribution of flow through the array. Overall 157 individual data points were acquired in this research with Reynolds numbers ranging from 5000 to 75000 for a select set of impingement arrays. Most impingement arrays were tested over only four Reynolds numbers (7500, 15000, 30000 and 60000) to keep the size of the data acquisition and analysis tractable. The average heat transfer coefficient and the static pressure rise of each row in the array was calculated individually.

CHAPTER 1
INTRODUCTION

The gas turbine engine has become a very important prime mover for both electric generation and almost exclusively for modern aviation propulsion systems, since its invention in early part of twentieth century. The simple gas turbine produces power by first compressing air to a very high pressure and moderate temperature using a series of stages of rotating and stator compressor blades. Next, the fuel is mixed with compressed air and ignited within the combustion chamber. The high energy byproduct gases are then discharged into the turbine section to extract maximum possible amount of power to drive the compressor and other utilities. A nozzle is added behind the turbine section for aero-propulsion engines to use the momentum of the exhaust gases to generate thrust to propel the aircraft. Furthermore, power can also be extracted from existing hot gas by means of heat transfer for land-based power generating gas turbines to enhance overall efficiency using a Brayton/Rankine combined cycle. The fundamental principle of the workings of the gas turbine engine is the Brayton thermodynamic cycle. Brayton cycle analyses show that higher combustion temperatures and increased pressure ratios are required to achieve greater power output and higher efficiency (see Figure 1.1 and Figure 1.2).These temperatures pose quite a technical challenge because current combustion gas temperatures, also known as turbine entry temperatures (TET), far exceed the material melting temperature of critical components in

the turbine section. The only line of defense designers can rely on is internal and external cooling methods to protect turbine blades and guide vanes from catastrophic failure.

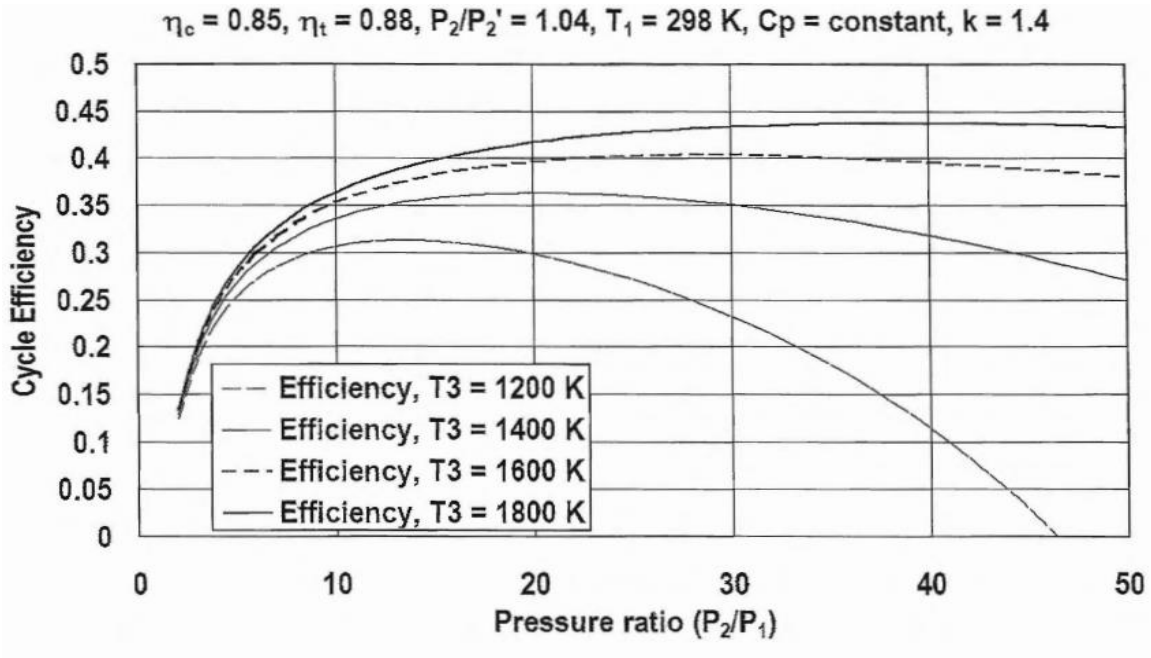

Figure 1.1. Gas Turbine Cycle Efficiency Versus Pressure Ratio and TET.

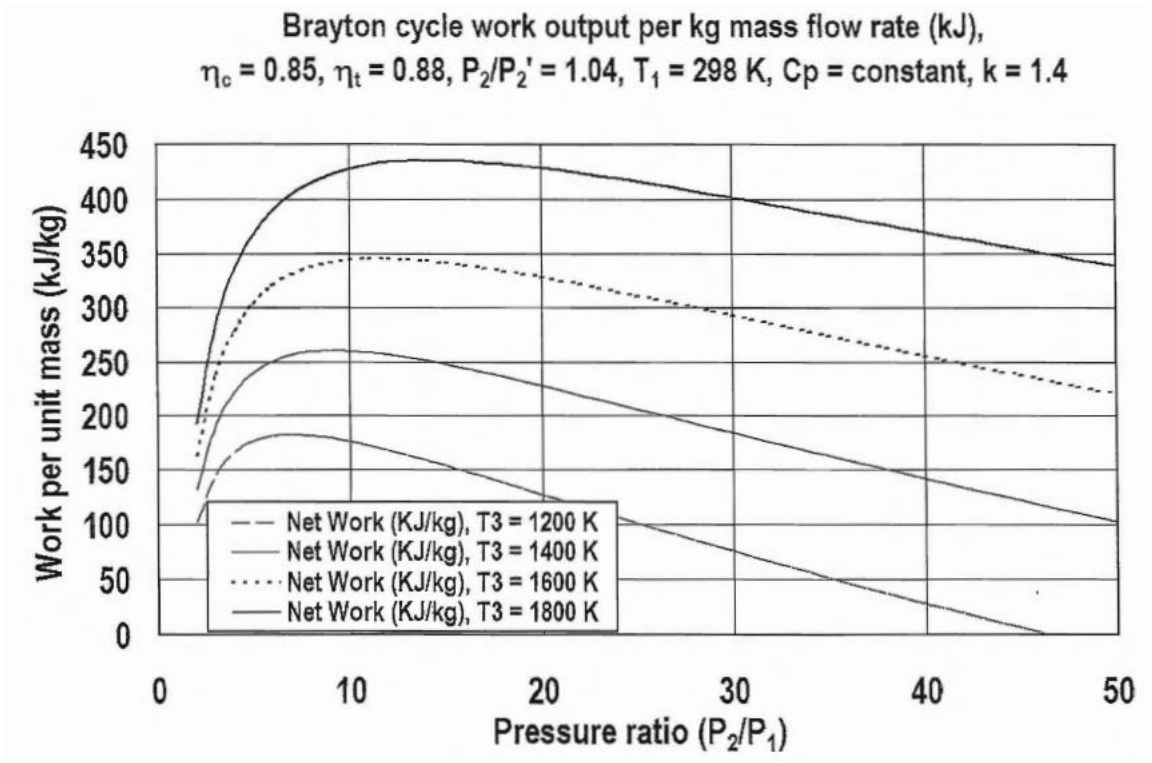

Figure 1.2. Work Per Unit Mass of Gas Turbine versus Pressure Ratio and TET.

Designers usually divert some air from the compressor for cooling turbine gas path components and purging turbine cavities. Turbine cooling air is directed through internal passages in the gas turbine components to cool them to more durable temperature levels. Internal cooling can be delivered in the form of impinging jets onto component surfaces adjacent to the gas path in order to remove the heat load. Another cooling approach, film cooling, works by ejecting some spent coolant air from small holes in an array, typically laser drilled, to provide a shield of protection to the blade surface from the hot combustion gases. Normally film cooling in the form of a showerhead array and impingement cooling is used in the leading edge region of blades and vanes for removing the typically high heat loads in these regions. In the leading edge the structure is quite thick and therefore can accommodate flow passages: however, arrays of cylindrical pins are used in thin trailing

section of blades to provide bridging structural support while also giving a larger surface area for the convection process to take place and cool the blades.

The general approach of this study has been to further improve internal heat transfer levels by combining a high solidity pin-fin array with impingement cooling methods, a cooling method we call incremental impingement. This present study focuses on variable hole size incremental impingement, intended to provide designers with even more control to distribute coolant flow more efficiently. The ability to control the flow condition to match the needed heat transfer through turbine blade can be a very critical tool in order to reduce thermal stresses in the component. These variable hole size impingement jets give designers more ability to control the flow and direct extra cooling air to needed areas of turbine blades. Coolant flow can be allotted to reduce thermally induced stresses on the component and reduce pressure loss while maximizing the overall heat transfer. Gas turbines play a very important role as a source of power in our modern world with several important applications. Two crucial applications include aircraft propulsion and land based power generation. About 33% of the current US electrical power production is generated from gas turbine based cycles. There is well established relationship between gas turbine power output per unit mass and the combustion product temperature also know turbine entry temperature (TET). Turbine entry temperature can exceed 3000 F. In spite of the development of durable thermal barrier-coating protection methods and other high temperature materials, there is currently no material which has properties which can safely withstand such high temperatures today without significant levels of internal cooling. The first stage guide vanes and turbine blades sets next to the combustion system are exposed to the highest thermal loads. Therefore, it is absolutely necessary that a comprehensive

cooling scheme is put in place to protect these critical components. Furthermore, the industry trend to continuously increase the efficiency of turbine gas engines will surely lead even higher TET.

In order to reduce thermally induced stresses on turbine section components, designers extract a portion of the compressed air and deliver it to turbine blades and vanes to remove the heat load internally and reduce the external heat load with film cooling.

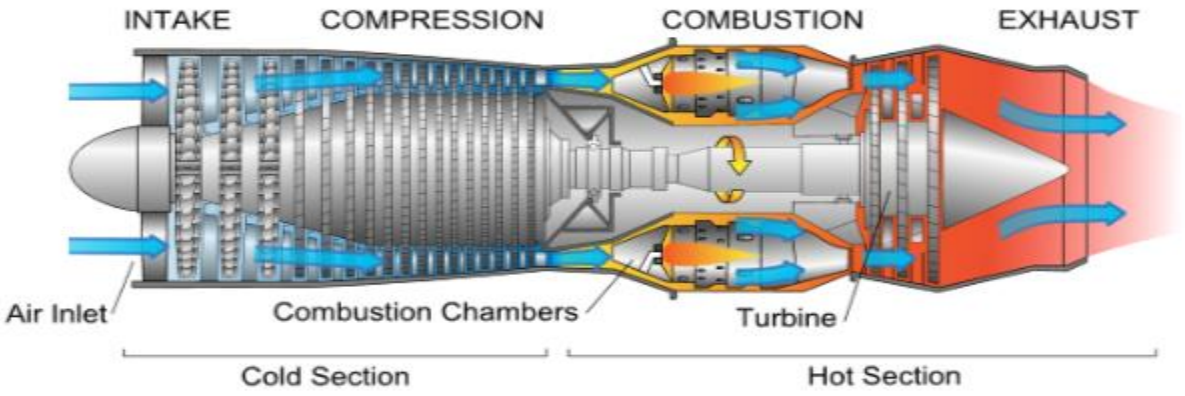

Figure 1.3. Schematic of the Modern Gas Turbine.

Film cooling (external cooling) works by ejecting coolant air through laser drilled hole arrays, angled manner to provide the surface a protective layer from the extremely hot combustion gas products. However, negative issues arising from film cooling include increased aerodynamic losses due coolant flow and contaminant buildup that can block coolant air flow.

The present study investigates the heat transfer and pressure drop related to incremental impingement cooling applications with emphasis on variable hole size to achieve better matched cooling distributions and overall cooling effectiveness. Incremental impingement is applied by incrementally integrating impingement jet holes

behind select pedestals. The coolant jets are directed straight to the hot surface without crossflow effects to provide continuous cooling. Leading edge regions cooled with incremental impingement can easily integrate thermal barrier coatings. Both of these methods are usually applied to manage heat loads in the leading edge region

Increasing the compressor pressure ratio and turbine entry temperature (TET) leads to increased power output and improved efficiencies in both aero-propulsion and land-based gas turbines. Figure 1.1 illustrates the direct relationship between work output and turbine entry temperature (TET) of a simple Brayton cycle.

CHAPTER 2
BACKGROUND

The background chapter in this report presents the valuable and related literatures the researchers previously compiled on several important gas turbine cooling approaches. These methods include conventional and high solidity pin-fin arrays heat transfer. Furthermore, internal impingement cooling and incremental impingement cooling techniques are also reviewed in this report. In addition, there have been several geometric modifications such as pin spacing and line orientation changes (staggered and in-line arrays) to enhance overall heat transfer. Therefore, the heat transfer impact of each configuration change will be also be discussed in this chapter. Quite a considerable amount of researched data of several well developed cooling schemes is available for the designers to integrate and optimize using already existing external and internal cooling technologies. Very recently studies have focused internal impingement arrays with cooling air replenishment added continuously in downstream rows to improve heat transfer augmentation. The added cool air addresses the streamwise decline in pin fin array heat transfer due to the rise in cooling air temperature. Other researches emphasizes fluid flow conditions and row spacing effects on the overall heat transfer and pressure loss in pin fin arrays. Furthermore, there are numerical studies devoted to geometrical effects on surface heat transfer due to pin shape, size and orientations.

2.1. Pin-Fin Arrays Heat Transfer

The pin-fin array provide turbine components with bridging structural support in trailing edge region connecting the pressure and suction surfaces. Pin-fin arrays can also increase the surface area for internal cooling substantially with double walled cooling arrangements in other regions of the component surfaces. Double wall cooling uses the conduction through pins to enable the cool side endwall participate the convection process. Additionally, pin arrays can work as fluid flow modifiers to generate turbulence and flow vortices which disrupt the boundary layers forming on pin and endwall regions, enhancing the array heat transfer in both pin surface area and uncovered endwall areas. There have been quite a number of papers describing research conducted on the pin-fin array heat transfer aimed to find the best pedestal size, shape or array configuration to yield the optimum design in terms of the heat transfer and pressure loss.

The influence of the pin height on overall heat transfer was investigated by Vanfossen [10] using two different short staggered pin-fin models. The larger model had 0.24 inches (0.6mm) diameter pins spaced four diameters and 2 diameter tall in length. the smaller model had 0.125 inch (0.32 mm) diameter spaced at 2 diameters, and the height of smaller model was equal 0.5 diameter. Each configuration was tested using four streamwise rows over Reynolds numbers ranging from 300 to 60,000. The author found the heat transfer level of the short pin array was lower compared their longer counterparts in the literature. The heat transfer level for short pin-fin arrays was estimated to be 2 times higher than the heat transfer for a plain channel [10]. The heat transfer rate from a short evenly spaced (X/D=S/D=2.5) pin-fin array was examined by M.K Chyu et al [18] using a channel height to diameter of unity (H/D=1). The authors used Naphthalene sublimation

technique with the mass transfer to heat transfer analogy to determine the row based average heat transfer. Two different pin-fin streamwise orientations were used, one with staggered and one in-line pins using 7 downstream rows of each. These arrays were tested over Reynolds numbers ranging 5000 to 25000. Also the channel height to diameter ratio of both configurations were selected to be unity (H/D=1) which according to the report [10] is considered to be the optimum channel height to diameter ratio for turbine airfoils. A pin fin arrays with a height to diameter ratio of 1 provides more wetted surface for heat transfer. The pin area and uncovered endwall area are included in the heat transfer calculations. Additionally, pin fins serve as reinforcement to support the structural integrity for trailing edge portion of blade and vanes. due to its heat transfer enhancement and structural support, the pin-fin cooling is most typically used in the thin trailing edge region of blades and vanes.

In addition, M.K.Chyu [6] research also includes the comparison of inline oriented pin-fin and staggered pin-fin arrays in terms of array heat transfer and pressure drop . The study found staggered arranged pins exhibit higher heat transfer compared to inline oriented pins. However, Chyu found staggered pin fin arrays also produce higher pressure drop

Both the surfaces of the pin and endwall are convection areas for heat transfer in pin-arrays. The pin creates a flow blockage and as a result, the convection heat transfer occur in two geometrical distinct part of areas, namely the pin' surface area and the endwall surface area. Each of these areas interacts with bulk fluid flow differently.

Understanding the complex fluid flow physics of convection in pin fin array has motivated several important studies in the field of heat transfer and fluid dynamics. Ames,

Dvorak and Morrow [5] studied the influence of turbulence on pin-fin heat transfer augmentation in staggered pin-fin arrays. These authors used hot wire anemometry to capture the local velocity distributions and turbulence levels, and then correlate the effective velocity and local heat transfer distribution on the pin. Flow stagnates as it approaches the pin leading edge. The resulting static pressure distributions from the pin toward the approaching flow helps create horseshoe vortex systems. Subsequent endwall heat transfer measurement investigated by Ames,Dvorak and Norquist [4] helped to provided a quantitative link between the heat transfer and fluid dynamics in pin-fin arrays. Velocity and pressure distributions were acquired in the array's eight rows. Also The authors used hot wire anemometry to acquire turbulence measurements in the array to help understand the heat transfer augmentation and turbulence levels. This study tried to quantitatively investigate the link between the fluid dynamics and the heat transfer in pin-fin arrays [5]. Furthermore, this study characterized the pin fin array into two, dependent geometric surfaces with respect to the fluid flow. First, the pin's surface area is critical. the pin or pedestal area itself can have many different shapes like cylindrical, rectangular and other geometrical configurations. The other critically important surface area is the endwall which may make up almost 80% of pin-fin array convection area []. The influence of each these surface area in the overall pin-fin heat transfer was studied by several researcher in this field. G.J.Vanfossen [10] studied the short pin-fin heat transfer using two different pin diameter ratios. The study of pin-fin array heat transfer covers not only the surface area of the pins, but also the endwall wetted area is an absolutely critical factor in overall heat transfer [18]. According to reference[18], the uncovered area (endwall area) sometimes make up almost 80% of the array surface area and its impact of the heat transfer can not

be ignored. The full endwall surface area heat transfer of a pin fin array was also studied by Ames et al [4] using an infrared camera with Reynold numbers ranging from 3000 to 30000 in staggered pin fin array. Turbulence generated by the pin wakes contributes to the enhancement of the endwall heat transfer [4]. The same study found a substantial rise in heat transfer across the first few rows. The authors attributed this heat transfer rise to the development of horseshoe vortices around the pins as the flow accelerates and then separates around the pin itself. Ames, Dvorak and Morrow [5] conducted research related pin-fin array heat transfer augmentations and fluid dynamics using hot wire anemometer to capture the local turbulence levels. Additionally, pin midspan's heat transfer distributions were determined using a constant heat flex foil and 24 surface thermocouples and pressure distributions were acquired using 20 pressure taps. Measurements were acquired the heat transfer and pressure distribution from rows 1 to 8. A significant relationship between local pin-fin heat transfer and fluid dynamics was presented in reference [5]. The turbulence levels in the inlet flow were found to be low (1.5%), but the authors found the turbulence levels continuously rise to peak at row 3 (23%) and decline from row 4. This increase of turbulence is mainly due to the unsteady separation around the pins mixing with spanwise velocity component formed at stagnation region [23]. The effective velocity was found to increase as flow separates on the row 1 pins around 80-90$^{\Theta}$ from the stagnation point and fluid rushes to fill the low pressure wake region behind the pin resulting in increased turbulence levels up to 17% [5]. Flow reaches its maximum effective velocity on row 3 due to combination of high approaching velocity from pins on row 2 and flow blockage resulting from row 1 separation. However, according to Ames et al [5], pressure recovery on row 3 is considerably higher (40%) with smaller separation

compared to row 1 and 2. This result in a lower effective velocity and the pressure recovery remains constant from row 4 throughout the array. Therefore, the authors concluded the effective velocity and turbulence are the critical drivers of pin-fin array heat transfer. Also Kays and Crawford's wedge-flow 2D stagnation point heat transfer formula for air ($Nu=0.95ReD^{1/2}$) can be used to correlate the stagnation heat transfer on pins in row 1 and 2 when effective approach flow velocity is used based on the midline distribution. Ames et al [5] found increasing levels of heat transfer from row 1 to row 3,but subsequently the heat transfer declined from row 4. The heat transfer levels in row 3 and beyond were related both the effective approach velocity to the pins and turbulent augmentations. This same study suggested the decreased of effective velocity at row four and beyond contributes to the heat transfer reductions reported in many publications in this field.

Naphthaline sublimation was used to investigate the heat transfer for endwall and pin surfaces by M.K.Chyu el al [7], and the authors indicated 10-20% more heat transfer occurred on surface of pins.

2.2. High-Solidity Pin-Fin Array Heat Transfer

High solidity pin-fin arrays can have quite an advantage in the very thin trailing edge section of turbine blades and vanes due to its heat transfer improvement and extra mechanical reinforcement. The heat transfer distribution of pin-fin array are mainly influenced by mean velocity and cross-flow velocity components created by the flow going around to adjacent pins. Jaswal and Ames [11] studied high solidity pin-fin array with round shaped and diamond shaped pedestals. Both configurations were test in constant height channel and a converging height channel. According to the authors, the high solidity pin surface ratio to the total area in this reference was increases to almost 60% compared

to conventional pin-fin array with about 22% [11]. Also, pin-fins and pedestals used by Jaswal and Ames[11] caused the flow blockage of 60% and 58% while typical pin-fins only block 40% of the cross flow area. Both the heat transfer and array's pressure drops were calculated in row averaged basis in all configurations. The converging arrays were found to result in a lower average heat transfer of around 6% compared to the constant flow channel height one at a given Reynolds number. The authors indicated the heat transfer levels were influenced by flow acceleration in the converging section arrays. Both the streamwise array orientations and geometrical shape of the pin-fins were studied by early researchers in this field. Initially, there was great interest in the investigation of the influence the pin spacing(both in streamwise and spanwise) and row orientation (staggered vs in-line) on heat transfer and pressure drop. Brigham and Van Fossen [6] conducted a experiment using two staggered pin-fin arrays. The authors initially tested an array of 4 diameter long pins with eight rows in the streamwise direction. In the same study, 1/2 diameter long pins with 2 diameter spacing resulted in a considerable heat transfer advantage. Furthermore, researchers obtained a greater increase in heat transfer when they added an extra row of pins in both staggered and inline pin row orientations. This indicated a substantial role that both pin height to diameter ratio and spacing play in pin-fin heat transfer levels. The two different height and spacing configurations were tested and the resulting heat transfer were compared. Higher heat transfer was obtained on longer pins compared to their short counterparts in this experiment. For example, the authors found 50 percent higher heat transfer with eight diameter long pins compare to four diameter long pins. The same study found a greater effect of pin length to diameter ratio on heat transfer which was especially prevalent at low Reynolds number.

Variable spanwise and downstream spacing was used by Jubran et al [8] to seek the optimum heat transfer and pressure drop for pin fin arrays. Reynolds numbers ranging from 5000 to 54000 were used, and the maximum heat transfer was obtained at streamwise spacing of X/D=1.25.

2.3. Row Spacing and Other Geometric Effects on the Pin-Fin Heat Transfer

The pin-fin array heat transfer has a tendency to peak at the first couple of rows in the array, and the heat transfer decline beyond first couple rows was quite common with all the literature reviewed as illustrated in Haley graph (Figure 2.1). The heat transfer peak is mainly due the air picked up more thermal energy as it flows downstream and the cross-flow effect as described in other part of the this report the higher effective velocity found in row three due to the upstream blockage as well as the turbulence generated by the upstream wakes. However, several design factors such as pin spacing [20] and flow Reynolds number seem to influence and may even delay the peak location of the pin-fin array heat transfer. As a result, a substantial number of investigations have been done regarding the study the effects of the pin's spacing, geometrical shape and physical row arrangements for both experimental and computational approaches. For instance, Ames and Dvorak [23] acquired full surface pressure distributions on both the pin and endwall areas in their pin-fin array. The aim of that research was to understand the pressure field. An eight row array with streamwise and spanwise spacing of 2.5 diameter was used in that investigation. Also the height to diameter ratio was equal to 2. The authors reported almost periodic fluid and pressure properties on row 5 and beyond. The row to row development of turbulence levels and velocity intensities were reduced from row 5 and beyond according to the report [23]. It is believed that decreased turbulence levels are the cause the heat

transfer decline in the downstream rows. Simulation of these experimental studies has been undertaken using computational fluid dynamics software for both pin-fin and impinging cooling jet heat transfer aimed at supplementing the experimental approaches over the years. In addition, flow channel modifications have also been included in these investigations to evaluate the influence of these modification on the overall pin-fin heat transfer. In fact, Jaswal and Ames [11] conducted heat transfer and pressure drop analysis on a constant flow channel and converging one using round pin-fins and diamond shaped pedestals in high solidity arrays in both cases. Spanwise spacing was set at 1.674 diameters and streamwise spacing was set at 1.043 diameters while the constant channel height has an H/D=1

G. J. Van Fossen [10] studied the inclination effects on the pin-fin effective heat transfer by compared the normal pin and 30° tilted pin heat transfer. The aim of this investigation was to see if wake shading created by tilted pins can be extended streamwise to the next row, and therefore, heat transfer improvement was expecting with inclined pin due to stretched wakes. However, the author found no different between normal pin (straight) and inclined pin in average heat transfer terms [10]. although, Van Fossen's report suggested the inclined pins can enhance the effective heat transfer in an array by increasing the wetted surface area due to tilt angle. In addition, the effect of the pin's endwall fillet to array heat transfer and fluid flow was studied by M.K. Chyu [7] using the naphthalene sublimation technique mass transfer analogy. The heat transfer and pressure drop of straight cylindrical pin fin arrays and filleted cylindrical pin fin arrays were evaluated using both inline and staggered arrangements. Also the pin spacing and height to diameter ratio fillet pins and straight pins were the same between the two models. The author reported

straight pins perform at similar trends with their counterparts in earlier studies in terms of both heat transfer and pressure loss, but the lower average heat transfer and higher pressure loss was found on the pins with endwall fillet configurations. The pressure loss in the enwall fillet was even higher in the staggered configuration. The author also concluded the staggered pin-fin arrays had higher heat transfer coefficient compared with inline pin-fin arrays. However, the pressure loss associated with staggered pins was also greater.

The average heat transfer and flow friction factor of staggered pin-fin array study was also reported by Armstrong and Winstanley [24]. The influence of the pin heights, row spacing and channel flow convergence to the average heat transfer and the flow friction was reviewed based on investigation in the literature. The findings of all parameters were presented in correlations with early research of similar experiments done by Metzger. The row averaged heat transfer (Nu_D) correlation presented in [24] agreed within 20 percent range with data reported by Metzger's early work except in the case of extremely close streamwise spaced (X/D=1.05). In this particular case the correlation result was off beyond the 20 percentage range. The author concluded the average heat transfer is function of Reynolds Number to the power of 0.6 to 0.7 depending on the channel height to diameter ratio (H/D). No significant effect of pin height on heat transfer was found with height to diameter ratios (H/D) of less than 3 according this report. However, for H/D greater than 3, the heat transfer appears to increase with an increase of height to diameter ratio according this report. In addition, the authors also found the converging pin-fin channel can reduce the both the heat transfer and the friction factor by around 20 percent. A similar trend of heat transfer reduction in converging section pin-fin arrays was also reported by Jaswal

and Ames [11]. However, the difference between the two reports is no pressure drop correlation was presented in [11].

2.4. Internal Impingement Heat Transfer and Associated Pressure Drop

The internal impinging jet can create a higher magnitude of heat transfer than any other convection heat transfer application available today [13]. Furthermore, the impingement cooling method gives the designer more ability to control the heat transfer by adjusting the coolant flow condition and the surface geometry as needed. Jet impingements with turbulence enhancing surface enlargement configurations were investigated by Mats O Annerfeldt et al [21]. Four different geometries were tested including triangles, wings, and cylindrical and dashed ribs. All the structures were made from aluminum, and all the impingement jets were oriented in staggered arrangement with Reynold numbers ranging from 20,000 to 65,000. The temperature distribution within the array was captured using an infrared camera in reference [21]. The same study found a decreasing heat transfer trend with an increase Z/D (channel height to jet diameter ratio) for all tested geometries. While all the configurations show a modest improvement in heat transfer (1-1.3) levels compared to a flat plate, cylindrical and ribs obstacle are more favorable due their low pressure loss according to authors.

The internal impingement heat transfer with the presence of initial cross-flow was investigated by L.W. Florschuetz et al [15] using both inline and staggered hole configurations. Three initial cross-flow to jet flow rate ratios (m_c/m_j) of .2, .5 and 1.0 were tested in all geometries both inline and staggered hole orientations. The coss-flow present in the jet array resulted in a substantial reduction in heat transfer even with the smallest initial cross-flow in system. The heat transfer created by jet impingement directed toward

the perpendicular hot surface has been subjected to quite an extensive number of studies in gas turbine cooling research over the last few decades. For instance, the average heat transfer coefficient of square configured arrays with round impinging air jet striking the heated surface was investigated by D.M.Kercher and W.Tabakoff [12]. A single line of impinging jets with and without crossflow present was tested, and the critical effect by the crossflow on overall internal impingement heat transfer was investigated. In addition, other important parameters such as jet diameter, jet spacing and channel height were all evaluated in this study. Authors reported significant increase of heat transfer resulted when smaller diameter holes is used with combination of increase of the number holes. Also,the overall degradation due to the cross-flow in impinging jets was documented all papers reviewed in this report.

The jet induced heat transfer and pressure loss within the array with turbulence enhancing obstacles (ribs) was studied by Hussian and Andrews[16] using three different rib configurations. Three different shapes and sizes of flow obstacles, A (full width ribs), B(slotted ribs) and (CB) slotted ribs with decreased blockage, were constructed and tested. The magnitude of the heat transfer and pressure drop acquired in each configuration was compared with similar flow using an unobstructed flat wall. The pressure loss resulted from full width ribs (A) and slotted ribs (B) were quite small in magnitude. around 10% for A and 13% for B compared to the unobstructed flat wall. These pressure loss value were correlated with heat transfer increaseed of 18.8% and 19.9% for A and B using a 0.72 exponent in relation with mass flux and heat transfer provided in the same investigation. On the other hand, the CB slotted rib with increasing blockage resulted in the highest pressure loss compared with design. About a 41% increase in pressure loss and a 28%

increase in heat transfer was obtained. It is important to note that the authors attributed all this increased pressure loss mainly to the cross flow with a minimum effect of the jet walls. In addition, streamwise flow convergence was used in reference [19] to study the overall pin-fin array heat transfer in non-uniform height to diameter (H/D) ratio array. Downstream heat transfer improvement had been reported in that study [19] due flow acceleration through the converging area.

The heat transfer coefficient and pressure loss increase resulted from impinging jet supplemented with effusion flow was studied in an investigation [17] by G.E.Andrews et al. According to authors, combination of these existing cooling methods were aimed at improving the effectiveness of the impingement flow.

The influence of cross-flow on internal impingement cooling array was studied by D.E.Metzger and R.J.Korstad [13] using single spanwise line. Significate heat transfer reduction has been observed on the upstream region in this impingement jet area while downstream heat transfer increases as crosflow deflected the jet at a downstream angle. In addition, authors found a relationship between hole spacing(C_n/D) and crossflow degrading the jet impingement heat transfer. The crossflow effect on the heat transfer on the impinging jet completely disappeared when C_n/D increased. The critical contributors on jet impingement were noted in reference [13]. The main and the most important driver of the internal impingement heat transfer is the impinging jet. However, Authors found that heat transfer impact is considerable reduced when the crossflow stream deflects impingement jet angle lass then 90 degrees. It creates the highest heat transfer in circular area with size a 5 times the jet diameter [13]. Another important heat transfer factor in internal impingement is presence of turbulence in fluid flow field.

2.5. Incremental Impingement Heat Transfer and Pressure Distributions

Normally, the greater levels of heat transfer can be achieved from impingement jets, but its heat transfer capability declines in the downstream direction after first few rows due to crossflow effects. The incremental Internal impingement addresses the crossflow effects by hiding the jet behind the cutout region of pedestals. This provides the jet necessary protection from the crossflow so the jet can directly reached and sufficiently cool the hot endwall surface. Furthermore, incremental impingement combined with high solidity pin-fin arrays protects the jets air from degraded effect due to the cross-flow and enhances heat transfer by hiding the jet in a cutout region behind the pin's wake region. Injecting the jet in this ,high solidity,pin's shadow area allows the jet to strike the endwall surface with full stagnation velocity and achieve considerable convection heat transfer while protecting, the jet cooling from mixing with the heated crossflow. The area of maximum impingement jet heat transfer was estimated to be 5D where D is the jet diameter by [13]: however, this assumption was based on a single impinging jet without presence of any cross-flow where fluid spreads and accelerates in all direction. The cross-flow develops a protective boundary layer over the hot surface that deflects the jets from hitting the hot surface it was supposed to cool [2]. To address this degraded cross-flow effect, an investigation was undertaken by Butch et al [2] in a experimental investigation using a combination of high solidity pin-fins and impingement jets. This newly developed novel idea to address the cross-flow effect on jet impingement heat transfer using an approach very similar with present study called incremental impingement. In this approach, jets are injected through the cutout side of a pin to hide it from the cross-flow deflection. It also provides continuous coolant replenishment throughout the array which addresses the

coolant heat up issue typically experienced in pin fin arrays. In reference [22], the authors used large eddy simulation (LES) to model the complete flow fluid and heat transfer. The velocity distributions of several hole configurations were precisely correlated with the present experimental studies for the same configurations. Furthermore, researchers presented the relationship between the higher heat transfer augmentations obtained in the present work using certain hole size combinations (PLPPP) and mass flow rates in their model. The variable hole size method gives the designer more control to mitigate jet impingement's inability to maintain sufficient heat transfer capacity after first couple rows has negatively impact its cooling potentials. . Lately, researchers, including Busche and others as well as this present study are developing quite a novel approach to address cross-flow blockage that prevents coolant jet striking and cooling intended target. There have been numerous studies conducted on pin fin heat transfer and internal impingement aimed to find best configuration and geometrical design to produce optimum heat transfer with reasonable pressure drop.

CHAPTER 3
EXPERIMENTAL APPROACH

This chapter describes the overall bench scale experiment performed to acquire internal heat transfer and flow information on the variable hole-size incremental impingement geometry. This chapter will descript the bench scale internal heat transfer and flow rig. The heat transfer test surface geometry and instrumentation will be document thoroughly. The PC based data acquisition system and its various components will also be described. Some of the initial data acquired to document the initial hole discharge coefficients will be examined. Finally the experimental uncertainties will be described and quantified.

3.1. Bench Scale Internal Heat Transfer and Flow Rig

The internal heat transfer and pressure drop measurements were acquired for the variable hole size incremental impingement in UND's bench scale internal heat transfer and flow rig shown schematically in Figure 3.1. This bench scale rig is powered using a high pressure New York Blower capable of providing 400 CFM (m3/s) at a static pressure rise of 21 inches water gage (5250 Pa). The blower discharges into a plenum box used to cool and direct the air into the orifice tube. The large orifice tube is used to measure the inlet flow rate into the test section. The airflow discharges from the orifice tube into a diffuser which connects to a screen box flow conditioning section. Furthermore, the plenum connects directly to the flow conditioning section and directs air into the heat transfer test surface. The heat transfer test surface is used to experimentally determine the

heat transfer rate and pressure drop within the cooling array and then discharges the air to atmosphere through 60 degree downward a slot.

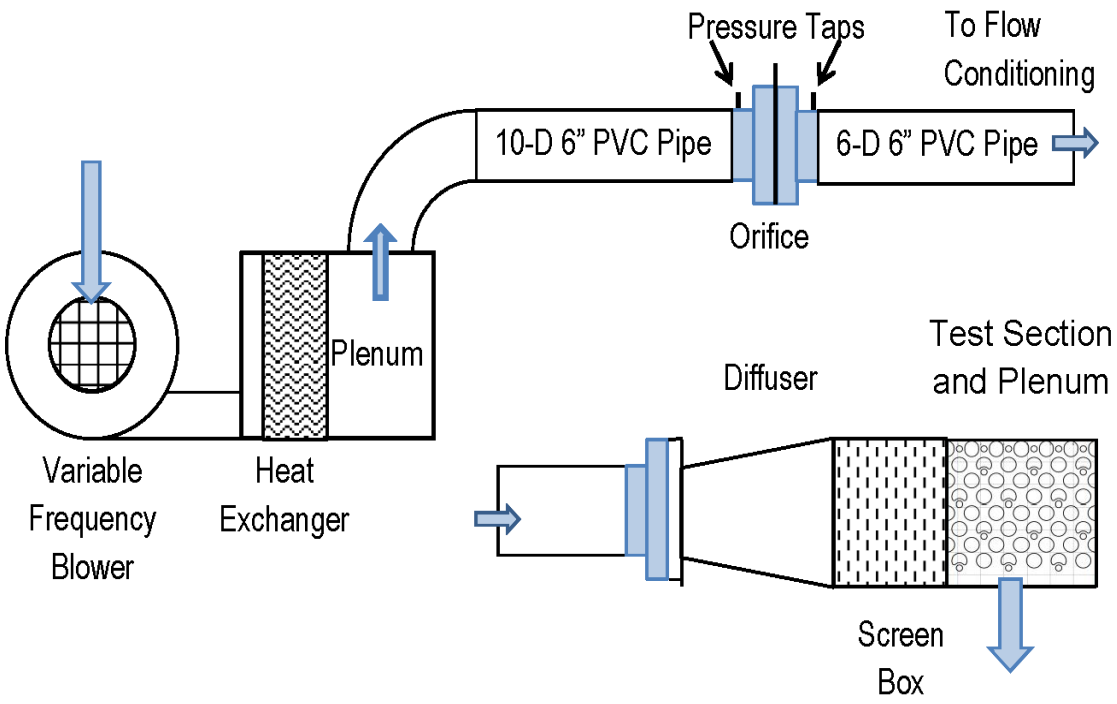

Figure 3.1. UND's Bench Work Internal Cooling Heat Transfer and Flow Rig.

3.2. Description of Blower, Orifice, and Flow-Conditioning Section

The bench scale heat transfer and flow rig is driven by a New York Blower, pressure blower. The pressure blower has an 18 inch diameter wheel and a 3 inch outlet and is driven by a 3 HP electric AC motor which is controlled remotely using a variable frequency drive. The New York Blower is used to draw the ambient air and supply airflow can be adjusted with a great accuracy with a mass flow rate producing Reynolds numbers ranging from 5000 to in excess of 75000. This particular blower has a flow rate capacity of 250 CFM (0.12 m^3/s) and can increase the static pressure to around 22 inches water

gauge (5500 Pa). The blower discharges the airflow into the heat exchanger plenum next to blower which cools the air to maintain near room temperature flow throughout testing. This system uses a water reservoir tank with a pump to draw and circulate cooling water through the heat exchanger so the airflow from the blower remains near ambient temperature even at higher pressure ratio conditions. The tank water level is maintained by drawing water from the water supply while the used coolant water overflows directly to the drain. The airflow is then directed upward into a 15 cm diameter PVC 90° elbow. The elbow is connected with a 15 cm diameter PVC orifice tube that includes one of two large sharp edge orifice plates to measure the flow rate continuously throughout testing using the pressure differential across the orifice plate. The flow goes through another 0.95 m downstream section with same diameter that discharges into 12cm by 12cm rectangular shaped diffuser that slows down the flow. There is one K type thermocouple installed within the diffuser intended to acquire the temperature of the airflow before it reaches the test section. The air flows through the flow conditioning section, which is made up of four nylon screens spaced 5 cm apart to restrict the air in order to provide a uniform flow distribution approaching the test section plenum box.

When the flow reaches the plenum box, the air slows down completely and uniformly, and it is forced into 5 rows of holes, each row containing six holes. The holes direct the air downward through the top of the cool side plate to strike perpendicular onto the hot side or heated surface of the test section. Then the flow enters the very complex flow field in the pin-fin arrays. The jet flow impinges and spreads on the hot side endwall, stagnating on the leading edge of the downstream pin and then accelerating around the pins mixing with the cross flow present. This complex fluid dynamics in the pin-fin array is

assumed to be very critical for enhancing the heat transfer, and it was intentionally added to the design to achieve the maximum convective heat transfer from the airflow. Finally, the air is discharged from a slot with a 30° downward angle from the test section into the atmosphere.

3.3. Test Plenum Layouts

The plenum box was designed in-house and contains both the test plate and the inlet instrumentation that references the test plate pressures and temperatures to the inlet plenum conditions. However, the inlet temperature were found to be effected by radiation error so a thermocouple in the upstream of the flow conditioning section was used as a reference. The plenum box was meant to accept the inlet airflow and provide uniform distribution as it passes into the test plate. In addition, the plenum box and surroundings were designed to provide all its containments including insulation of the test section with minimum or no heat transfer into surroundings and ambient air around it. This particular plenum was made as a rectangular shaped box with all its walls completely closed and sealed to avoid any air leakage. Both the front inlet face of the test box and flow conditioning section of the diffuser have flanges with a same dimensions that can be clamped together tightly to prevent airflow leakage. Furthermore, a closed cell foam seal was placed between flanges to ensure firm contact and air tightness. Each side of box surrounded the test section was constructed using a 0.125 inch thick acrylic interior layer and 1 inch thick outer layer of isocyanurate foam with a 6.5 R-value thermal resistance .Between the two layers, a high strength multipurpose foam adhesive was used to laminate the two layers. Furthermore, aluminum foil covered all exterior faces of the foam layer to reduce thermal radiation and further reduce porosity.

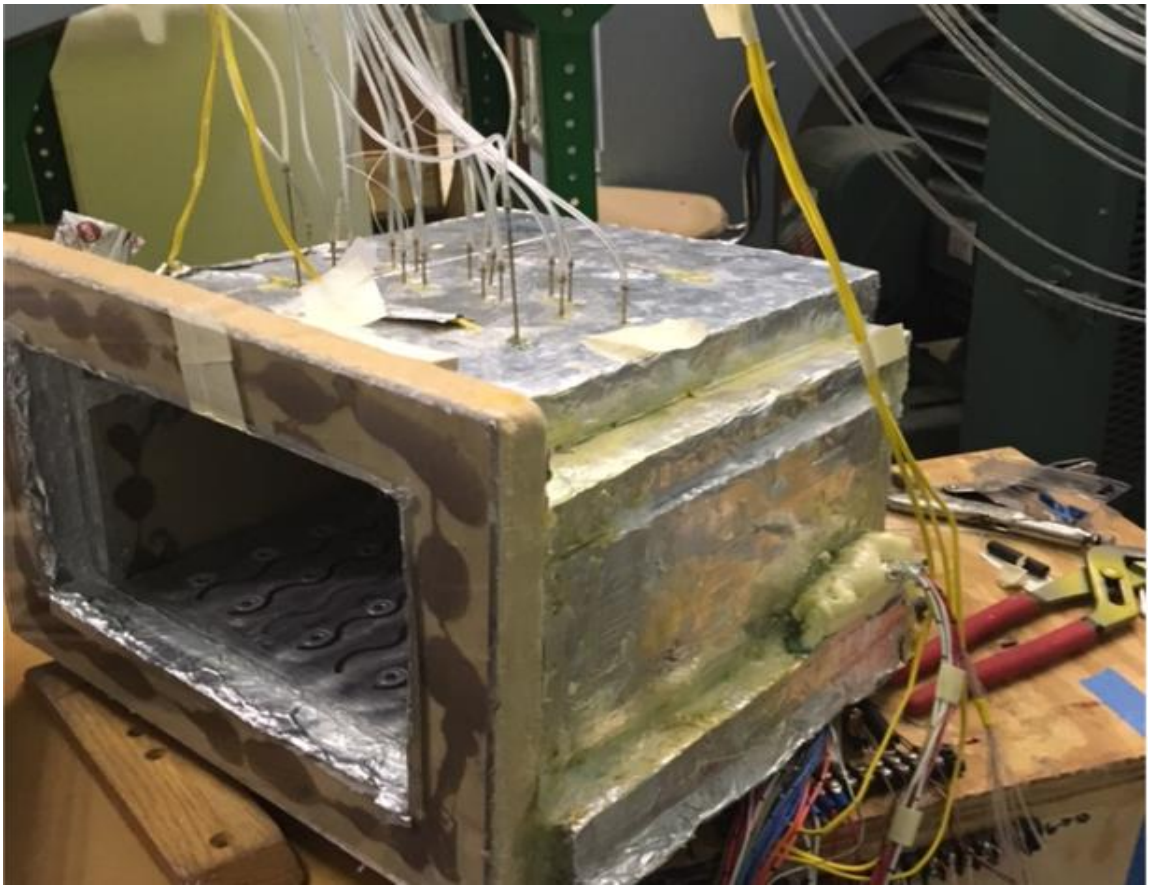

Figure 3.2. Plenum Box and Heat Transfer Section with Instrumentation Access.

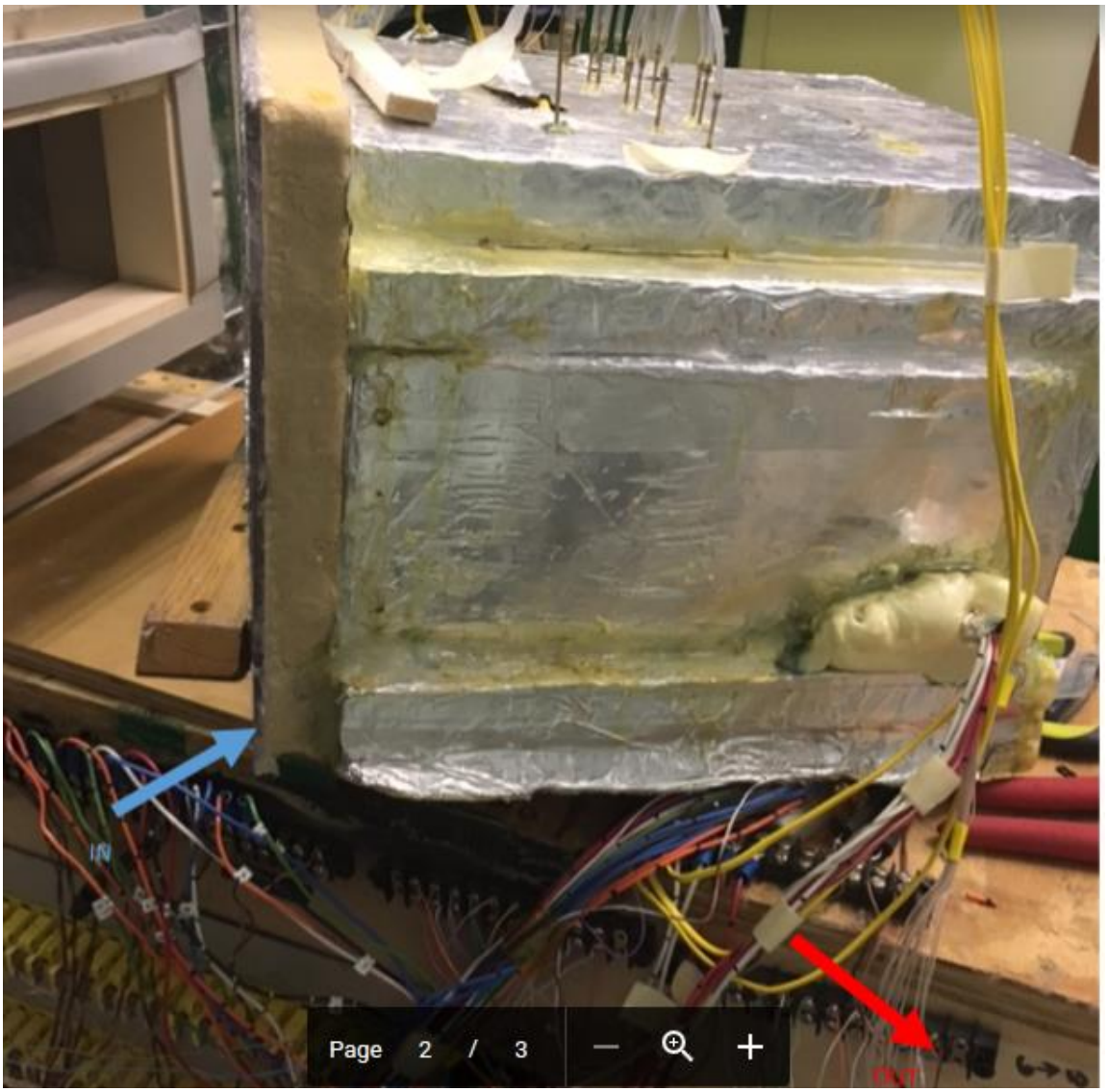

Figure 3.3. Plenum Box Showing Pressure Tubes, Thermocouples, and Heating Wiring.

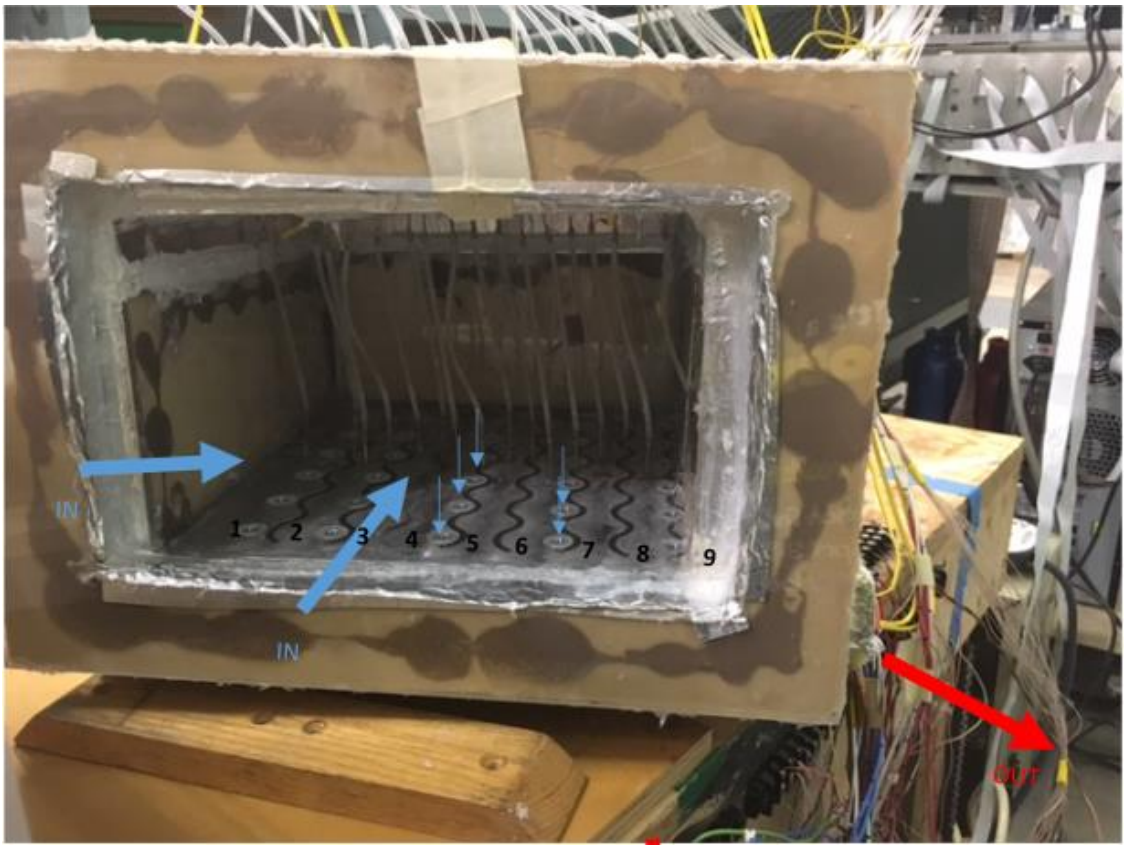

Figure 3.4. Plenum Box with Flow Illustrations and Static Pressure Instrumentations.

3.4. Instrumentation Informational Section

The instrumentation for this incremental impingement test was assembled with the intention of providing continuous and accurate information on the local temperatures, pressures, and heater power. The conditions sensed by this instrumentation were related to the heat transfer and fluid dynamics of interest throughout testing phase of the experiment. This instrumentation consisted of more than 50 K-type thermocouples and 16 static pressure taps installed directly within heat transfer test section. Another two K-type thermocouples and two extra static pressure taps were placed within the plenum box to sense the air total temperature and pressure in the plenum to provide a reference for the

conditions acquired in the test plate. The wall temperatures in the plenum were captured by three more K-type thermocouples which were attached to the inner surfaces of the top, back and side walls of plenum. These temperatures helped to account for any possible heat conduction through the plenum walls caused by radiation from the plate. There were another three thermocouples placed in the exit region of the slot to measure the exhaust air temperature to enable an approximate energy balance for the air. All the thermocouples were connected through the multichannel passive reference junction that connected to the HP3497A data acquisition module. The pressure taps were connected into a pressure scanner attached to two Rosemont smart pressure transmitters with full scale ranges of 1 and 25 inches water pressure gage (250 and 6250 Pa). The pressure transmitters generate a 4 to 20 milliamp current routed a cross a precision 500 ohmresistor to provide a 2 to 10 VDC signal to the data acquisition unit. All the temperatures, heater voltages and currents, and air mass flow rate measurements were continually sensed by the data acquisition unit and written to the screen by the data acquisition program. The data acquisition program allowed the ability to monitor each reading continuously while updating appropriate power supply outputs.

The power to the heaters is supplied to individual rows and individual sections. The heaters are controlled by supplying a variable voltage to individual power supplies using adjustable potentiometers connected to each power supply. This configuration allows operators to vary the power to heat different sections of the heat transfer test section to achieve a uniform steady state temperature throughout heat transfer surface before recording the test data. Power is dissipated in two 12.7 cm long by 1.27 cm wide serpentine heater strips for each row which are adhered to the “hot side” endwall surfaces in rows

with pedestals. The great care was taken by cleaning the wall surfaces to make sure the heater strips were in good contact with surface for good thermal conduction. Two voltage leads were also connected at the end of each heater to closely monitor voltage difference across each heat transfer section. The current through the heaters was determined using a calibrated shunt resistor. All heater voltage and current readings were monitored during the experimental testing and updated periodically on the monitor along with thermocouple readings for each heat transfer section.

The pressure blower variable frequency drive was controlled using a variable voltage adjusted with a KΩ potentiometer to change the mass flow rate to set an exact Reynolds number for each test condition as needed. This potentiometer and the array of 11 variable resistors used to control the power supplies were placed adjacent to the PC monitor. The potentiometers allow adjustment of the heater power settings to nearly exact values while monitoring the readings from the program screen.

3.5. Description of the Heat Transfer Section

The heat transfer section used in this experiment consisted two rectangular plates, a “hot-side” plate with six pins in each row and a “cool side” plate heated with the hot side plate through the top of each pin. The test plate consisted of eight pinned rows in the streamwise direction and a downstream plenum region. The plenum region collected the flow and directed it into a 30° exit slot allowing the discharge of spent airflow downward through the “hot side” plate. Both bottom plate and top plate measured 11 inches (27.94 cm) in streamwise direction and 10.7 inches (27.178 cm) in the spanwise direction, (see Figure 3.1, bottom plate and Figure 3.2, top plate). Both top and bottom plate had the same thickness of 0.25 inches (0.635 cm). The round pins protrude upward 0.5 inch (1.27 cm)

in height from the bottom plate and the pins were 1 inch (2.54 cm) in diameter. All the components (plates and pins) described above were fabricated from homogenous cast Aluminum tooll plate which was precession machined in to the desired geometry. There were serpentine grooves cutout between rows to isolate the rows from thermal conduction from one row to another. These serpentine grooves were completely filled with a low thermal conductivity epoxy. The epoxy fill was also smoothed to a uniform level with endwall surface after casting to remove any roughness present that might restrict the flow.

In addition to rows of round pins, a round shaped cutout was made on the back-face of those pins located directly below the edge of impingement jet discharge holes in the top plate. The pins with cutouts were intended to shield the discharging jet from crossflow to enable the jet to strike on the hot surface directly. As a result, these pins with round cutouts were placed below the edge of the every hole in top plate except for the first row holes. The first row of holes had no cross-flow and upstream protection was absolutely unwarranted. The pins were oriented in staggered arrangement. Generally, impingement jets with cutout pins were located every other row. The staggered arrangement is believed to enhance the fluid mixing and other fluid flow phenomena which early researchers attributed heat transfer improvement.

The high solidity of the array and the height to diameter ratio of 0.5 were also used to improve heat conduction between the cold plate (top plate) and the hot plate (bottom plate). The temperature variations between the two plates was ranging from 0.31 °C in the low Reynolds number flow to 1.3 °C at Reynolds numbers flow. It is important to note thermally induced stresses can negatively impact the structural integrity of the turbine components. Therefore, the high solidity array used in this testing is expected to

address the temperature variation within the component by increasing the conduction through pins without decreasing overall wetted surface for the convection heat transfer. The jet impingement spacing was another critical factor identified by early the researchers. The closely spaced impinging jets produce the highest heat transfer compared to sparsely spaced impingements jets. With these two issues in mind, the high solidity pins were spaced 1.625 diameters in spanwise direction and 1.074 diameters in streamwise direction to produce 45% solidity in pin array for solid pin row. The impingements jets were placed behind the pins in every other row.

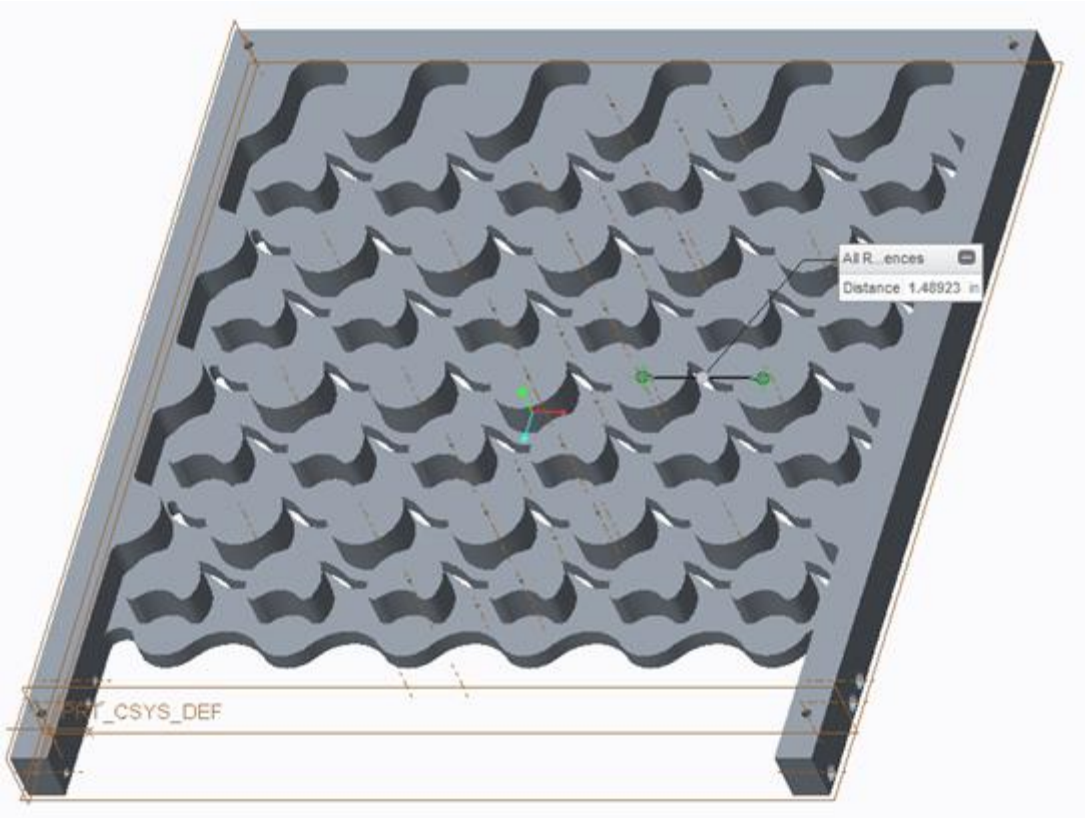

Figure 3.5. 3D Model Sketch of the Bottom Plate.

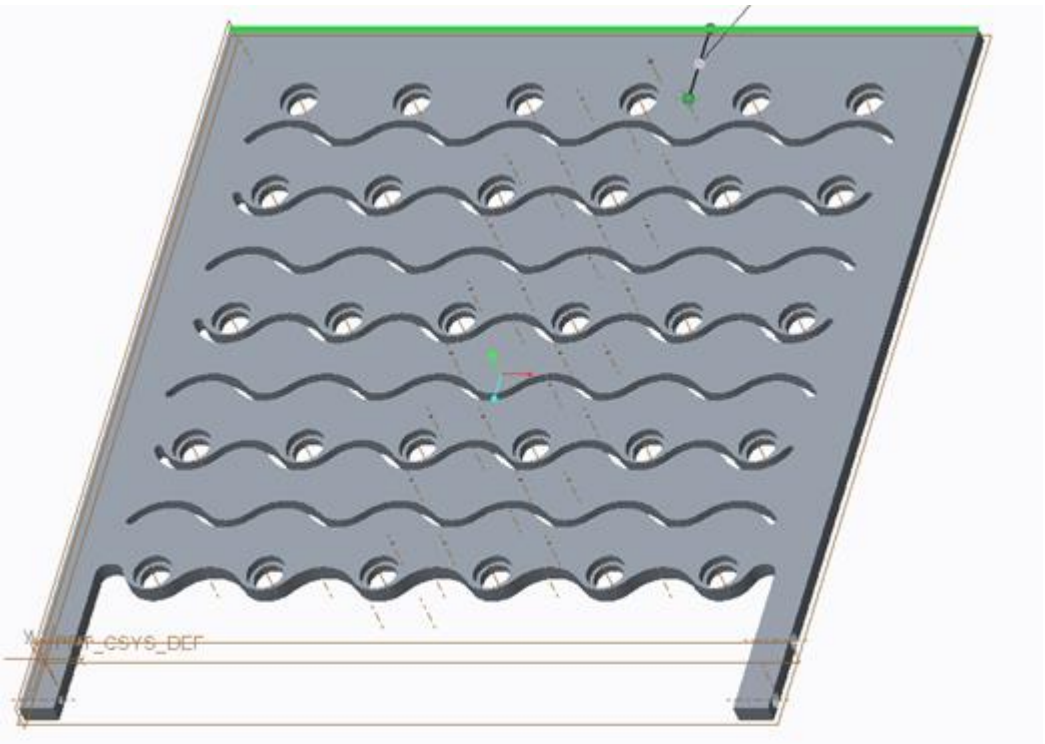

Figure 3.6. 3D Model Sketch of the Top Plate (Cool Side Plate).

3.6. Heat Transfer Analysis

The heat transfer part in this experiment uses 11 DC power supplies, 22 heating strips in pairs of 2 and double walled heat transfer surfaces described in the earlier section. The DC power supplies were controlled using an eleven variable resistor potentiometers. These variable resisters enabled the operators to control and adjust y the power supply of each heated section individually over the heat transfer surfaces. The electrical power is delivered into two Kapton insulted Minco thermofoil heaters configured in parallel style in each section. The surface of the plate was carefully cleaned before the heaters were attached to ensure uniform and firm contact for good conduction (see Figure 3.3&3.4). The two heater foils dissipate the thermal energy of a magnitude described in equation 3.1 in each row where V stands the voltage drop across the heater and I is electric current in

amperes. The serpentine grooves filled with low thermal conductive epoxy were used to thermally insulate each row from heat transfer to or from adjacent rows by means of conduction. The heat is then conducted through 0.5 long high solidity pins to reach the cool side endwall. Equation 3.2 illustrates basic conduction formula of heat transfer. There were approximately 0.09 cc of high thermal conductive epoxy cast between the pins and top plate to laminate the two plates while also providing good thermal contact between them. This high thermally conductive epoxy conducts the heat very well, and the temperature difference between the two plates remains small as reported previous section in this report.

$$Q = VI \qquad \text{Equation 3.1}$$

$$Q = K\left(\frac{\Delta T}{L}\right) \qquad \text{Equation 3.2}$$

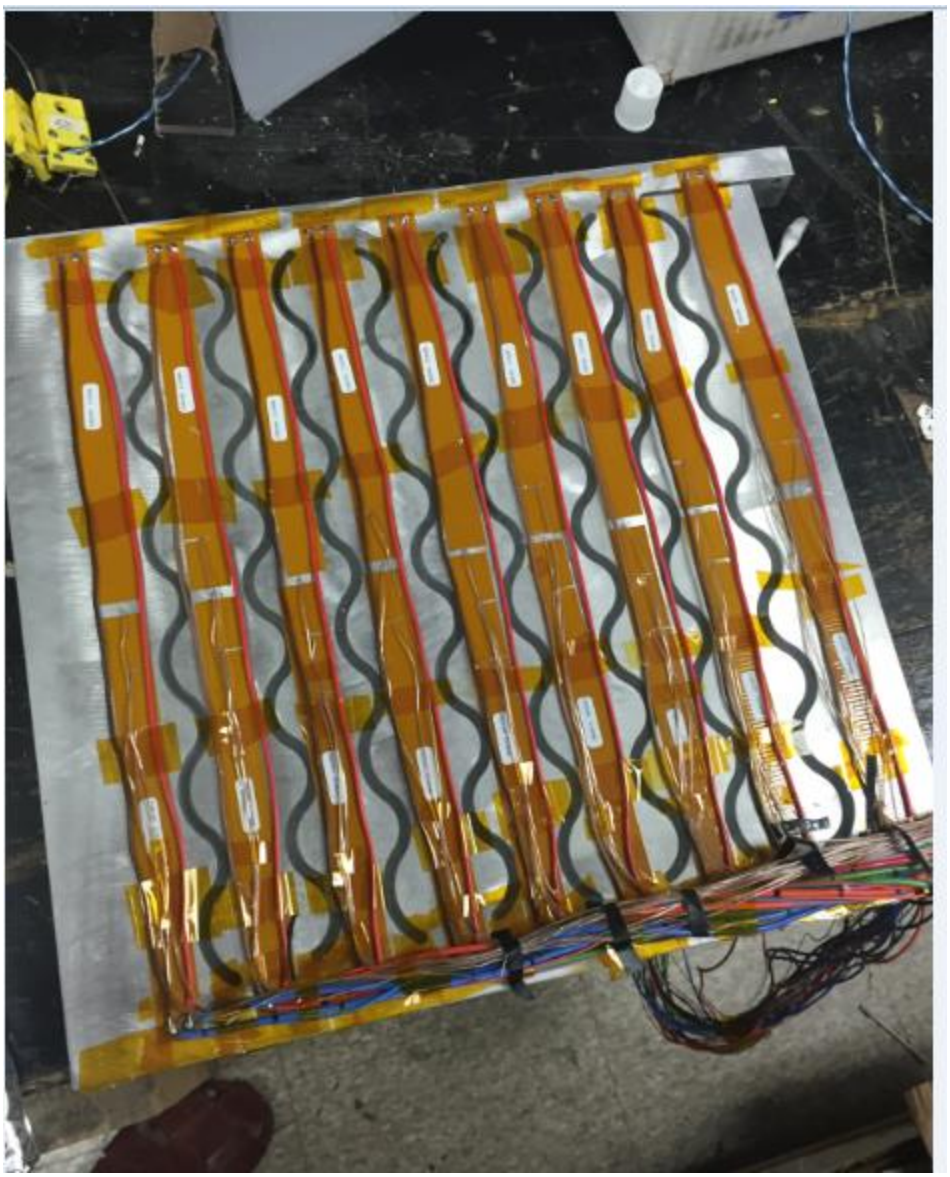

Figure 3.7. Bottom Plate with Heating Strips and Power Wires.

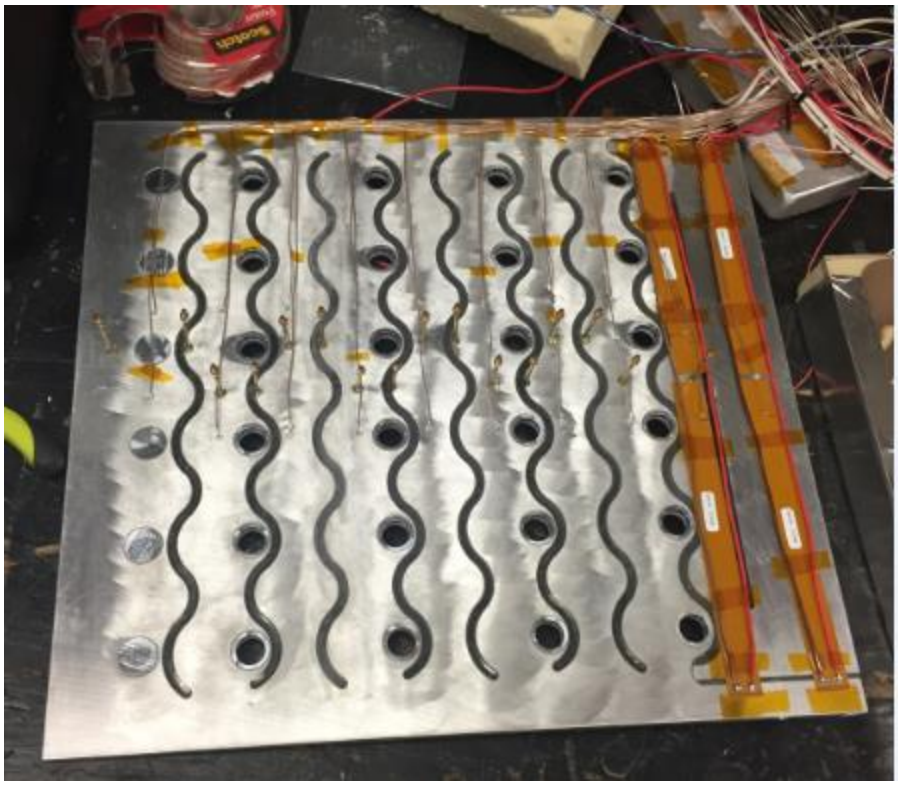

Figure 3.8. The Top or Cold Side Plate with Two Heat Strips over the Plenum.

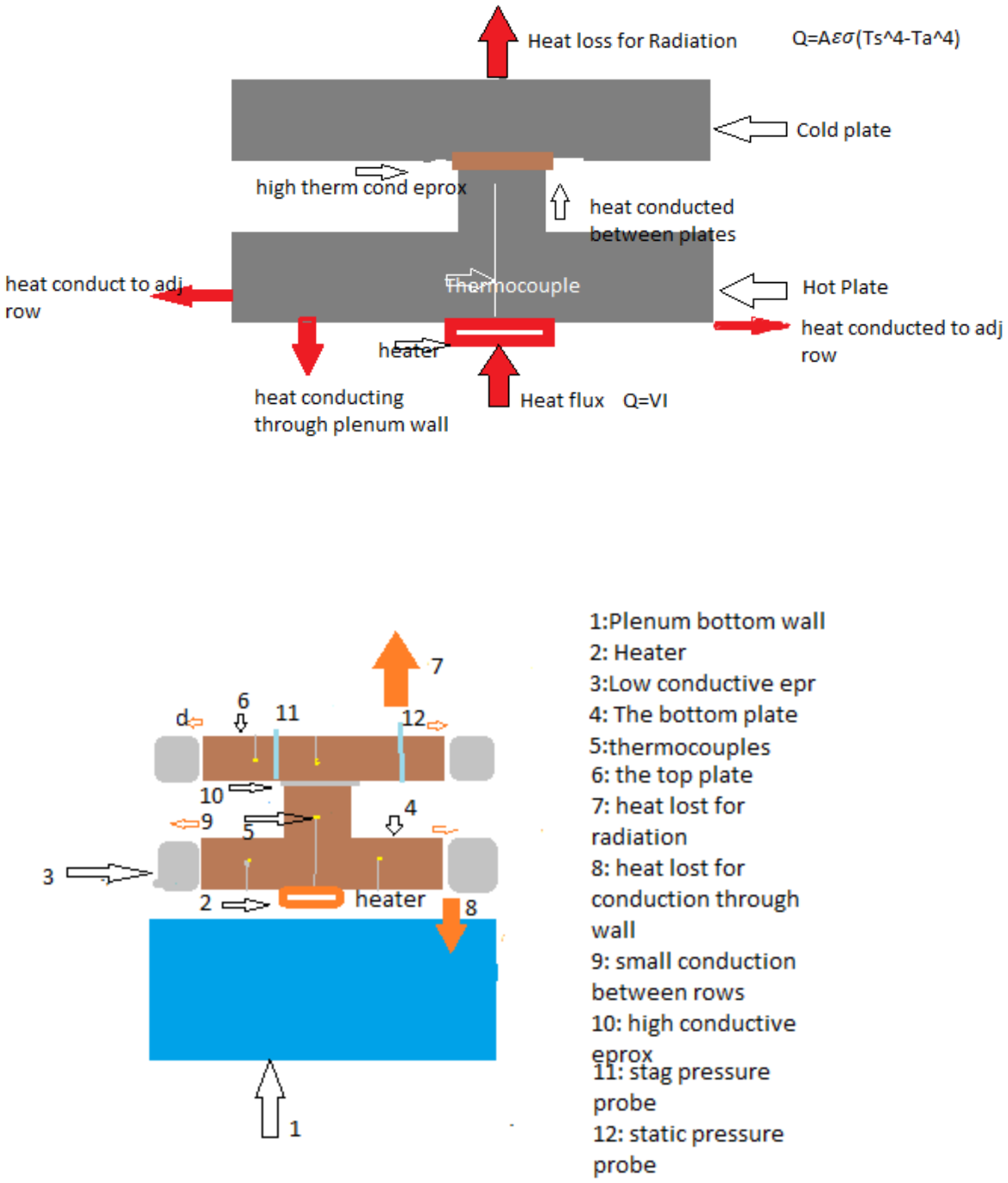

Figure 3.9. The Heat Transfer Calculation Model.

3.7. Data Acquisition System

The PC based data acquisition system is controlled with a Dell Computer which is connected to an HP 3497A data acquisition unit. The HP 3497A was used to acquire all the current experimental data. This data acquisition system has amore 50 input channels which can be scanned at rate of 10 channels per second. In addition, a simple QuickBasic program was used to acquire and monitor the data throughout testing. The QuickBasic program includes both the monitoring and data acquisition subroutines enabling setting data points and troubleshooting data acquisition problems. The program was built to input the current absolute atmospheric pressure prior the testing, so the operator must always read the atmospheric pressure reading from the mercury barometer located in the room 114 of Upson. This input allows the program to updates the absolute pressure to factor in the atmospheric pressure change day to day during the testing. The temperature measurement in data acquisition system was also referenced to an ice bath thermos. Maintaining a good quality water and ice for ice bath reference temperature was critical for the system to accurately capture absolute temperature variations during the testing . As result, the ice bath was replenished almost daily before the testing.

Figure 3.10. Data Acquisition System.

3.8. Uncertainty Analysis

There are always inherited uncertainties in both the experiment procedures and the instruments used to acquire the results, and this experiment was not exceptional. The heat transfer is by nature difficult to control because the heat can be transferred from one body to another easily in several different modes such as radiation, conduction and convection. Hence, there were some expected uncertainty associated with experiment as well included in the heat transfer calculations. However, the early calibration tests of the instruments like resistors and later verification of calculations done on the heat transfer values in this experiment indicated the uncertainties associated this experiment to be very small. The heating power was supplied into the test sections in the form of current multiplied the voltage as illustrated in equation 3.1. The shunt resistor used here was calibrated more than

once, and the uncertainty associated with resistance value was found to be +/- 2% or less. The current measurement uncertainty is expected to follow closely with the uncertainty in shunt resistance. The thermal energy lost to the surroundings was found to be small but still a factor. There was thermal energy lost by conduction through bottom section of plenum and the walls. The key driver of that heat transfer was the difference temperature between the test section (approximately 38 °C) and an outside temperature (typically about 25 °C). Highly thermally resistant foam insulates the test section. The foam has thermal conductivity coefficient (K) of 0.035 W/m-K and a 0.0254 m cross-sectional thickness (L). The cross-sectional area of the bottom section was 0.0503m^2. Using equation 3.3, the conduction loss to the bottom wall in low Reynolds number was found to be 1.3753 W or 2.5% of whole power supplied.

$$Qcon = \frac{kA(Ts - Ta)}{L} \qquad \text{Equation 3.3}$$

Other similar conduction loss were also expected through the side walls but were small due to the small surface area of the side walls. This conduction loss from all side walls was calculated to be around 1.290 W or 2.5%. The absolute loss are very likely to increase slightly at higher Reynolds number flows due to the higher blower compression energy added into the system which drives the test section temperature slightly higher. At the same time, the outside temperature still remains approximately constant. As a result the magnitude of conduction losses are expected to increase slightly. However, due to higher electrical heating levels the percentage loss is expected to decrease. Thermal radiation loss was also considered to be factor in the heat transfer analysis. Top surface of the test section was exposed to inlet air flow within the plenum. The temperature difference between inlet

air and top surface of plate were the major driver in this heat loss. Equation 3.4 was used to calculate the magnitude of the radiation loses.

$$Qrad = \frac{A\sigma(Ts^4 - Ta^4)}{\frac{1}{\varepsilon a} + \frac{1-\varepsilon s}{\varepsilon s}(\frac{Aa}{As})}$$ Equation 3.4

CHAPTER 4
EXPERIMENTAL RESULTS

In this experiment, an extensive set of heat transfer results and pressure drop parameters were acquired using a conventional high solidity pin fin array combined with the internal incremental impingements method.In addition, the newly formulated idea of using variable holes size distributions was applied by testing and analyzing almost 30 different configurations. The variable hole size method was included because variable holes sizes gives more control to the designers to adjust the mass flow rate and pressure drops of the array for achieving more closely optimum results for internal cooling. The heat transfer and pressure drop measurement were obtained over Reynolds numbers between 5000 to 75,000 in all configurations. The pressure drop through the array of each configuration is presented as function of the downstream distance in inches. Also the discharge coefficient (Cd) of the arrays has been calculated and the measured value was compared with the discharge coefficient of the top plate alone to ensure consistency in estimating flow splits in the array. Furthermore, the thermal effectiveness was also determined in all tested configurations. This row by row effectiveness distribution was presented in a dimensionless parameter (ε). In addition, the Nusselt number (Nu), another dimensionless heat transfer variable was calculated and reported as a function of downstream plate distance or row location and Reynolds numbers run in each variable hole size configuration tested. The fiction factor (f) resulted in each test is also reported

as function of the flow Reynold number. The cooling parameter obtained in this internal cooling experiment was also included in this report. Since the number of tests conducted over these 30 different configurations is quite large, a reduced number of configurations were selected and compared in this report to illustrate sufficient information on heat transfer and pressure drop. These heat transfer and pressure drop results are presented as a function of the array position and flow condition. A similar manner was also chosen to report other critical flow and heat transfer parameters such as Nusselt number (N_U), friction factor (f) and discharge coefficient (Cd).

4.1. Friction Factor

The flow friction factor was investigated in all incremental impingent test runs in this research project. Some of the result founded are presented as a function of array Reynolds number in figure 4.11 to compare them with an early study for a high solidity pin fin array. Early researchers (see Busche et al. [2]) indicated that the incremental impingement method may have a low flow friction factor value. indeed, Figure 4.11 provides evidence of that fact. The flow friction factor for the high solidity is quite elevated compared with any incremental impingement configuration in the plot. The lower Reynolds number condition are specifically where the incremental impingement method hold the greatest benefits over the high solidity pin fin array regarding friction factor or array pressure drop.

$$f=\frac{\nabla p}{\frac{1}{2\rho Vmax^2}*Nrow} \qquad \text{Equation 4.1}$$

$$f = 1.72ReD^{-0.297} \qquad \text{Equation 4.2}$$

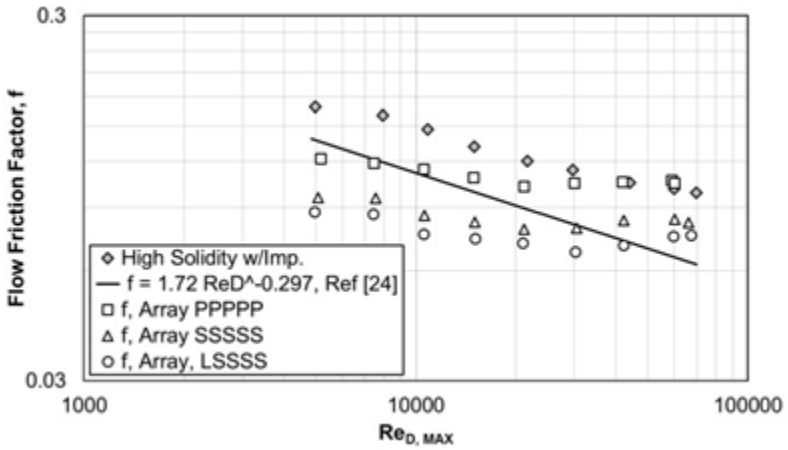

Figure 4.1. The Flow Friction Factor of the Incremental Impingement Versus the High-Solidity Pin-Fin Array.

4.2. The Flow Discharge Coefficient (C_d)

The discharge coefficient (C_d) of the impingement holes was another critical parameter evaluated in this experiment. The discharge coefficient is the ratio of actual mass flow to the ideal mass flow through the impingement hole inserts. Therefore, it is sometimes useful to model the flow performances of holes and compare the average Cd for the array with the top plate Cd test results. Developing a method to estimate flow rates within an array is critical to estimating the local heat transfer coefficient and thermal effectiveness level. Correlating the average Cd values of various experimental configurations with the early study for top plate alone was important objective. This provides a measure of the accuracy of estimating flow splits within the array based on an array average Cd. The C_d values of all hole size arrangement used in this test were acquired in a separate test prior the heat transfer test using only the top plate. These results are provided in figure 4.2 without bottom section attached. The discharge coefficient (C_d)

measures in for small, medium and large (S, M, L) hole sizes are plotted against mass flow rate for each case in the figure 4.2. Additionally, Cd determined for all small hole configuration acquired during heat transfer is mated to show consistency with complete array flow using local static pressure with the array.

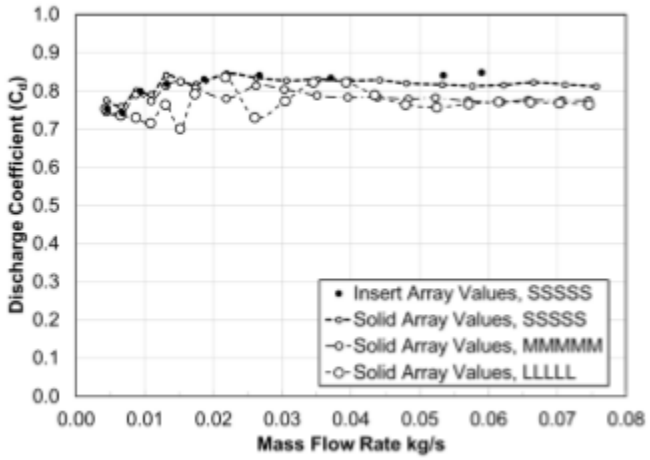

Figure 4.2. The Discharge Coefficient (C_d) of the Incremental Impingement and High-Solidity Array as a Function of Mass Flow Rate (kg/s).

4.3. Pressure Drop

Pressure drop distributions over the complete array surfaces were acquired using static pressure taps located both near pin stagnation faces and in the middle of the flow channel, between pins, to determine the stagnation and static pressure drop inside the array. There were 7 pressure taps placed the top edge of stagnation point upstream of each pin to measure the precise rise of the stagnant pressure. Another 9 pressure taps were located right on the flow channels to capture the static pressure of fluid in the each row. Both the stagnation pressure taps and the static taps were equally spaced about 1.074 inches in the streamwise direction. Those (16) closely spaced pressure taps were able to allow

documentation of the streamwise pressure distribution throughout the testing. The readings were acquired by referencing each pressure tap with the plenum pressure.The plenum to atmospheric pressure difference referenced to a barometer reading allowed the determination of the absolute pressure at each tap location.Then, the static pressure change of bulk fluid flow was used calculated the flow distribution through each row of holes (5) in the array. Furthermore, a maximum velocity (V_{max}) and air density, based on all the array flow directed through the minimum area in the last row was used to determine dimensionless the pressure coefficients of the flow through the array. This specific calculation is illustrated in equation 4 on the next page.

The very broad range of heat transfer and fluid flow variable acquired in these experiments is much too large to present in this report. The thirty different hole-size configuration were tested and analyzed in this experimental program resulting more than 140 different test data sets. Therefore, only of four test configuration are included in this report for simplicity to clarify the impact of variable hole-size configurations on the heat transfer and fluid dynamics. The aim of this report is to present the influence of the variable holes size arrangements on the internal cooling to help enable the optimization of the internal cooling distributions while effectively managing the channel pressure drop. The selected four hole-size configurations include in this report were SSSSS, PPPPP, LSSSS and MSSSS.

4.4. The Static Pressure Field in the Array

The static pressure field of the flow was measured for all test condition and configuration using eight static pressure taps located right in the flow channels in each row. The measured pressure values for the SSSSS configuration is plotted in figure 4.2 as function

of the array's streamwise distance in inches. This figure is presented to provide some insight about the pressure drop in the array particularly at high Reynolds number flow conditions.

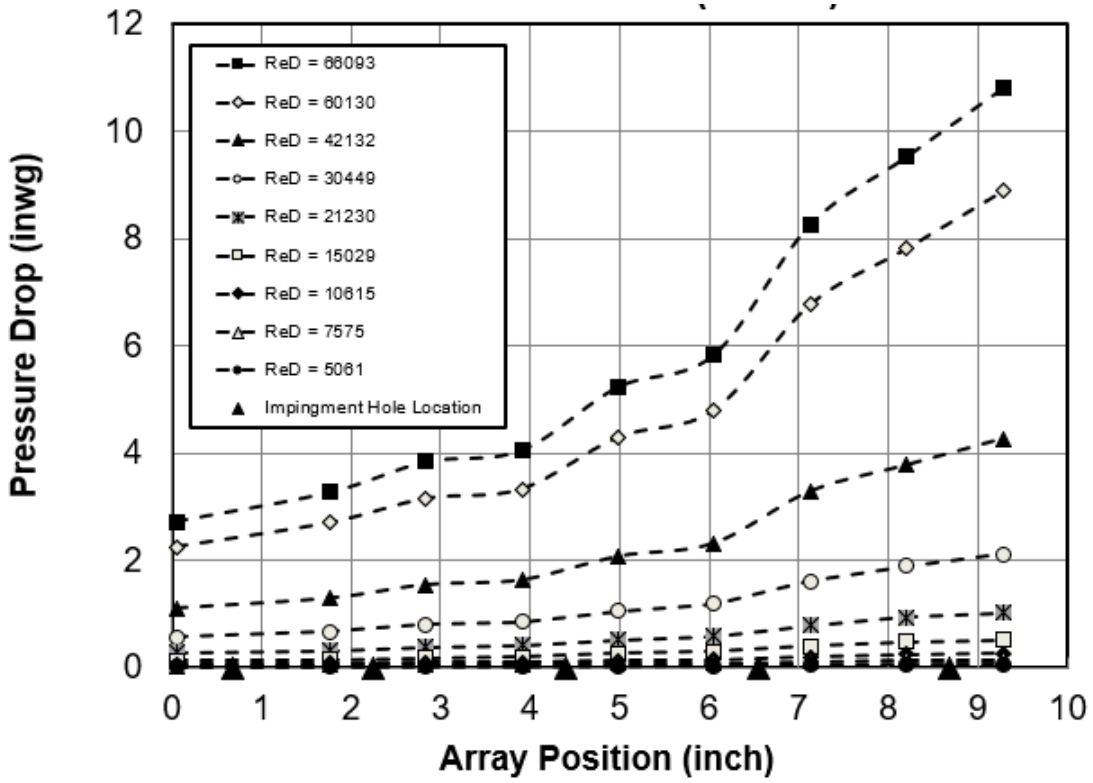

Figure 4.3. The Pressure Drop of the SSSSS Hole-Size Configuration.

The static pressure distributions in figure 4.3 show that dramatic pressure variations exist cross high through low Reynolds number. Lower Reynolds number regimes display only a slightly drop in the overall static pressure cross the array. In contrast, the higher Reynolds number flow shows a dramatic increase of inlet plenum to local static pressure drop in these incremental impingement arrays. For example, the mid range Reynolds number of 21000 results only show a static pressure drop of around 2 inches water gauge (~498 Pa) compared to static pressure drop for the 66,000 Reynolds number with a static

pressure of 10 inches water gauge through the last row.Also, this static pressure drop in the array appears to be non-uniform especially after the third row. It seems the fluid pressure drop spiked beyond row 4 in all flow conditions. However, this decrease is quite dramatic at higher Reynolds number. For instance, the pressure gradient between row 4 to end of the array can be approximated around 1.333 inches water gauge for every inch distance in the streamwise direction at the highest Reynolds number, 66,000.On the other hand, only a 0.4666 inches water gauge pressure drop exists in per inch of streamwise distance in the array when it comes at the lower Reynolds number of 42,000. This shows a similar trend of static pressure drop exists at lower Reynolds numbers, especially in the last rows, but the magnitude of pressure drop scales much lower compared with the higher Reynolds numbers.This rapid static pressure decrease in the last few rows is caused by the increase mass flow rate. In fact, analysis of experimental results showed that almost 50% of the total mass flow in all hole size arrangements was discharged in last two rows effectively doubling the streamwise flow rate. The increased mass flow distribution through the last two rows results in increased levels of local Vmax. Since pressure drop scales on Vmax the pressure drop naturally increases dramatically at the higher flow rate condition.

4.5. Pressure Coefficient

The pressure coefficient (C_p) is a dimensionless parameter used to scale the pressure variation existing across the array during the particular test condition. The empirical formula used to calculate the pressure coefficient in this study is provided in Eq 4.3 . This pressure gradient existing within the array is main driver of fluid flow, both within the array and a cross the impingement holes that drives the performance of the overall heat transfer in the incremental impingement method.

$$Cp = \frac{\nabla P}{\frac{1}{2} * \rho * Vmax\text{^}2}$$ Equation 4.3

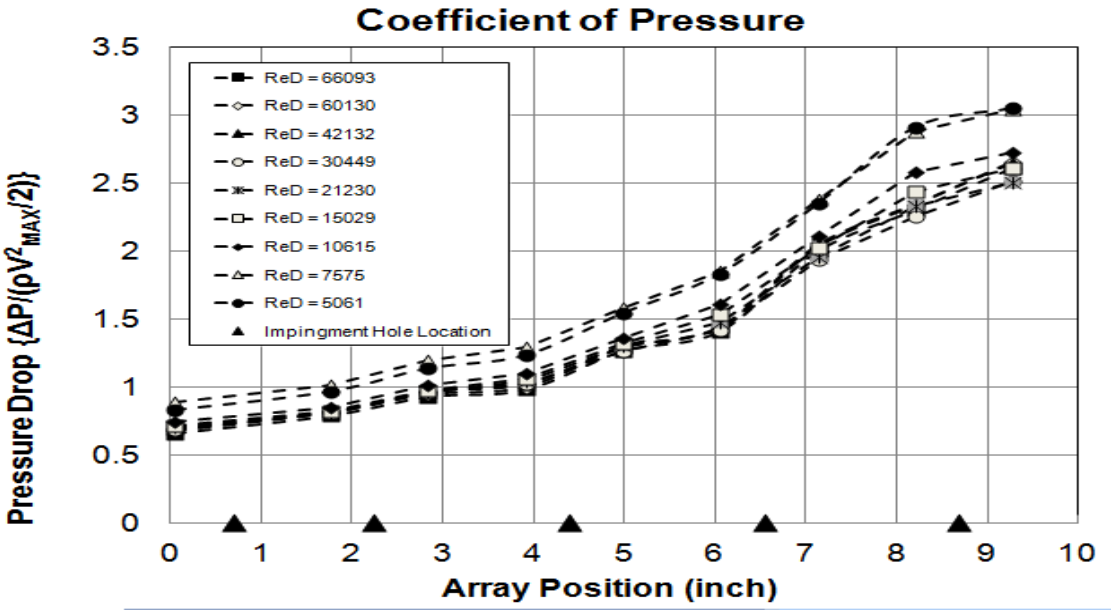

Figure 4.4. The Pressure Coefficient for All Small Hole Size (SSSSS) Configuration.

Figure 4.4 shows the dimensionless pressure coefficient for the SSSSS hole-size arrangement versus the streamwise distance.This pressure coefficient plot follows a very similar trend of a continuous drop in pressure toward the downstream region of array due to the increasing mass flow rate. Furthermore, the pressure coefficient for the SSSSS configuration in figure 4.4 also shows a greater dependence of the array pressure field on the array Reynolds number. In addition, pressure drop increases rabidly right after row 4 and beyond due to the increased velocities with accompany higher flow rates and the resulting higher pressure drop which scales on V_{max}^2 . The downstream pressure drop visible on figure 4.4 suggests the mean velocity of flow increases with the additional fluid flow, which causes increases acceleration between adjacent pins and increased separation

loses downstream for minimum areas. This idea supports the early literature findings where heat transfer increased rapidly in the first few rows due to flow acceleration caused by pin and wake blockage increasing velocity rapidly in the first few rows. Although the cause of acceleration in the aft section of the array is largely due to increased mass flow rate, resulting enhancement of heat transfer in the two cases is similar.

The pressure drop increase a cross the arrays was also investigated with respect to variation in the row hole sizes in conjunction with other heat transfer parameters. The overall array pressure loss is the sum of both the hole injection pressure loss and the channel flow pressure loss components. Therefore, plotting and comparing the pressure loss coefficient graphs for each varied hole configurations provides an interesting insight into the role of injection hole size on overall pressure loss. Figure 4.5 shows the pressure coefficient of the all petite (PPPPP) hole size array configurations. This hole size has the smallest diameter and the minimum injection area of the all test configurations. As a result, the pressure drop across array is the highest among the configurations tested in this study. Also, the pressure coefficient distribution presented in figure 4.5 show the influence that hole diameter has on pressure drop suggesting a substantial pressure loss occurs through the hole addition to the downstream channel flow. Although the size difference of SSSSS (.295 inch diameter) and PPPPP(0.25inch diameter) is only 0.045 inches in the diameter, but the pressure drop resulting by this difference is quite substantial with the PPPPP configuration showing a much higher pressure drop. The pressure coefficient (C_p) for the PPPPP array hole size shown in figure 4.5 indicates the pressure coefficient reached almost 3.9 at the last row for the lowest Reynolds number. The increased array pressure drop seen in PPPPP shows the strong influence of the jet injection hole diameter on the overall

pressure drop coefficient. In contrast, the SSSSS pressure coefficient distribution have a notably lower starting value and the magnitude barely reached 3.0 last row for lowest Reynolds number flow.

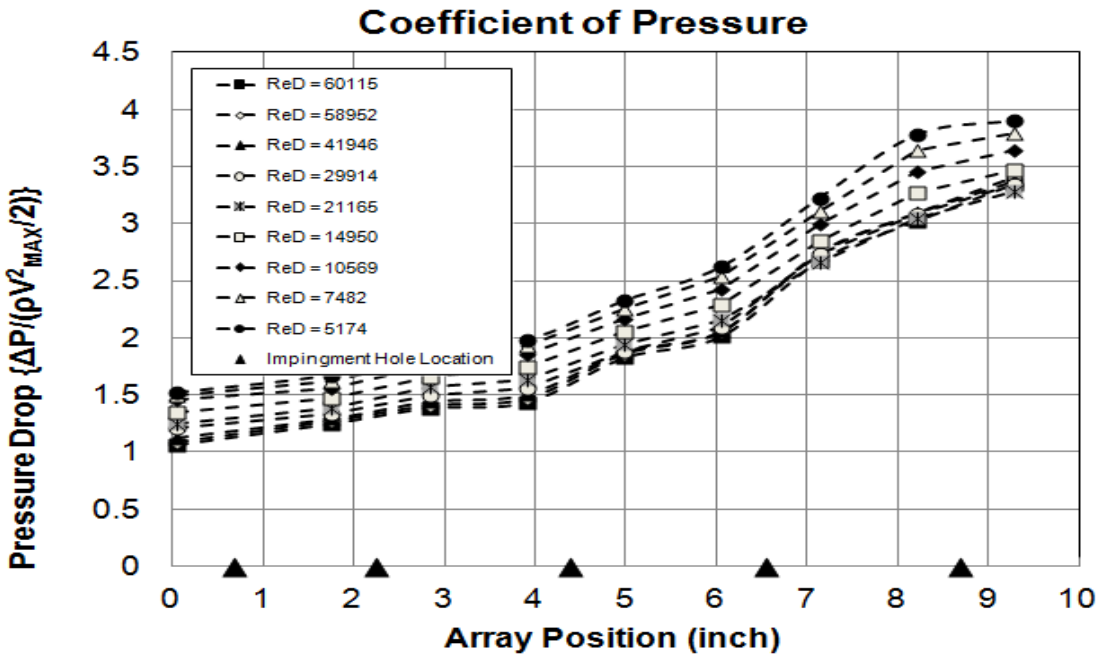

Figure 4.5. The Pressure Coefficient of the PPPPP Array Configuration.

The MSSSS was another selected hole size variation tested in this experiment. The pressure coefficient plots of MSSSS are provided in figure 4.6 showing all four Reynolds numbers. In this particular configuration, the medium size (0.351 Inch) diameter hole sized was placed in the first row impingement holes while all downstream rows remained at the small hole diameter (0.295 Inches).The flow distribution calculation indicated 19.7% of the overall mass flow rate through this configuration was injected through the first row of holes. Around 14.8% and 17.3% of the total mass flow went through second and third rows, respectively. The last two rows in the array accommodate almost 48% of the total mass

flow rate injected into arrays. The extra mass flow rate in last two rows results in a dramatic increase in the pressure drop shown in figure 4.6.The fraction of the flow distribution in each hole remains nearly constant at all Reynolds numbers,even though, the mass flow rate change between the lowest Reynolds number of 7500 and the highest Reynolds number of 60000 scaled on Reynolds number. This increase in the mass flow rate in last two rows resulted in a large pressure over the last few rows similar to the other incremental impingement configurations.

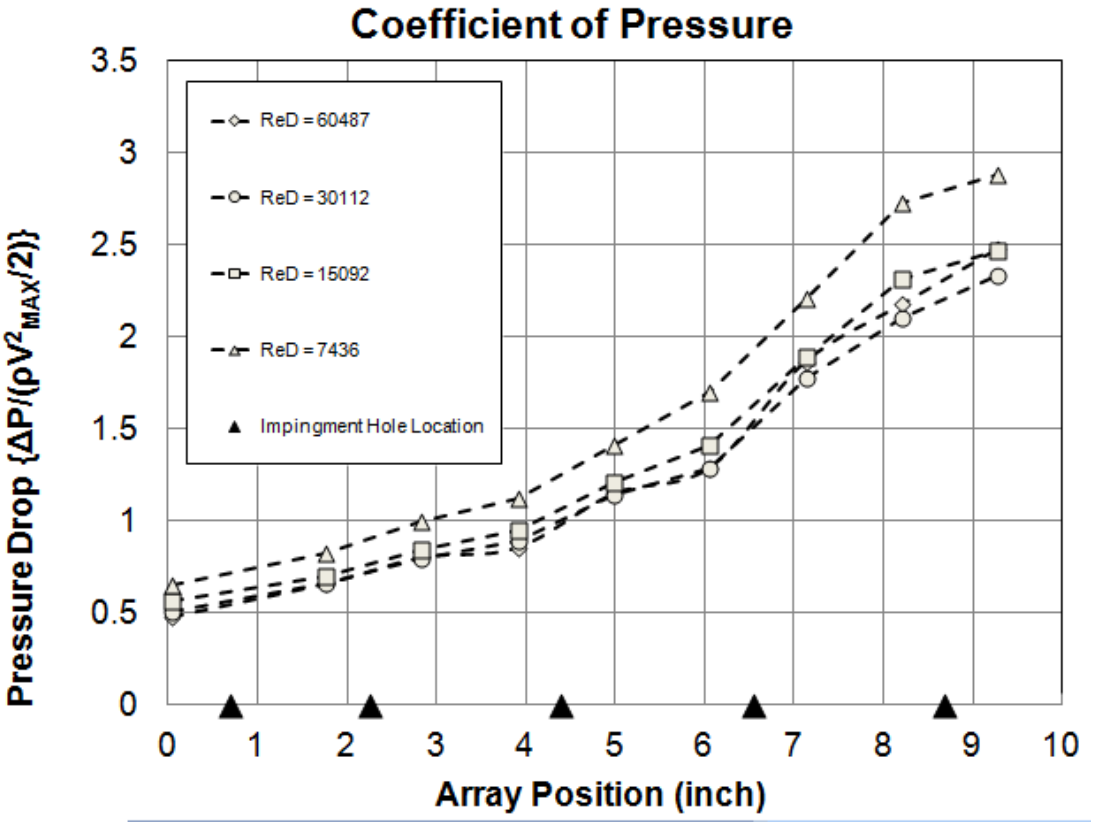

Figure 4.6. The Pressure Coefficient Distribution for the MSSSS Hole-Size Configuration.

The overall pressure coefficient of MSSSS is notably lower compared with the other two configuration discussed earlier. The difference in this configuration and the

SSSSS configuration was the medium holes placed in the first row while the other rows remained the same.

The pressure coefficient results of LSSSS hole size arrangement is given in figure 4.7. In this variable hole size configuration, the largest hole diameter (0.417 inches) in this experiment was selected for all holes in the first row while maintaining all remaining downstream rows at all small hole size (0.295 inches). As a result, more than 22% of total mass flow rate was injected through the first row.It appears that this geometry adjustment reduced second and third row mass flow rates to around 13% and 16 % of the total flow. The far downstream rows were not affected by this change at all. The four and fifth rows maintained a constant flow injection percentage of 21% and 27% in all four configurations reported here. This configuration was found to have the lowest pressure drop among all the tested geometries. The ability to specify the coolant flow rate is a critical advantage for internal cooling using the incremental impingement method. The extra coolant mass flow can be directed toward the sections of the gas turbine component with the greatest cooling demand by adjusting the hole sizes.

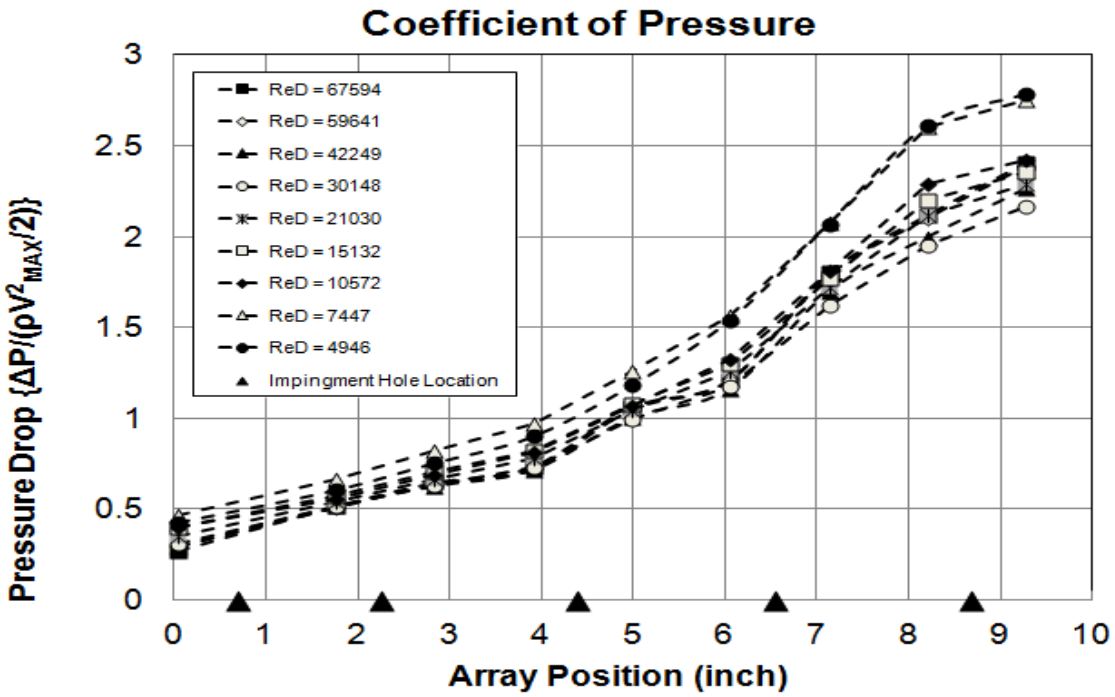

Figure 4.7. The Pressure Coefficient of the LSSSS Array Configuration.

4.6. Heat Transfer

This section will discuss the heat transfer results obtained in this experiment using the four different hole size configurations selected for comparison as a function of the different Reynolds number flow conditions. The selected hole size arrangements included SSSSS, PPPPP, MSSSS and LSSSS. The heat transfer results for each hole configuration is presented in two dimensionless heat transfer parameters, heat transfer effectiveness (ε) and the cooling parameter (ξ), at either 9 or 4 selected Reynolds numbers. The hole size configurations such as SSSSS and PPPPP with uniform hole distributions were tested at nine Reynolds number ranging from 5000 to 75000 while the variable hole size models were only tested only four Reynolds numbers starting from 7500 to 75000. The results are presented quantitatively using two dimensionless thermal transfer parameters, the thermal transfer effectiveness and the cooling parameter are calculated using equations 4.4 and 4.6.

The thermal transfer effectiveness is the ratio between the plate surface temperature (Ts) and the fluid bulk temperature (T_b) with both subtracted fluid inlet temperature (T∞). On other hand, the cooling parameters is calculated using the ratio of initial Nusselt number of air (Nu_0) to bulk fluid Nusselt number (Nu). In addition, this ratio is multiplying by one minus the heat transfer effectiveness (1-ε).

$$\varepsilon = \frac{T_b - T_\infty}{T_s - T_\infty} \qquad \text{Equation 4.4}$$

4.7. Heat Transfer Calculations

The thermal effectiveness and the cooling parameter of the high solidity pin fin array obtained in an early study, presented present in figure 4.8 and 4.9 for use as a baseline to compare with current results. These figures illustrate the general heat transfer behavior of the high solidity pin fin array with only a single row of coolant jets placed at the array inlet. Both the thermal transfer effectiveness and the cooling parameter indicated decreased heat transfer capacity as air moved toward the downstream as it continues to pick up thermal energy through the array. Heat transfer results of four selected variable hole size incremental impingement configurations are presented in this section for comparison with the high solidity array baseline result. The high solidity array test was conducted with a single initial injection row without any additional impingement air added throughout array. The baseline heat transfer results in figure 4.8 and 4.9 were included to document the cooling advantage of the incremental air replenishment method over the high solidity pin-fin array.

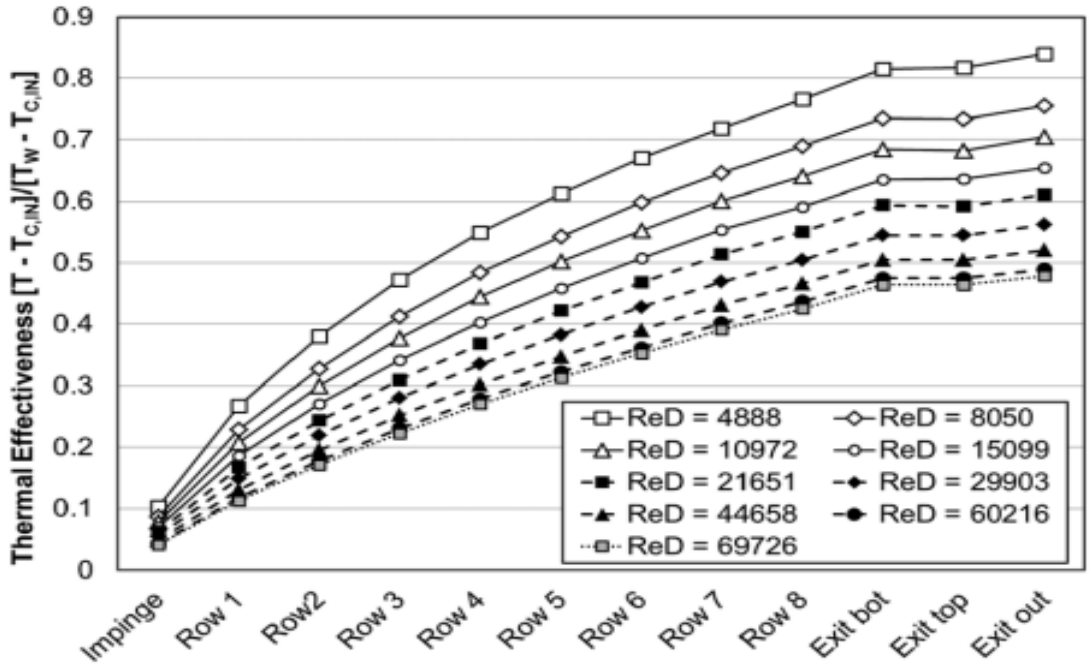

Figure 4.8. Thermal Effectiveness of High-Solidity Baseline from Refer [2].

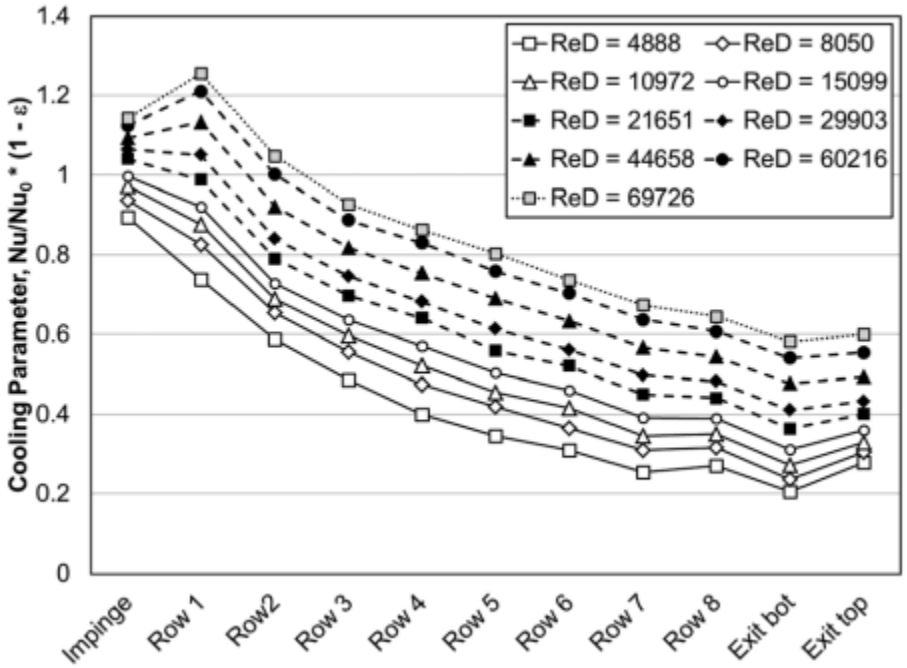

Figure 4.9. The Cooling Parameter of the High-Solidity Array Baseline from Refer [2].

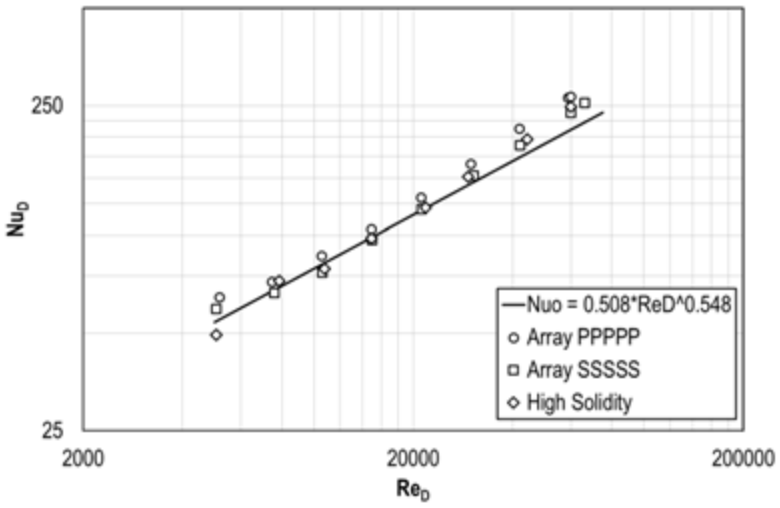

Figure 4.10. Array Nusselt Number versus Reynolds-Number-Based Nusselt Number of Both High-Solidity Pin-Fin and Incremental Impingement Array Results.

The array averaged Nusselt number is a very useful heat transfer parameter for comparing different cooling methods. Both Nusselt number and cooling parameter, based on equation 4.4 and 4.5, are presented as function of Reynolds number. The resulting values from these calculation are plotted in figures 4.11,4.12 and 4.13 to illustrate the variation in heat transfer between the incremental impingement and high solidity pin fin arrays. The Nusselt number is dimensionless heat transfer parameter as indicated by equation 4.5. A comparison between figure 4.8 and 4.11 shows the evidences of moderate advantage in average heat transfer by the incremental impingement over conventional high solidity pin fin especially at lower Reynolds numbers. However, this difference in average array heat transfer between the two disappears in the higher Reynolds number conditions.

The Nusselt number ratio of all four configurations selected were also plotted as function of the array downstream length at the figures 4.12, 4.15, 4.18 and 4.21 in the heat transfer calculations section. Reynolds number based Nusselt number (N_{uo}) was calculated

using the empirical equation provided in equation 4.7 using the flow Reynolds number while the other Nusselt number (Nu_D) is completely based on the pin diameter (D) and the heat transfer coefficient (h) as it can be seen on equation 4.5. All Nusselt ratios for each configuration reported here has shown a similar pattern of increasing toward the downstream. However, a significant fluctuation of the Nusselt number ratios has been seen at lower Reynolds number flow conditions. This Nusselt ratio fluctuation is quite significant in SSSSS configuration more than any other hole configurations. The heat transfer coefficient (h) is assumed to be main driver of this Nusselt number variations especially at low Reynolds number flows.

$$Nu_D = \frac{h * D}{K} \qquad \text{Equation 4.5}$$

$$\xi = \frac{NuD}{Nu0}(1 - \varepsilon) \qquad \text{Equation 4.6}$$

$$Nu_O = 0.508\, Re^{0.548} \qquad \text{Equation 4.7}$$

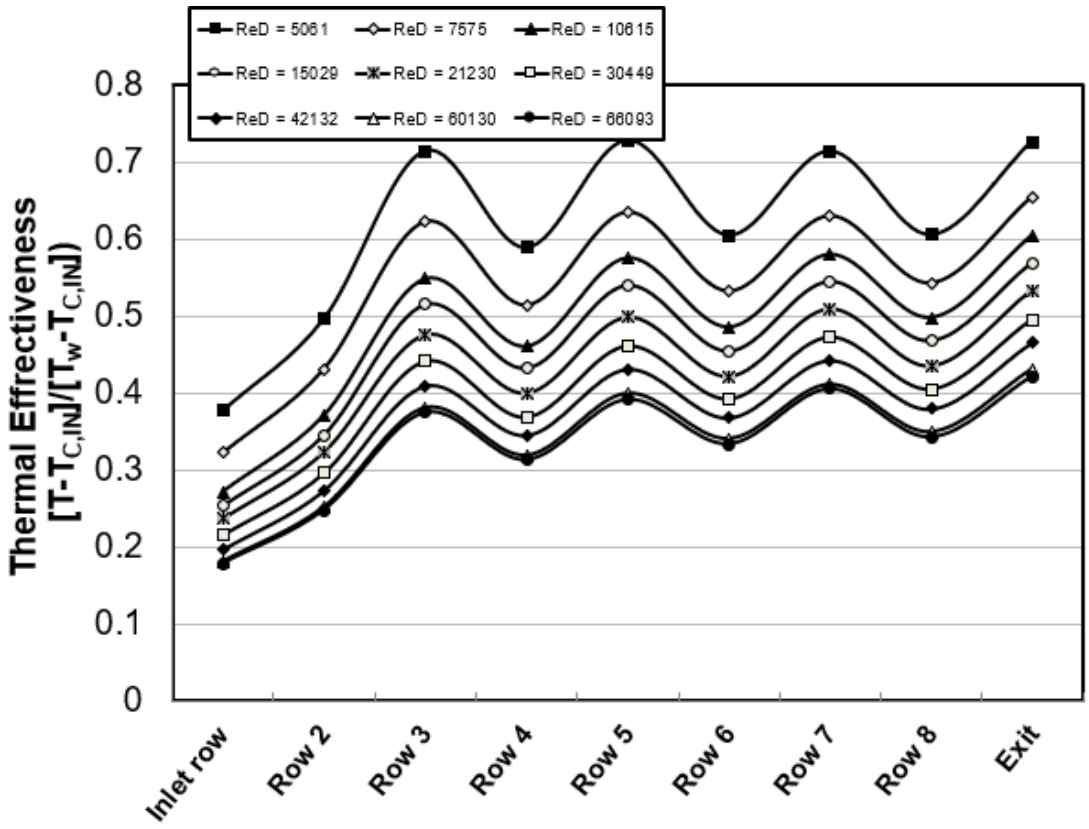

Figure 4.11. The Thermal Effectiveness of the SSSSS Configuration.

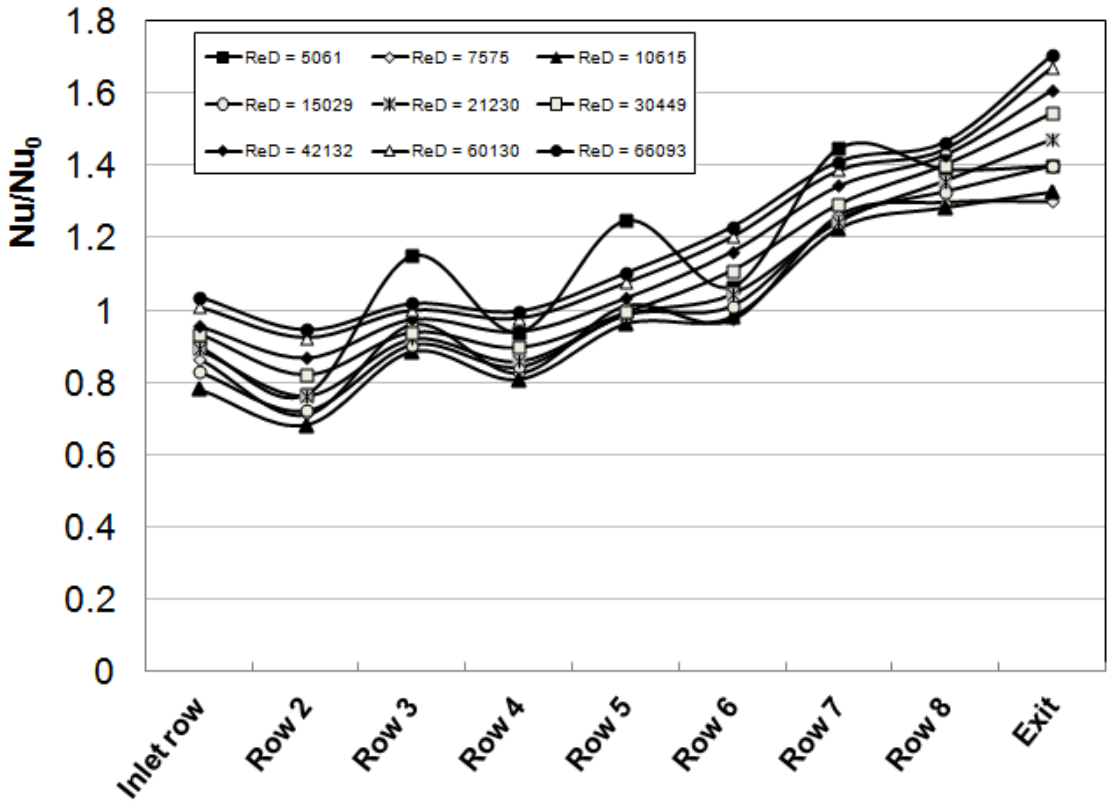

Figure 4.12. The Nusselt Number Ratio of the SSSSS Configuration.

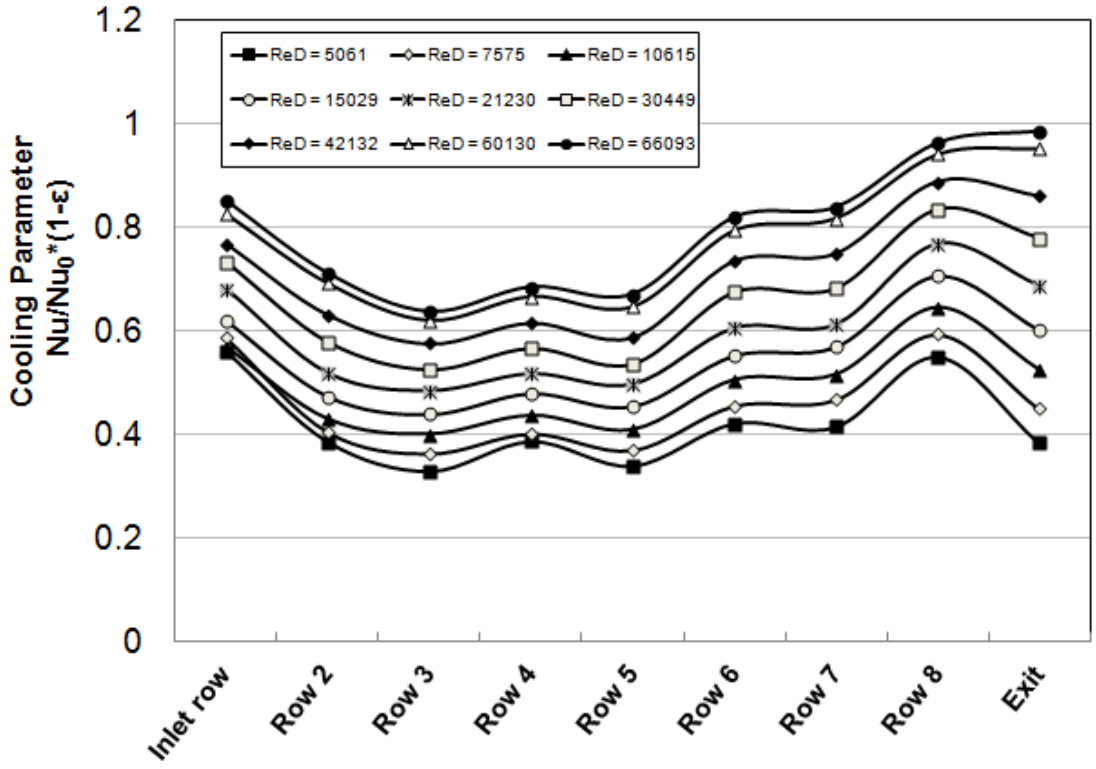

Figure 4.13. The Cooling Parameter of the SSSSS Configuration.

The influences of incremental impingement on the downstream rows in terms of the heat transfer levels is visible in both the thermal effectiveness, local heat transfer and the cooling parameters graphs in the figure 4.11,4.12 and 4.13 for the SSSSS configuration. For instance, the thermal effectiveness in figure 4.11 shows the cooling air input to the array is managed to maintain the cooling potential throughout the array. The thermal effectiveness oscillates with the input of new cooling air and maintains a reasonably consistent driving force temperature difference between the local cooling air and the wall. The thermal effectiveness levels peaked on around 0.73 at row 5 at the lowest Reynolds number and at around 0.40 for the highest Reynolds number flow. This demonstrates that the air still maintains good cooling properties even at the end of the array

in contrast to high solidity baseline in figure 4.8 where the thermal effectiveness peaked at 0.85 for the lower Reynolds number and at about 0.49 for the higher Reynolds number flow. This higher thermal effectiveness value for the baseline in figure 4.8 shows the temperature of cooling air is increasing continuously, and as a result, the ability of the air to cool the surfaces is at same time decreasing. A similar advantage of the incremental impingement over the high solidity array can be seen in terms of cooling parameter figures. The lowest value of the cooling parameter value for the SSSSS configuration is 0.328 compared with 0.25 for the high solidity array at lowest low Reynolds number for both configurations.

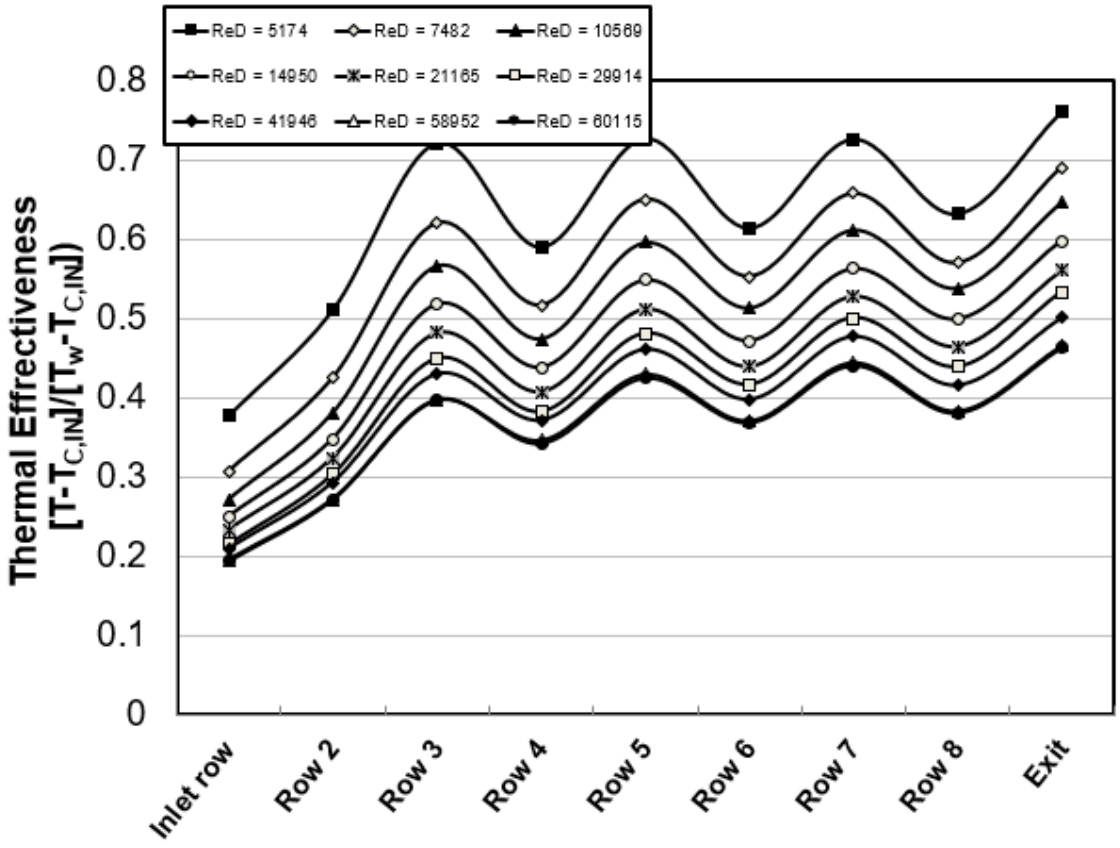

Figure 4.14. The Thermal Effectiveness of the PPPPP Configuration.

The thermal effectiveness for the PPPPP hole size configuration is shown in figure 4.14 with a very similar pattern in overall array heat transfer like SSSSS configuration discussed earlier. The thermal capacity of the air remains quite constant both of configurations when compared with the baseline model in figure 4.8 where the thermal effectiveness reached around .82 or 82% at the lower Reynolds number. The thermal effectiveness of the PPPPP configuration peaked at about 0.73 or 73% at the same Reynolds number. This difference in available temperature difference obviously gives the PPPPP configuration a large quantitative advantage over the baseline high solidity array. In addition, the heat transfer figures for the SSSSS and PPPPP configurations show the air flow heating up then the impingement jet addition cooling the air down. This process of air heat up and then cool down with coolant addition appears to be a continuous cycle throughout array's downstream length with thermal effectiveness which peak near a constant value. However, this management of the local cooling air temperature is not present in the high solidity pin-fin array on figure 4.8. Instead, the cooling air temperature is increasing row after row toward the metal surface temperature.

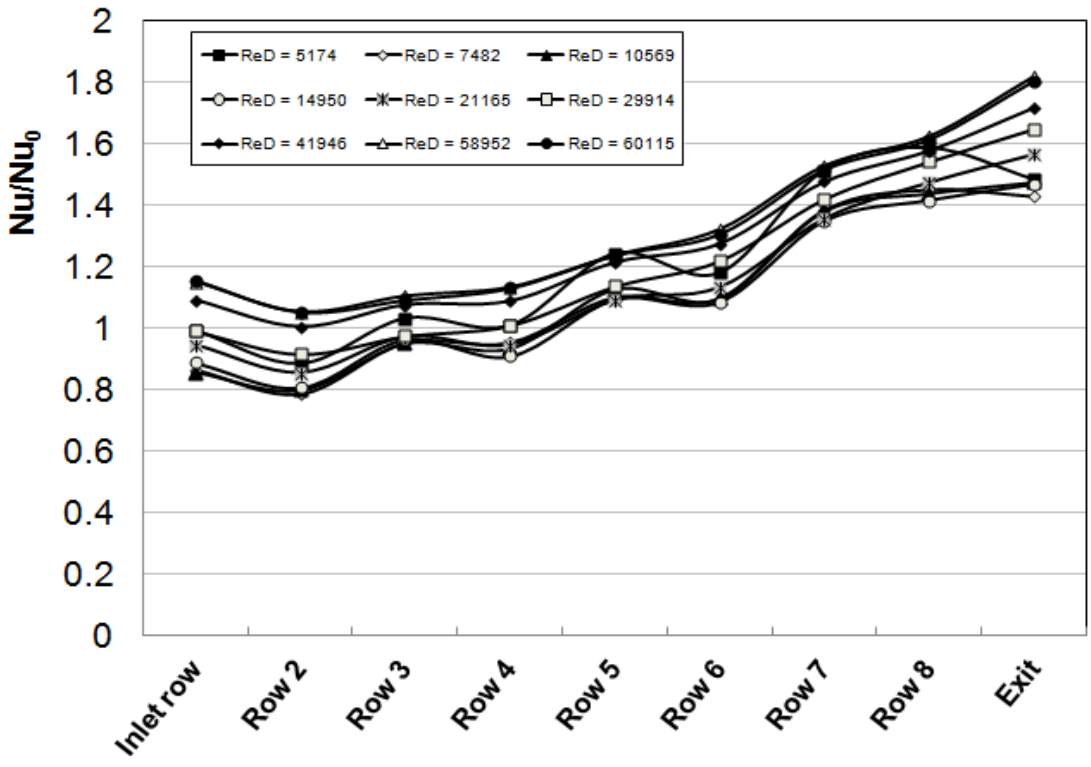

Figure 4.15. The Nusselt Number Ratio of the PPPPP Configuration.

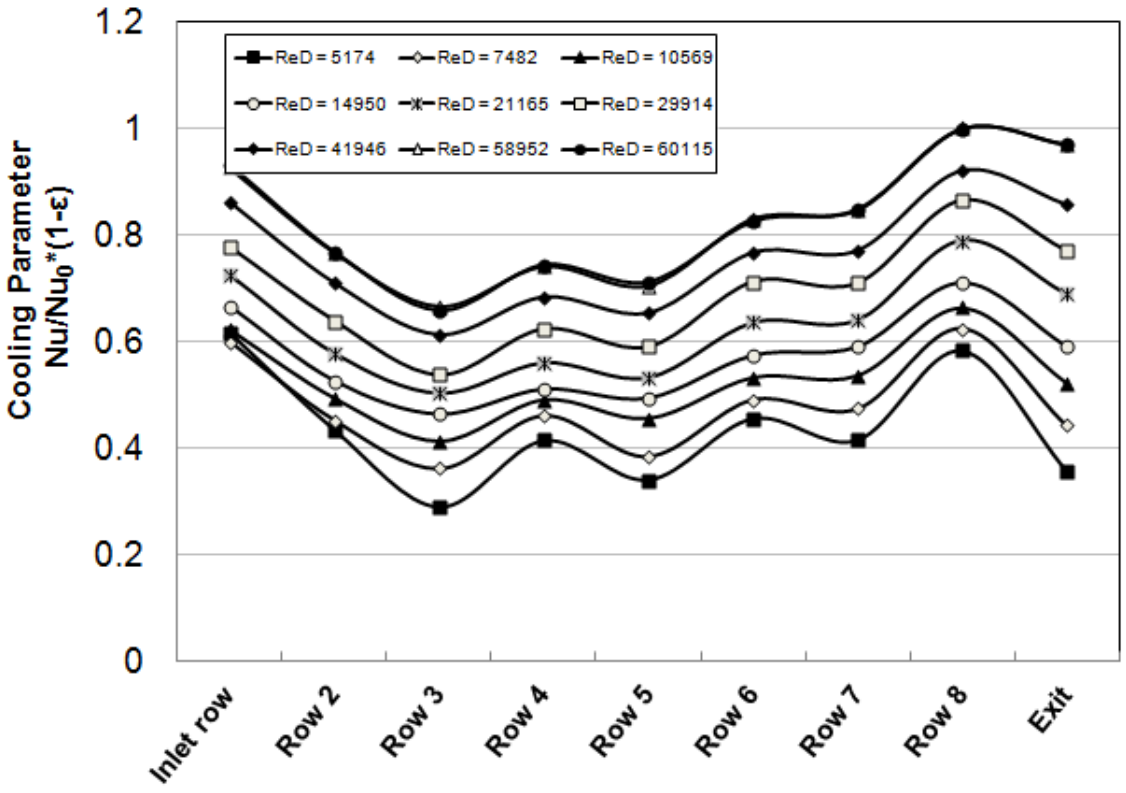

Figure 4.16. The Cooling Parameter of the PPPPP Configuration.

The highest cooling parameter was obtained for the PPPPP configuration with value of 1.0018 at the higher Reynolds number flow condition as shown in figure 4.16. The closest value of SSSSS hole arrangement was 0.94 for a similar flow condition. The cooling parameter of PPPPP peaked at about 0.587 in row 8 for the lowest Reynolds number compared with value 0.541 for the SSSSS configuration for the same row and flow condition. However, both PPPPP and SSSSS incremental configuration yielded higher value for the cooling parameters in row 8 compared with the baseline result which produced a value of only 0.25 at lowest Reynolds number.

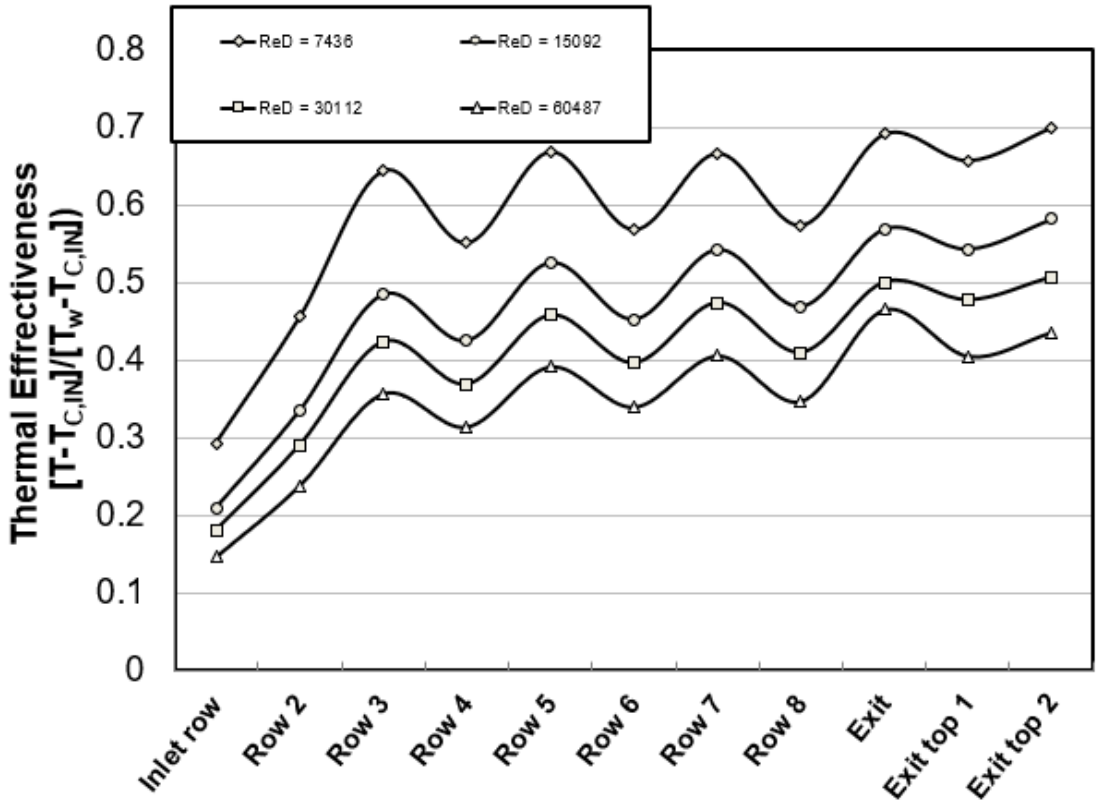

Figure 4.17. The Thermal Effectiveness of the MSSSS Configuration.

The first two configurations, SSSSS and PPPPP, evidenced the cooling advantage of variable-hole size incremental internal impingement over the high solidity cooling array. However, the variation of hole size was another feature added this experiment to allow more control in adjusting the cooling air flow where it is needed the most. A medium sized hole was placed in each hole of the first row and its thermal effectiveness is presented in figure 4.17. The result in figure 4.17 showed the thermal effectiveness, heat up of the air is little higher compared with the other configurations presented earlier such as the SSSSS and PPPPP configurations. For instance, the MSSSS data show the thermal effectiveness in third and fifth rows has risen to about 0.644 and 0.669 in 7500 Reynolds number compared to 0.6222 and 0.6346 for the SSSSS configuration at similar low Reynolds

number. A similar incremental difference in terms of the thermal effectiveness was observe between the two configuration at higher Reynolds number flow conditions. The modest increase of the thermal effectiveness for the MSSSS result can be attributed to the larger flow of cooling air injected into first the row, which increased the local heat transfer there and as a result, picked more thermal energy in initial rows. The reduced downstream flow resulted in the somewhat higher thermal effectiveness levels. Note the first row thermal effectiveness for the MSSSS configuration is the lowest compared with the other two. However, reverse has occurred in the downstream rows at all Reynolds number conditions.

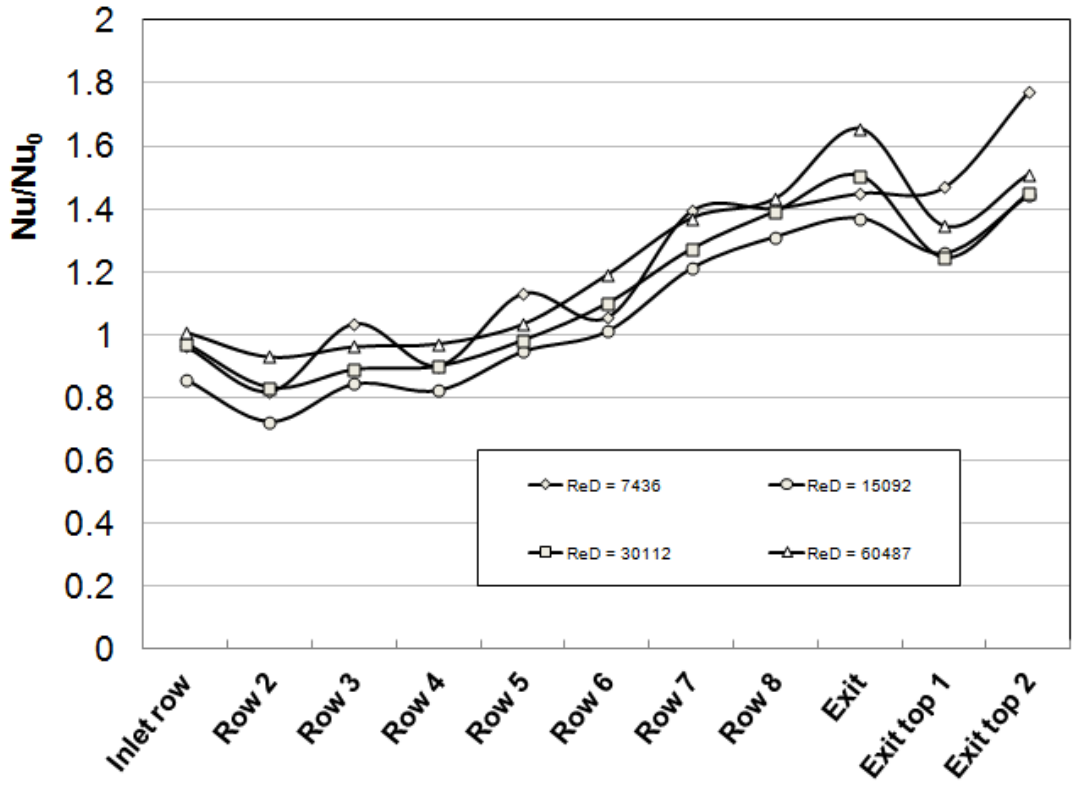

Figure 4.18. The Nusselt Number Ratio of the MSSSS Configuration.

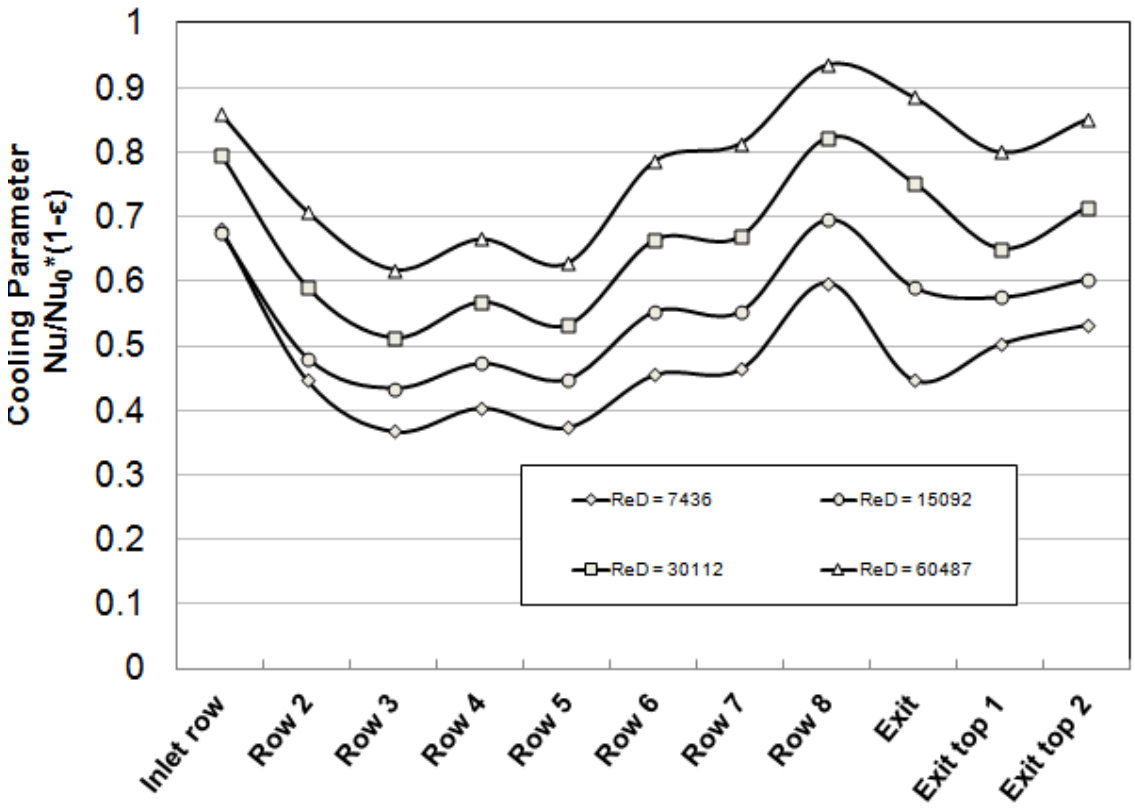

Figure 4.19. The Cooling Parameter of the MSSSS Configuration.

The cooling parameter of MSSSS is provided in figure 4.19 at the four different Reynolds numbers. This cooling parameter has indicated a slightly reduced cooling performance of MSSSS compared with other two configurations discussed earlier. For example, the cooling parameter of MSSSS in figure 4.19 was minimum at 0.3626 in third row for the lowest Reynolds number compared with 0.3679 for the same row and Reynolds number for the SSSSS configuration. This incremental difference of the cooling parameters between MSSSS and other configurations appears to be uniform in all flow conditions. The slightly lower heat transfer values of MSSSS configuration appears to related flow distribution through rows. For instance, almost 20 percent of total mass flow was injected in first row for the MSSSS while only 14 percent and 17 percent of total mass flow was

introduced through the successive two downstream injection rows. The larger mass flow rate injected on the first row very effectively cooled the first row, but this added substantial thermal energy to the air which was convected downstream, creating cooling environment with reduced thermal capacity. In fact, the MSSSS cooling parameter in the second row was determined to be 0.4461 for the 7500 Reynolds number compared with a value of 0.4044 for the SSSSS configuration at a similar flow condition.

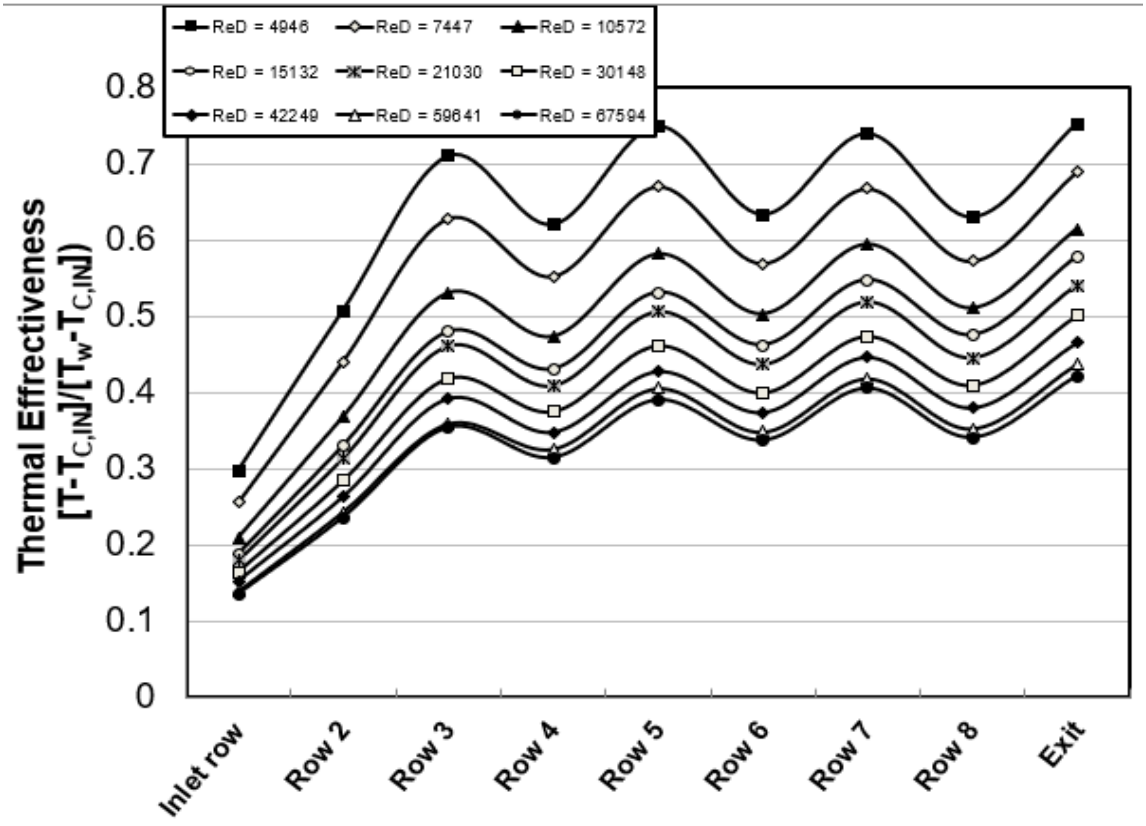

Figure 4.20. The Thermal Effectiveness of the LSSSS Configuration.

The thermal effectiveness distribution for the LSSSS configuration are provided in figure 4.20 at nine different Reynolds numbers ranging from 5000 to 75000. This figure presents is the second variable hole size experimental heat transfer result discussed in this

report. The largest diameter hole size of 0.417 inches was placed in all holes in the first row while the small (0.295 inches) diameter holes were placed in rest of the injection holes. As a result, 22% of the mass flow rate was directed through the first row of holes while the second and third rows received a smaller flow distribution of 13% and 16% of total mass.The impact of the mass flow distribution on the thermal effectiveness can be analyzed by comparing the this configuration in figures 4.20,4.21 and 4.22 with the SSSSS results in this report. The thermal effectiveness of LSSSS closely reflects this mass flow distribution. For instance, the thermal effectiveness of LSSSS only increases to around 0.2917 compared with 0.3778 for the SSSSS configuration. This heat transfer advantage for the LSSSS configuration appears to be limited to the first two rows where the highest mass flow percentage is injected. The downstream heat transfer performance of the LSSSS configuration is somewhat reduced compared with the SSSSS configuration.In fact, both the LSSSS and MSSSS heat transfer results reflect the overall mass flow distribution in the arrays. Only the first couple of rows show higher cooling parameters while the downstream rows show slightly reduced heat transfer levels.

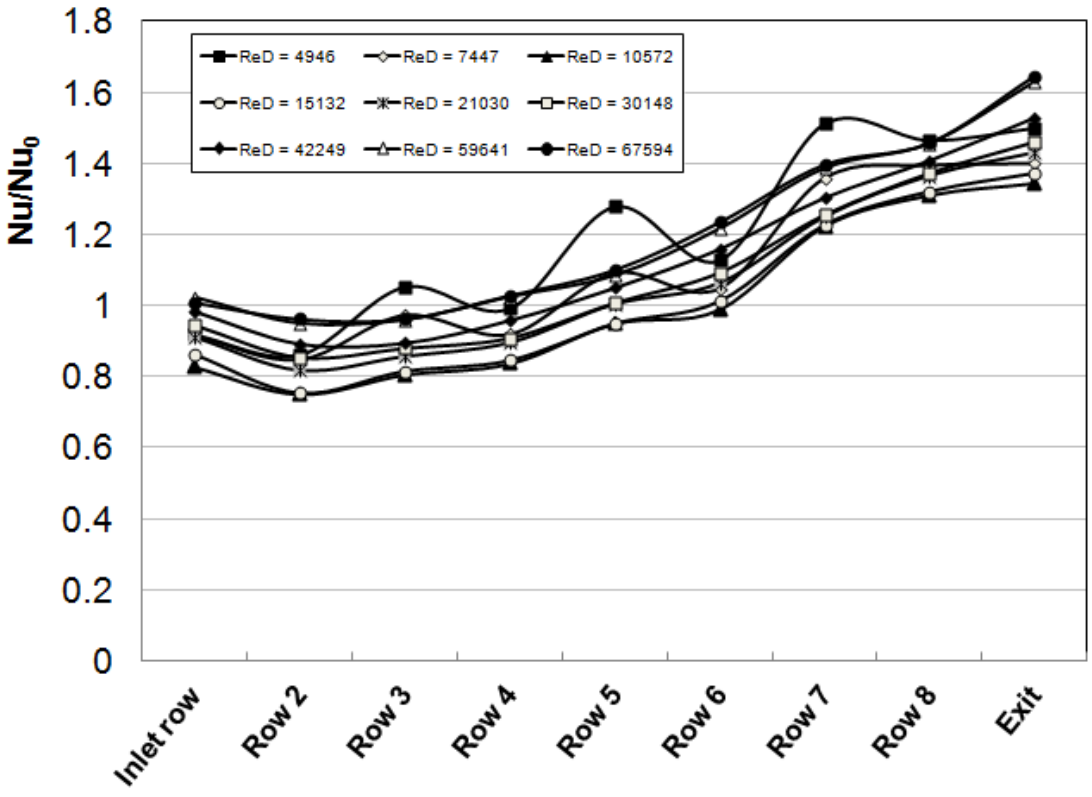

Figure 4.21. The Nusselt Ratio of the LSSSS Configuration.

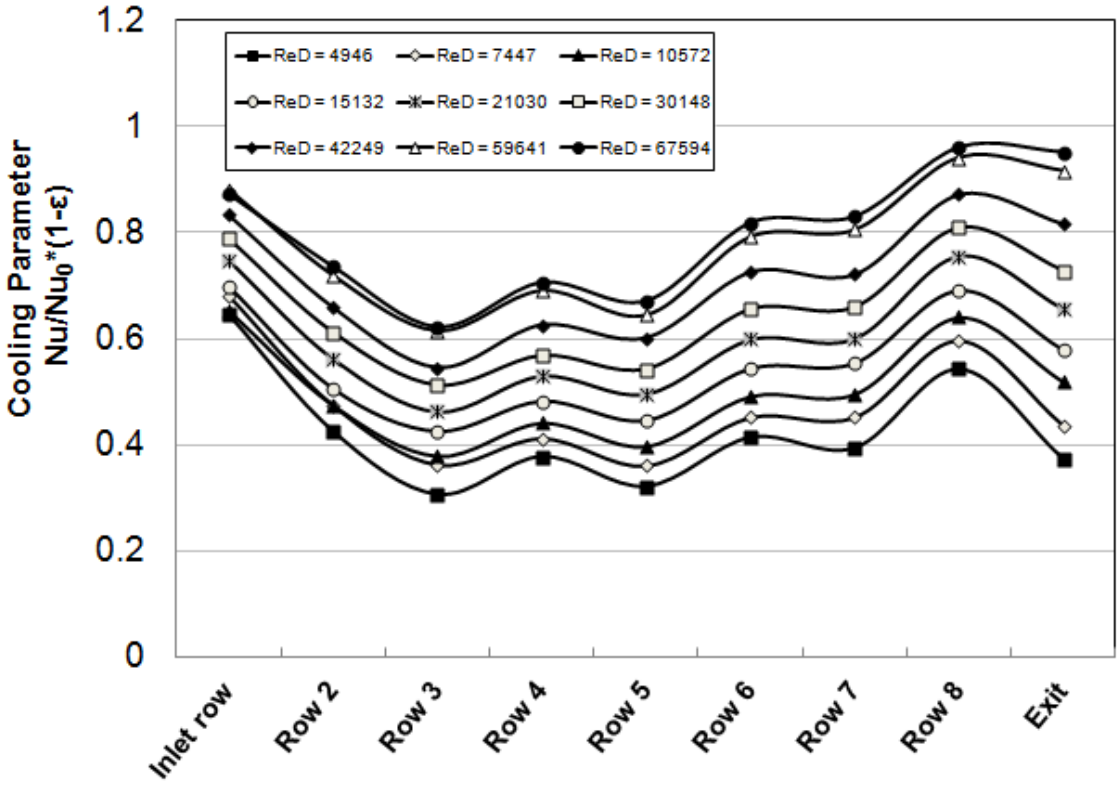

Figure 4.22. The Cooling Parameter of the LSSSS Configuration.

The cooling parameter distribution of the LSSSS configuration show in figure 4.22 illustrates a substantial initial cooling benefit resulting from the first row hole size increase. For instance, the first row cooling parameter of the LSSSS configuration stands around 0.6742 while the SSSSS configuration reaches a value of only 0.5617 for a similar flow condition for a 5000 Reynolds number. A similar incremental difference between the two configurations also exists for the other Reynolds number flow conditions. The first row cooling parameter value for the SSSSS configuration is around 0.8508 compared with 0.8722 for LSSSS at highest Reynolds number of 66000.

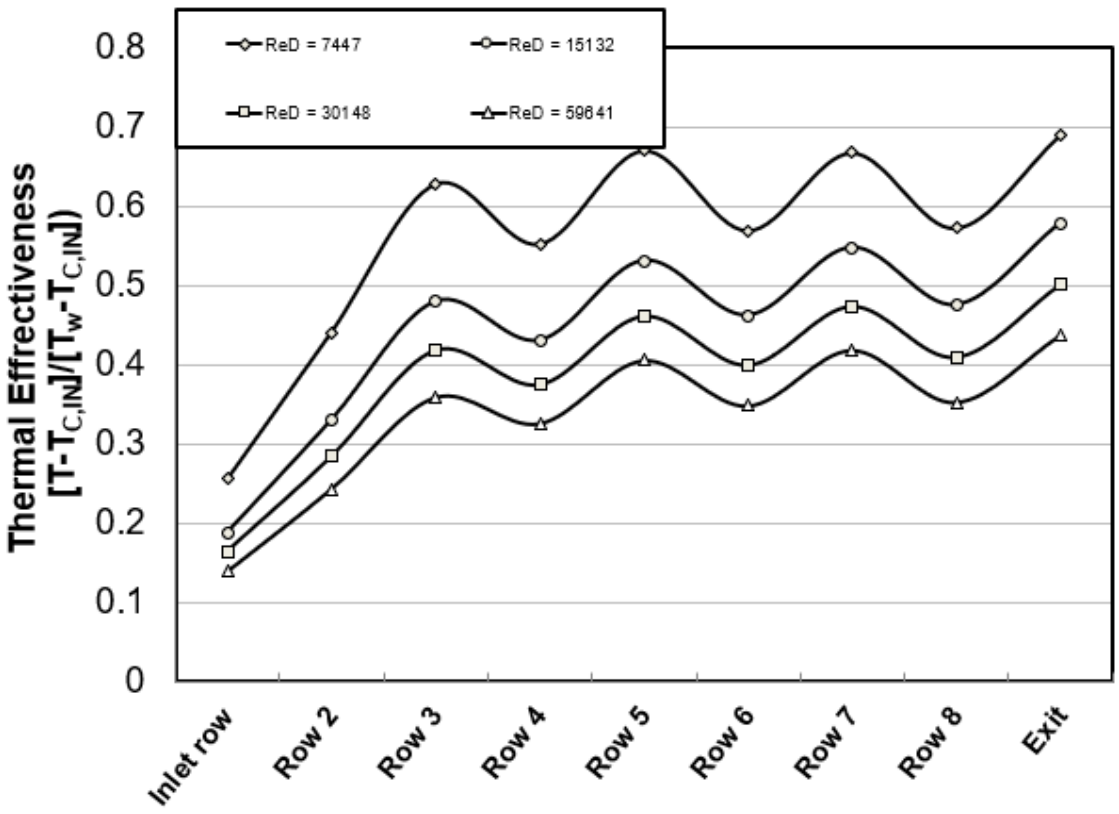

Figure 4.23. The Four Reynolds Number Presented Thermal Effectiveness of LSSSS.

The last two figures (4.22 and 4.23) were presented to compare the heat transfer effectiveness of the two variable holes configuration results. First row flow areas were varied about 30%. The injection flow area of the MSSSS was calculated to be around 0.484 inches squared in first row while the LSSSS maintained an area of 0.683 inches squared for the same row.All other parameters of the two configurations remained the same. The thermal effectiveness result presented in the above figures showed that the LSSSS configuration has slight advantage in first row over the MSSSS due the increased coolant flow. Once more, this heat transfer benefit seems to be limited only the first row. However, that advantage eroded immediately by the second row and continues through array in all Reynolds flow conditions. It appears that the large mass flow injected through

the first row of the LSSSS configuration adversely affected the downstream inject rates by reducing the relative flow area and the pressure drop available to the downstream rows. The flow restriction specifically impacted the impingement jet flow rate for the second row and third row where only 13% and 16% of flow went in the LSSSS configuration. The MSSSS has a higher mass flow rate in both of these rows,14% and 17% of total mass flow rate went second and third rows. The main idea of integrating the variable hole size style into internal impingement is give more control to designers to be able to distribute flow rate in way that matches the heat transfer requirements of the turbine blade and vanes. A vane cooling model [13] has shown certain section of these components are often over cooled while other sections are under cooled.

CHAPTER 5
CONCLUSION AND RECOMMENDATIONS

The gas turbine engine plays a very important role in today's energy needs contributing to both the aviation propulsion and power generation sectors. A well understood relationship directly couples both the power output and efficiency of a gas turbine engine with the combustion outlet temperature or Turbine Entry Temperature (TET). This relationship implies any future increase of gas turbine performance (efficiency and power output per unit flow) would require even higher TET. However, the current materials available to the engine component manufacturers cannot withstand the present turbine entry temperatures (TET) without some kind of comprehensive cooling management design in critical sections of turbine airfoils let alone the even further increase of TET. In addition, the conventional methods usually used to cool the leading edge section vanes such as showerhead arrays, which cool turbine blade and guide vane leading edge regions exposed to maximum heating, may not be prudent due to the turbulent combustion gases with particulates causing the potential of deposition in the leading edge region. Therefore, the present study was designed to investigate an alternative method to generate comprehensive internal cooling in the critical regions of turbine components while achieving higher efficiencies in terms of the coolant used and heat transfer requirements.

The use of impingement jets, incrementally integrated into high solidity pin fin arrays was the focus in the current study. High solidity pin fin arrays provide more

structural rigidity in bridging the two sides of double wall cooling methods used in turbine blades. Also, pin fin arrays effectively provide more wetting surface area to speed up the heat transfer by thermally connecting the cold side wall. Moreover, high solidity pin fin arrays also increase the heat transfer by enhancing the flow mixing within the array. In addition, the variable hole size style was also investigated in this current study to provide the designer with more control to adjust coolant flow and direct air into the undercooled areas within components. The overall results found in these experiments are very encouraging. The fluid pressure field was captured throughout the array to compare one configuration to another, and also to correlate the high solidity heat transfer to the flow variations within the array. Furthermore, the heat transfer effectiveness and the cooling parameters calculated in this experiment were presented in comparison with a baseline model experiments tested earlier. The baseline high solidity model was configured with an initial single row of impinging jets. The resulting comparison showed the incremental impingement configuration has a greater advantage over the conventional high solidity approach. The results of all the configuration showed the impingement jets continuously replenish the coolant air throughout array maintaining an almost constant thermal capacity for heat transfer.

In addition, the heat transfer advantages achieved in the incremental impingement cooling arrays have been analyzed in the last section in this report. The substantial cooling benefits of the incremental impingement configurations were discussed in depth. However, the author believes the heat transfer potential of the incremental impingement jet can be expend even further by adding a showerhead array to the current configurations. The heat transfer benefits of the incremental impingement jets can be expanded by added a

showerhead cooling array to the cooling method. This updated design might only require the addition of exit slots to discharge the spent coolant onto the near leading edge surface at an optimum angle. The object of this combined approach is to utilize the spend air of impingement cooling to provide surfaces of components with a proactive layer against the approaching combustion product gases. The film cooling slots must be placed in a region where the turbulence level is the lowest and boundary layer flow is established. The area behind the leading edge region where the flow accelerates over the surface can be a good choice to position these exit hole or slots. The author believes any further usage of the coolant air will greatly improve the overall power efficiency of gas turbine engines.

APPENDIX

Table 1. The Heat Transfer Effectiveness and the Cooling Parameter Values of the SSSSS Configuration.

Configura	II1PPPPP		II2PPPPP		II3PPPPP		II4PPPPP		II5PPPPP		II6PPPPP		II7PPPPP		II8PPPPP		II9PPPPP	
	ReD = 5174		ReD = 7482		ReD = 10569		ReD = 14950		ReD = 21165		ReD = 29914		ReD = 41946		ReD = 58952		ReD = 60115	
Paramete	ε	ξ	ε	ξ	ε	ξ	ε	ξ	ε	ξ	ε	ξ	ε	ξ	ε	ξ	ε	ξ
Inlet row	0.377	0.617	0.307	0.599	0.271	0.623	0.250	0.666	0.233	0.724	0.215	0.777	0.209	0.862	0.195	0.927	0.194	0.932
Row 2	0.510	0.433	0.424	0.452	0.380	0.493	0.348	0.526	0.324	0.577	0.303	0.638	0.293	0.710	0.272	0.767	0.272	0.768
Row 3	0.721	0.288	0.620	0.362	0.566	0.411	0.518	0.464	0.482	0.503	0.449	0.537	0.430	0.613	0.397	0.666	0.398	0.658
Row 4	0.590	0.414	0.516	0.461	0.474	0.490	0.438	0.511	0.407	0.560	0.382	0.624	0.372	0.683	0.346	0.741	0.343	0.744
Row 5	0.727	0.339	0.650	0.385	0.596	0.455	0.548	0.494	0.512	0.532	0.481	0.590	0.461	0.654	0.430	0.705	0.425	0.712
Row 6	0.614	0.455	0.553	0.491	0.513	0.532	0.472	0.574	0.439	0.635	0.416	0.712	0.398	0.767	0.371	0.831	0.369	0.826
Row 7	0.726	0.414	0.658	0.474	0.612	0.536	0.563	0.590	0.528	0.640	0.500	0.710	0.478	0.772	0.445	0.848	0.441	0.849
Row 8	0.632	0.584	0.570	0.624	0.538	0.664	0.499	0.710	0.464	0.789	0.439	0.865	0.416	0.922	0.383	1.001	0.381	1.000
Exit	0.760	0.356	0.691	0.442	0.646	0.521	0.598	0.590	0.560	0.688	0.533	0.770	0.501	0.858	0.466	0.971	0.463	0.970
Exit top 1	0.727	0.404	0.663	0.446	0.619	0.517	0.574	0.539	0.536	0.571	0.505	0.642	0.477	0.704	0.445	0.784	0.442	0.779
Exit top 2	0.763	0.389	0.695	0.478	0.656	0.511	0.606	0.559	0.561	0.639	0.531	0.693	0.502	0.772	0.473	0.866	0.470	0.868

Table 2. The Heat Transfer Effectiveness and the Cooling Parameter Values of the PPPPP Configuration.

Configur	II1SSSSS		II2SSSSS		II3SSSSS		II4SSSSS		II5SSSSS		II6SSSSS		II7SSSSS		II8SSSSS		II9SSSSS	
	ReD = 5061		ReD = 7575		ReD = 10615		ReD = 15029		ReD = 21230		ReD = 30449		ReD = 42132		ReD = 60130		ReD = 66093	
Paramet	ε	ξ	ε	ξ	ε	ξ	ε	ξ	ε	ξ	ε	ξ	ε	ξ	ε	ξ	ε	ξ
Inlet row	0.378	0.558	0.323	0.587	0.272	0.567	0.253	0.620	0.237	0.680	0.216	0.732	0.196	0.768	0.181	0.826	0.179	0.851
Row 2	0.497	0.385	0.431	0.404	0.371	0.428	0.345	0.473	0.323	0.517	0.296	0.578	0.273	0.631	0.252	0.692	0.248	0.710
Row 3	0.714	0.329	0.622	0.363	0.548	0.399	0.515	0.439	0.475	0.483	0.441	0.524	0.409	0.576	0.380	0.620	0.375	0.636
Row 4	0.589	0.386	0.514	0.401	0.460	0.435	0.432	0.479	0.399	0.516	0.369	0.565	0.345	0.616	0.319	0.666	0.313	0.684
Row 5	0.728	0.339	0.635	0.370	0.575	0.408	0.540	0.454	0.498	0.496	0.461	0.535	0.431	0.588	0.399	0.647	0.392	0.670
Row 6	0.605	0.420	0.532	0.455	0.486	0.504	0.454	0.552	0.421	0.604	0.392	0.674	0.368	0.735	0.340	0.794	0.334	0.819
Row 7	0.714	0.414	0.630	0.467	0.580	0.515	0.545	0.569	0.509	0.611	0.473	0.682	0.443	0.749	0.411	0.818	0.406	0.838
Row 8	0.606	0.547	0.543	0.593	0.498	0.644	0.468	0.706	0.435	0.767	0.405	0.834	0.379	0.888	0.349	0.942	0.343	0.963
Exit	0.727	0.382	0.655	0.449	0.605	0.524	0.569	0.602	0.533	0.687	0.496	0.779	0.466	0.860	0.431	0.953	0.422	0.986
Exit top 1	0.698	0.472	0.626	0.506	0.574	0.546	0.542	0.579	0.504	0.615	0.472	0.681	0.441	0.742	0.407	0.801	0.401	0.827
Exit top 2	0.742	0.407	0.666	0.462	0.611	0.531	0.578	0.588	0.535	0.654	0.506	0.699	0.471	0.771	0.432	0.869	0.430	0.889

Table 3. The Heat Transfer Effectiveness and the Cooling Parameter Values of the LSSSS Configuration.

Configura	II1LSSSS		II2LSSSS		II3LSSSS		II4LSSSS		II5LSSSS		II6LSSSS		II7LSSSS		II8LSSSS		II9LSSSS	
	ReD = 4946		ReD = 7447		ReD = 10572		ReD = 15132		ReD = 21030		ReD = 30148		ReD = 42249		ReD = 59641		ReD = 67594	
Paramete	ε	ξ	ε	ξ	ε	ξ	ε	ξ	ε	ξ	ε	ξ	ε	ξ	ε	ξ	ε	ξ
Inlet row	0.297	0.645	0.256	0.682	0.209	0.654	0.189	0.700	0.180	0.748	0.165	0.789	0.153	0.834	0.139	0.881	0.136	0.872
Row 2	0.508	0.424	0.441	0.474	0.368	0.475	0.330	0.505	0.314	0.562	0.284	0.611	0.263	0.658	0.243	0.719	0.236	0.735
Row 3	0.710	0.305	0.628	0.362	0.530	0.378	0.480	0.424	0.461	0.463	0.418	0.511	0.392	0.544	0.359	0.615	0.354	0.622
Row 4	0.620	0.377	0.552	0.412	0.473	0.441	0.431	0.481	0.409	0.530	0.375	0.567	0.348	0.625	0.326	0.691	0.314	0.706
Row 5	0.749	0.320	0.670	0.360	0.581	0.397	0.531	0.445	0.506	0.496	0.462	0.542	0.428	0.601	0.406	0.645	0.390	0.671
Row 6	0.633	0.413	0.569	0.451	0.503	0.492	0.462	0.544	0.437	0.599	0.400	0.655	0.374	0.726	0.348	0.792	0.337	0.818
Row 7	0.740	0.394	0.667	0.452	0.594	0.496	0.548	0.554	0.519	0.601	0.474	0.659	0.447	0.721	0.419	0.806	0.405	0.830
Row 8	0.630	0.542	0.572	0.596	0.510	0.641	0.475	0.692	0.445	0.756	0.410	0.809	0.380	0.873	0.353	0.942	0.341	0.961
Exit	0.753	0.371	0.689	0.435	0.614	0.518	0.578	0.578	0.541	0.656	0.501	0.728	0.465	0.817	0.437	0.917	0.422	0.951
Exit top 1	0.725	0.437	0.661	0.502	0.587	0.535	0.548	0.565	0.514	0.615	0.474	0.669	0.442	0.718	0.413	0.796	0.401	0.818
Exit top 2	0.769	0.454	0.706	0.489	0.626	0.519	0.582	0.581	0.548	0.639	0.507	0.689	0.466	0.777	0.440	0.853	0.428	0.876

Table 4. The Heat Transfer Effectiveness and the Cooling Parameter Values of the MSSSS Configuration.

Configura	II2MSSSS		II4MSSSS		II6MSSSS		II8MSSSS	
	ReD = 7436		ReD = 15092		ReD = 30112		ReD = 60487	
Paramete	ε	ξ	ε	ξ	ε	ξ	ε	ξ
Inlet row	0.293	0.680	0.210	0.676	0.181	0.795	0.147	0.860
Row 2	0.455	0.446	0.335	0.481	0.290	0.589	0.238	0.707
Row 3	0.644	0.368	0.485	0.434	0.424	0.512	0.357	0.618
Row 4	0.551	0.404	0.425	0.473	0.369	0.567	0.314	0.666
Row 5	0.669	0.374	0.526	0.448	0.458	0.532	0.391	0.629
Row 6	0.568	0.455	0.453	0.553	0.396	0.663	0.340	0.786
Row 7	0.667	0.464	0.543	0.553	0.474	0.669	0.406	0.814
Row 8	0.574	0.597	0.469	0.696	0.410	0.821	0.347	0.936
Exit	0.692	0.447	0.569	0.590	0.500	0.751	0.465	0.885
Exit top 1	0.657	0.503	0.543	0.575	0.477	0.650	0.405	0.800
Exit top 2	0.700	0.532	0.582	0.604	0.507	0.714	0.436	0.852

Table 5. The Heat Transfer Effectiveness and the Cooling Parameter Values of the SMSSS Configuration.

Configura	II2SMSSS		II4SMSSS		II6SMSSS		II8SMSSS	
	ReD = 7528		ReD = 14761		ReD = 30130		ReD = 60344	
Paramete	ε	ξ	ε	ξ	ε	ξ	ε	ξ
Inlet row	0.352	0.560	0.253	0.546	0.250	0.733	0.187	0.761
Row 2	0.380	0.421	0.284	0.462	0.267	0.576	0.209	0.667
Row 3	0.573	0.436	0.440	0.484	0.400	0.549	0.325	0.693
Row 4	0.512	0.416	0.401	0.467	0.357	0.564	0.299	0.670
Row 5	0.633	0.375	0.502	0.446	0.444	0.536	0.375	0.638
Row 6	0.543	0.451	0.439	0.548	0.388	0.667	0.331	0.796
Row 7	0.641	0.462	0.527	0.550	0.466	0.671	0.399	0.815
Row 8	0.554	0.600	0.460	0.685	0.405	0.820	0.346	0.932
Exit	0.670	0.449	0.560	0.579	0.496	0.753	0.425	0.934
Exit top 1	0.639	0.507	0.533	0.574	0.473	0.656	0.405	0.795
Exit top 2	0.682	0.524	0.569	0.593	0.503	0.715	0.432	0.862

Table 6. The Heat Transfer Effectiveness and the Cooling Parameter Values of the SSMSS Configuration.

Configura	II2SSMSS		II4SSMSS		II6SSMSS		II8SSMSS	
	ReD = 7583		ReD = 15036		ReD = 30363		ReD = 60958	
Paramete	ε	ξ	ε	ξ	ε	ξ	ε	ξ
Inlet row	0.362	0.576	0.265	0.576	0.226	0.679	0.185	0.762
Row 2	0.480	0.392	0.361	0.433	0.309	0.524	0.258	0.641
Row 3	0.691	0.354	0.537	0.412	0.459	0.491	0.389	0.586
Row 4	0.484	0.415	0.383	0.481	0.327	0.557	0.281	0.642
Row 5	0.610	0.447	0.490	0.513	0.417	0.597	0.354	0.716
Row 6	0.539	0.483	0.437	0.567	0.373	0.678	0.320	0.803
Row 7	0.643	0.480	0.528	0.571	0.452	0.682	0.389	0.818
Row 8	0.560	0.610	0.461	0.711	0.396	0.828	0.337	0.939
Exit	0.676	0.462	0.564	0.599	0.486	0.765	0.418	0.939
Exit top 1	0.644	0.515	0.538	0.585	0.463	0.683	0.398	0.810
Exit top 2	0.688	0.538	0.577	0.620	0.495	0.709	0.426	0.854

Table 7. The Heat Transfer Effectiveness and the Cooling Parameter Values of the SSSMS Configuration.

Configura	II2SSSMS		II4SSSMS		II6SSSMS		II8SSSMS	
	ReD = 7552		ReD = 15023		ReD = 29327		ReD = 60072	
Paramete	ε	ξ	ε	ξ	ε	ξ	ε	ξ
Inlet row	0.351	0.558	0.268	0.579	0.230	0.678	0.186	0.757
Row 2	0.466	0.387	0.364	0.437	0.312	0.523	0.260	0.633
Row 3	0.673	0.336	0.541	0.410	0.464	0.474	0.392	0.573
Row 4	0.551	0.372	0.453	0.441	0.387	0.512	0.329	0.610
Row 5	0.680	0.353	0.568	0.431	0.484	0.505	0.412	0.600
Row 6	0.494	0.449	0.416	0.541	0.359	0.646	0.306	0.760
Row 7	0.595	0.512	0.506	0.613	0.437	0.727	0.374	0.869
Row 8	0.528	0.608	0.449	0.719	0.391	0.829	0.330	0.937
Exit	0.647	0.451	0.554	0.607	0.484	0.766	0.413	0.935
Exit top 1	0.616	0.529	0.526	0.608	0.458	0.697	0.389	0.812
Exit top 2	0.658	0.480	0.564	0.615	0.491	0.725	0.418	0.868

Table 8. The Heat Transfer Effectiveness and the Cooling Parameter Values of the SSSSM Configuration.

Configura	II2SSSSM		II4SSSSM		II6SSSSM		II8SSSSM	
	ReD = 7445		ReD = 14931		ReD = 30342		ReD = 59320	
Paramete	ε	ξ	ε	ξ	ε	ξ	ε	ξ
Inlet row	0.357	0.562	0.266	0.568	0.230	0.682	0.191	0.761
Row 2	0.473	0.382	0.362	0.423	0.314	0.526	0.265	0.641
Row 3	0.682	0.339	0.537	0.406	0.466	0.490	0.403	0.575
Row 4	0.560	0.369	0.449	0.438	0.390	0.519	0.338	0.615
Row 5	0.689	0.352	0.564	0.428	0.487	0.505	0.424	0.602
Row 6	0.575	0.414	0.476	0.508	0.413	0.615	0.360	0.735
Row 7	0.679	0.424	0.572	0.516	0.497	0.628	0.435	0.756
Row 8	0.516	0.593	0.432	0.695	0.377	0.811	0.326	0.917
Exit	0.633	0.517	0.537	0.651	0.468	0.843	0.408	1.019
Exit top 1	0.600	0.505	0.507	0.580	0.445	0.669	0.385	0.811
Exit top 2	0.641	0.508	0.542	0.610	0.475	0.734	0.414	0.883

Table 9. The Heat Transfer Effectiveness and the Cooling Parameter Values of the SLSSS Configuration.

Configura	II2SLSSS		II4SLSSS		II6SLSSS		II8SLSSS	
	ReD = 7447		ReD = 14940		ReD = 30129		ReD = 59629	
Paramete	ε	ξ	ε	ξ	ε	ξ	ε	ξ
Inlet row	0.404	0.546	0.277	0.535	0.232	0.609	0.202	0.721
Row 2	0.363	0.429	0.263	0.470	0.218	0.541	0.189	0.647
Row 3	0.565	0.522	0.421	0.572	0.348	0.668	0.302	0.772
Row 4	0.536	0.441	0.407	0.500	0.339	0.579	0.296	0.703
Row 5	0.663	0.389	0.513	0.466	0.427	0.558	0.375	0.658
Row 6	0.573	0.476	0.455	0.572	0.383	0.680	0.336	0.823
Row 7	0.676	0.464	0.545	0.561	0.461	0.669	0.407	0.831
Row 8	0.583	0.601	0.475	0.705	0.405	0.819	0.353	0.960
Exit	0.701	0.439	0.577	0.585	0.494	0.746	0.437	0.945
Exit top 1	0.665	0.506	0.551	0.575	0.470	0.664	0.416	0.795
Exit top 2	0.709	0.513	0.589	0.594	0.503	0.694	0.445	0.866

Table 10. The Heat Transfer Effectiveness and the Cooling Parameter Values of the SSLSS Configuration.

Configura	II2SSLSS		II4SSLSS		II6SSLSS		II8SSLSS	
	ReD = 7505		ReD = 14792		ReD = 30298		ReD = 59340	
Paramete	ε	ξ	ε	ξ	ε	ξ	ε	ξ
Inlet row	0.391	0.543	0.280	0.540	0.234	0.626	0.199	0.729
Row 2	0.506	0.359	0.378	0.392	0.320	0.475	0.278	0.599
Row 3	0.725	0.324	0.555	0.366	0.474	0.448	0.416	0.546
Row 4	0.446	0.412	0.348	0.469	0.295	0.542	0.260	0.621
Row 5	0.577	0.506	0.457	0.587	0.385	0.676	0.336	0.788
Row 6	0.530	0.507	0.428	0.590	0.359	0.709	0.315	0.843
Row 7	0.637	0.492	0.520	0.587	0.439	0.706	0.390	0.851
Row 8	0.560	0.615	0.460	0.717	0.394	0.839	0.345	0.967
Exit	0.677	0.449	0.565	0.588	0.482	0.759	0.425	0.949
Exit top 1	0.644	0.511	0.536	0.581	0.461	0.680	0.405	0.814
Exit top 2	0.687	0.519	0.573	0.622	0.492	0.730	0.433	0.887

Table 11. The Heat Transfer Effectiveness and the Cooling Parameter Values of the SSSLS Configuration.

Configuratic	II2SSSLS		II4SSSLS		II6SSSLS		II8SSSLS	
	ReD = 7496		ReD = 14828		ReD = 30090		ReD = 60487	
Parameter:	ε	ξ	ε	ξ	ε	ξ	ε	ξ
Inlet row	0.422	0.593	0.266	0.522	0.245	0.656	0.205	0.757
Row 2	0.553	0.393	0.361	0.382	0.332	0.490	0.283	0.600
Row 3	0.793	0.341	0.530	0.359	0.490	0.455	0.423	0.532
Row 4	0.649	0.384	0.444	0.385	0.409	0.486	0.350	0.580
Row 5	0.801	0.356	0.557	0.382	0.512	0.469	0.438	0.566
Row 6	0.511	0.484	0.366	0.515	0.334	0.628	0.287	0.738
Row 7	0.627	0.604	0.454	0.650	0.412	0.791	0.356	0.957
Row 8	0.569	0.668	0.421	0.712	0.378	0.861	0.327	0.974
Exit	0.696	0.545	0.524	0.596	0.474	0.805	0.409	0.979
Exit top 1	0.664	0.562	0.499	0.602	0.450	0.699	0.385	0.840
Exit top 2	0.715	0.640	0.536	0.624	0.481	0.785	0.417	0.933

Table 12. The Heat Transfer Effectiveness and the Cooling Parameter Values of the SSSSL Configuration.

Configura	II2SSSSL		II4SSSSL		II6SSSSL		II8SSSSL	
	ReD = 7508		ReD = 15059		ReD = 30210		ReD = 61126	
Paramete	ε	ξ	ε	ξ	ε	ξ	ε	ξ
Inlet row	0.388	0.523	0.281	0.530	0.233	0.622	0.198	0.717
Row 2	0.511	0.351	0.382	0.399	0.319	0.476	0.273	0.588
Row 3	0.730	0.306	0.567	0.365	0.474	0.442	0.409	0.535
Row 4	0.596	0.353	0.473	0.402	0.397	0.479	0.345	0.573
Row 5	0.737	0.319	0.590	0.387	0.496	0.469	0.432	0.554
Row 6	0.608	0.387	0.496	0.464	0.422	0.562	0.373	0.675
Row 7	0.721	0.402	0.594	0.489	0.507	0.588	0.446	0.702
Row 8	0.482	0.603	0.401	0.674	0.347	0.770	0.300	0.867
Exit	0.607	0.630	0.507	0.738	0.440	0.899	0.378	1.083
Exit top 1	0.575	0.547	0.476	0.606	0.412	0.693	0.356	0.831
Exit top 2	0.623	0.561	0.514	0.657	0.445	0.772	0.383	0.938

Table 13. The Heat Transfer Effectiveness and the Cooling Parameter Values of the MMSSS Configuration.

Configura	II2MMSSS		II4MMSSS		II6MMSSS		II8MMSSS	
	ReD = 7463		ReD = 14749		ReD = 30646		ReD = 58868	
Paramete	ε	ξ	ε	ξ	ε	ξ	ε	ξ
Inlet row	0.288	0.597	0.214	0.615	0.185	0.733	0.157	0.829
Row 2	0.378	0.439	0.290	0.485	0.251	0.582	0.212	0.683
Row 3	0.556	0.404	0.437	0.468	0.378	0.551	0.323	0.668
Row 4	0.510	0.409	0.406	0.469	0.351	0.573	0.303	0.679
Row 5	0.624	0.364	0.506	0.434	0.434	0.558	0.379	0.641
Row 6	0.541	0.452	0.445	0.538	0.385	0.677	0.337	0.799
Row 7	0.639	0.441	0.530	0.540	0.467	0.664	0.406	0.812
Row 8	0.553	0.591	0.465	0.679	0.409	0.813	0.353	0.943
Exit	0.663	0.434	0.561	0.573	0.498	0.748	0.436	0.928
Exit top 1	0.638	0.482	0.537	0.556	0.468	0.662	0.413	0.813
Exit top 2	0.675	0.449	0.569	0.571	0.498	0.705	0.443	0.873

Table 14. The Heat Transfer Effectiveness and the Cooling Parameter Values of the SMMSS Configuration.

Configura	II2SMMSS		II4SMMSS		II6SMMSS		II8SMMSS	
	ReD = 7416		ReD = 15001		ReD = 29222		ReD = 60313	
Paramete	ε	ξ	ε	ξ	ε	ξ	ε	ξ
Inlet row	0.338	0.493	0.274	0.539	0.231	0.610	0.193	0.706
Row 2	0.369	0.378	0.305	0.442	0.257	0.507	0.216	0.616
Row 3	0.555	0.380	0.468	0.464	0.394	0.527	0.335	0.636
Row 4	0.435	0.395	0.370	0.471	0.312	0.553	0.266	0.642
Row 5	0.548	0.393	0.470	0.489	0.399	0.576	0.339	0.676
Row 6	0.495	0.457	0.426	0.556	0.365	0.664	0.312	0.794
Row 7	0.592	0.439	0.514	0.554	0.441	0.663	0.378	0.806
Row 8	0.526	0.571	0.454	0.698	0.393	0.815	0.333	0.929
Exit	0.632	0.424	0.556	0.586	0.484	0.739	0.414	0.917
Exit top 1	0.606	0.479	0.529	0.579	0.458	0.663	0.393	0.803
Exit top 2	0.643	0.448	0.566	0.575	0.487	0.721	0.419	0.856

Table 15. The Heat Transfer Effectiveness and the Cooling Parameter Values of the SSMMS Configuration.

Configura	II2SSMMS		II4SSMMS		II6SSMMS		II8SSMMS	
	ReD = 7304		ReD = 14997		ReD = 29840		ReD = 60570	
Paramete	ε	ξ	ε	ξ	ε	ξ	ε	ξ
Inlet row	0.484	0.625	0.349	0.646	0.293	0.732	0.244	0.826
Row 2	0.622	0.415	0.458	0.449	0.388	0.550	0.327	0.675
Row 3	0.878	0.330	0.659	0.391	0.568	0.469	0.494	0.569
Row 4	0.586	0.410	0.454	0.483	0.391	0.568	0.335	0.667
Row 5	0.731	0.425	0.575	0.509	0.495	0.588	0.423	0.717
Row 6	0.546	0.479	0.441	0.569	0.378	0.688	0.326	0.822
Row 7	0.648	0.468	0.529	0.569	0.456	0.676	0.396	0.839
Row 8	0.573	0.604	0.473	0.705	0.408	0.828	0.351	0.962
Exit	0.691	0.439	0.575	0.583	0.497	0.748	0.432	0.941
Exit top 1	0.656	0.510	0.547	0.569	0.474	0.669	0.412	0.806
Exit top 2	0.700	0.517	0.582	0.618	0.508	0.708	0.441	0.874

Table 16. The Heat Transfer Effectiveness and the Cooling Parameter Values of the SSSMM Configuration.

Configura	II2SSSMM		II4SSSMM		II6SSSMM		II8SSSMM	
	ReD = 7552		ReD = 14995		ReD = 30149		ReD = 59801	
Paramete	ε	ξ	ε	ξ	ε	ξ	ε	ξ
Inlet row	0.372	0.520	0.283	0.548	0.236	0.628	0.204	0.731
Row 2	0.491	0.353	0.386	0.410	0.323	0.487	0.283	0.605
Row 3	0.705	0.307	0.571	0.379	0.480	0.448	0.427	0.543
Row 4	0.578	0.349	0.476	0.407	0.402	0.480	0.358	0.581
Row 5	0.714	0.327	0.594	0.402	0.503	0.477	0.447	0.573
Row 6	0.518	0.416	0.439	0.510	0.373	0.610	0.331	0.727
Row 7	0.622	0.480	0.533	0.569	0.455	0.676	0.405	0.824
Row 8	0.495	0.614	0.424	0.713	0.363	0.819	0.319	0.932
Exit	0.615	0.526	0.531	0.666	0.456	0.836	0.401	1.030
Exit top 1	0.582	0.551	0.501	0.614	0.430	0.696	0.380	0.817
Exit top 2	0.629	0.500	0.540	0.627	0.463	0.738	0.408	0.895

Table 17. The Heat Transfer Effectiveness and the Cooling Parameter Values of the MSMSS Configuration.

Configura	II2MSMSS		II4MSMSS		II6MSMSS		II8MSMSS	
	ReD = 7304		ReD = 14997		ReD = 29840		ReD = 60570	
Paramete	ε	ξ	ε	ξ	ε	ξ	ε	ξ
Inlet row	0.310	0.630	0.224	0.649	0.188	0.735	0.156	0.829
Row 2	0.483	0.418	0.356	0.451	0.302	0.552	0.255	0.677
Row 3	0.681	0.333	0.512	0.393	0.442	0.471	0.385	0.571
Row 4	0.501	0.412	0.389	0.485	0.335	0.569	0.287	0.668
Row 5	0.625	0.427	0.493	0.511	0.424	0.590	0.363	0.718
Row 6	0.554	0.478	0.447	0.569	0.383	0.688	0.330	0.822
Row 7	0.657	0.467	0.536	0.569	0.463	0.676	0.401	0.839
Row 8	0.573	0.604	0.473	0.705	0.408	0.828	0.351	0.962
Exit	0.691	0.439	0.575	0.583	0.497	0.748	0.432	0.941
Exit top 1	0.656	0.510	0.547	0.569	0.474	0.669	0.412	0.806
Exit top 2	0.700	0.517	0.582	0.618	0.507	0.708	0.441	0.874

Table 18. The Heat Transfer Effectiveness and the Cooling Parameter Values of the MSSMS Configuration.

Configura	II2MSSMS		II4MSSMS		II6MSSMS		II8MSSMS	
	ReD = 7433		ReD = 14957		ReD = 30211		ReD = 60618	
Paramete	ε	ξ	ε	ξ	ε	ξ	ε	ξ
Inlet row	0.292	0.587	0.223	0.646	0.187	0.739	0.155	0.818
Row 2	0.468	0.424	0.355	0.460	0.300	0.552	0.252	0.665
Row 3	0.695	0.426	0.514	0.400	0.440	0.470	0.376	0.566
Row 4	0.605	0.412	0.449	0.448	0.385	0.532	0.331	0.630
Row 5	0.744	0.369	0.557	0.431	0.479	0.507	0.410	0.613
Row 6	0.544	0.465	0.424	0.549	0.364	0.654	0.314	0.776
Row 7	0.646	0.486	0.513	0.608	0.441	0.721	0.382	0.878
Row 8	0.569	0.606	0.462	0.713	0.396	0.832	0.340	0.953
Exit	0.687	0.444	0.565	0.593	0.486	0.758	0.421	0.934
Exit top 1	0.655	0.514	0.541	0.588	0.463	0.679	0.399	0.801
Exit top 2	0.699	0.513	0.580	0.618	0.495	0.731	0.426	0.886

Table 19. The Heat Transfer Effectiveness and the Cooling Parameter Values of the MSSSM Configuration.

Configura	II2MSSSM		II4MSSSM		II6MSSSM		II8MSSSM	
	ReD = 7482		ReD = 14991		ReD = 29878		ReD = 59679	
Paramete	ε	ξ	ε	ξ	ε	ξ	ε	ξ
Inlet row	0.316	0.639	0.232	0.656	0.190	0.734	0.161	0.829
Row 2	0.492	0.423	0.371	0.454	0.305	0.551	0.263	0.674
Row 3	0.697	0.336	0.533	0.403	0.445	0.477	0.393	0.573
Row 4	0.591	0.384	0.462	0.457	0.393	0.528	0.344	0.640
Row 5	0.721	0.349	0.576	0.432	0.487	0.506	0.429	0.611
Row 6	0.607	0.426	0.497	0.510	0.420	0.616	0.372	0.754
Row 7	0.715	0.428	0.587	0.535	0.502	0.623	0.445	0.771
Row 8	0.542	0.608	0.453	0.699	0.385	0.806	0.337	0.933
Exit	0.663	0.531	0.566	0.649	0.477	0.825	0.421	1.030
Exit top 1	0.628	0.512	0.528	0.591	0.454	0.651	0.399	0.793
Exit top 2	0.673	0.525	0.570	0.622	0.485	0.729	0.429	0.883

Table 20. The Heat Transfer Effectiveness and the Cooling Parameter Values of the SMSMS Configuration.

Configura	II2SMSMS		II4SMSMS		II6SMSMS		II8SMSMS	
	ReD = 7392		ReD = 15124		ReD = 30111		ReD = 59924	
Paramete	ε	ξ	ε	ξ	ε	ξ	ε	ξ
Inlet row	0.395	0.555	0.289	0.569	0.239	0.641	0.200	0.727
Row 2	0.420	0.397	0.319	0.449	0.265	0.530	0.223	0.633
Row 3	0.618	0.381	0.480	0.457	0.404	0.544	0.346	0.654
Row 4	0.548	0.391	0.435	0.450	0.369	0.531	0.320	0.633
Row 5	0.677	0.364	0.544	0.432	0.461	0.522	0.399	0.614
Row 6	0.511	0.460	0.417	0.551	0.358	0.659	0.310	0.781
Row 7	0.613	0.512	0.505	0.608	0.435	0.726	0.377	0.877
Row 8	0.551	0.602	0.456	0.714	0.393	0.835	0.338	0.949
Exit	0.663	0.448	0.558	0.600	0.485	0.761	0.420	0.931
Exit top 1	0.640	0.503	0.531	0.594	0.461	0.688	0.398	0.805
Exit top 2	0.680	0.476	0.568	0.605	0.494	0.715	0.426	0.871

Table 21. The Heat Transfer Effectiveness and the Cooling Parameter Values of the SMSSM Configuration.

Configura	II2SMSSM		II4SMSSM		II6SMSSM		II8SMSSM	
	ReD = 7458		ReD = 15020		ReD = 30065		ReD = 60523	
Paramete	ε	ξ	ε	ξ	ε	ξ	ε	ξ
Inlet row	0.398	0.553	0.289	0.541	0.241	0.638	0.203	0.732
Row 2	0.425	0.405	0.326	0.462	0.267	0.534	0.227	0.642
Row 3	0.630	0.391	0.512	0.505	0.410	0.540	0.353	0.646
Row 4	0.561	0.400	0.464	0.476	0.373	0.535	0.323	0.642
Row 5	0.693	0.358	0.583	0.449	0.466	0.517	0.405	0.612
Row 6	0.592	0.432	0.503	0.543	0.410	0.628	0.357	0.760
Row 7	0.701	0.426	0.602	0.539	0.492	0.627	0.431	0.763
Row 8	0.535	0.614	0.458	0.701	0.381	0.812	0.330	0.927
Exit	0.654	0.524	0.561	0.619	0.473	0.826	0.412	1.017
Exit top 1	0.626	0.503	0.532	0.580	0.450	0.666	0.389	0.797
Exit top 2	0.669	0.495	0.569	0.604	0.483	0.728	0.419	0.883

Table 22. The Heat Transfer Effectiveness and the Cooling Parameter Values of the SSMSM Configuration.

Configura	II1SSMSM		II2SSMSM		II3SSMSM		II4SSMSM		II5SSMSM		II6SSMSM		II7SSMSM		II8SSMSM		II9SSMSM	
	ReD = 5062		ReD = 7457		ReD = 10604		ReD = 15004		ReD = 21386		ReD = 30362		ReD = 42362		ReD = 59519		ReD = 66231	
Paramete	ε	ξ	ε	ξ	ε	ξ	ε	ξ	ε	ξ	ε	ξ	ε	ξ	ε	ξ	ε	ξ
Inlet row	0.445	0.508	0.395	0.547	0.322	0.539	0.283	0.546	0.263	0.594	0.242	0.644	0.225	0.699	0.205	0.740	0.199	0.755
Row 2	0.582	0.329	0.519	0.367	0.436	0.385	0.386	0.403	0.356	0.443	0.331	0.497	0.309	0.554	0.284	0.610	0.278	0.632
Row 3	0.818	0.267	0.740	0.305	0.632	0.336	0.566	0.363	0.525	0.393	0.490	0.446	0.461	0.492	0.418	0.563	0.419	0.560
Row 4	0.571	0.370	0.516	0.393	0.448	0.421	0.403	0.456	0.374	0.487	0.350	0.534	0.329	0.574	0.311	0.612	0.300	0.635
Row 5	0.724	0.364	0.653	0.402	0.571	0.443	0.517	0.490	0.478	0.525	0.448	0.571	0.418	0.623	0.392	0.681	0.381	0.704
Row 6	0.632	0.413	0.571	0.439	0.507	0.479	0.462	0.527	0.428	0.571	0.399	0.642	0.377	0.711	0.351	0.754	0.344	0.771
Row 7	0.752	0.400	0.677	0.445	0.607	0.491	0.558	0.537	0.513	0.590	0.482	0.648	0.456	0.712	0.426	0.772	0.415	0.800
Row 8	0.576	0.557	0.524	0.616	0.475	0.665	0.436	0.703	0.402	0.755	0.377	0.822	0.354	0.882	0.329	0.927	0.321	0.948
Exit	0.700	0.468	0.643	0.528	0.590	0.595	0.542	0.655	0.499	0.736	0.470	0.837	0.444	0.931	0.410	1.019	0.403	1.056
Exit top 1	0.668	0.478	0.617	0.502	0.559	0.542	0.511	0.580	0.471	0.616	0.445	0.672	0.421	0.731	0.389	0.800	0.379	0.831
Exit top 2	0.716	0.459	0.658	0.500	0.597	0.578	0.548	0.616	0.503	0.673	0.479	0.740	0.450	0.817	0.418	0.895	0.408	0.928

Table 23. The Heat Transfer Effectiveness and the Cooling Parameter Values of the PPLPP Configuration.

Configura	II2PPLPP		II4PPLPP		II6PPLPP		II8PPLPP	
	ReD = 7394		ReD = 15002		ReD = 29504		ReD = 59569	
Paramete	ε	ξ	ε	ξ	ε	ξ	ε	ξ
Inlet row	0.385	0.550	0.274	0.539	0.236	0.632	0.208	0.765
Row 2	0.517	0.369	0.375	0.389	0.327	0.485	0.293	0.628
Row 3	0.728	0.295	0.546	0.345	0.481	0.441	0.438	0.534
Row 4	0.416	0.442	0.321	0.484	0.281	0.570	0.249	0.664
Row 5	0.551	0.541	0.426	0.627	0.371	0.725	0.327	0.843
Row 6	0.527	0.532	0.416	0.593	0.362	0.706	0.321	0.846
Row 7	0.638	0.480	0.507	0.590	0.443	0.697	0.390	0.855
Row 8	0.576	0.635	0.461	0.724	0.406	0.839	0.353	0.980
Exit	0.688	0.438	0.564	0.590	0.495	0.732	0.439	0.923
Exit top 1	0.660	0.486	0.541	0.563	0.472	0.668	0.412	0.820
Exit top 2	0.700	0.461	0.573	0.599	0.501	0.701	0.441	0.875

Table 24. The Heat Transfer Effectiveness and the Cooling Parameter Values of the PPLSS Configuration.

Configura	II2PPLSS		II4PPLSS		II6PPLSS		II8PPLSS	
	ReD = 7471		ReD = 14982		ReD = 29532		ReD = 59113	
Paramete	ε	ξ	ε	ξ	ε	ξ	ε	ξ
Inlet row	0.431	0.525	0.312	0.526	0.262	0.601	0.233	0.728
Row 2	0.575	0.346	0.427	0.375	0.360	0.447	0.326	0.587
Row 3	0.807	0.287	0.619	0.334	0.510	0.452	0.481	0.512
Row 4	0.464	0.403	0.364	0.462	0.319	0.528	0.278	0.625
Row 5	0.608	0.516	0.482	0.611	0.419	0.680	0.364	0.803
Row 6	0.532	0.503	0.433	0.582	0.371	0.695	0.326	0.827
Row 7	0.640	0.505	0.527	0.591	0.454	0.698	0.401	0.840
Row 8	0.553	0.614	0.455	0.720	0.393	0.841	0.343	0.964
Exit	0.667	0.459	0.556	0.609	0.486	0.770	0.424	0.962
Exit top 1	0.639	0.505	0.532	0.580	0.457	0.708	0.401	0.826
Exit top 2	0.679	0.492	0.566	0.608	0.494	0.704	0.430	0.876

Table 25. The Thermal Effectiveness and the Cooling Parameter Values of the PSLSS Configuration.

Configura	II2PSLSS		II4PSLSS		II6PSLSS		II8PSLSS	
	ReD = 7371		ReD = 14971		ReD = 29920		ReD = 58799	
Paramete	ε	ξ	ε	ξ	ε	ξ	ε	ξ
Inlet row	0.422	0.482	0.330	0.522	0.274	0.592	0.238	0.704
Row 2	0.475	0.344	0.378	0.384	0.320	0.461	0.277	0.586
Row 3	0.694	0.323	0.553	0.327	0.471	0.403	0.419	0.541
Row 4	0.445	0.402	0.350	0.469	0.298	0.545	0.270	0.624
Row 5	0.582	0.489	0.465	0.593	0.396	0.680	0.350	0.791
Row 6	0.518	0.502	0.423	0.581	0.361	0.698	0.320	0.823
Row 7	0.625	0.497	0.518	0.583	0.443	0.699	0.391	0.844
Row 8	0.546	0.602	0.452	0.718	0.389	0.838	0.340	0.960
Exit	0.655	0.453	0.550	0.607	0.479	0.768	0.423	0.944
Exit top 1	0.634	0.469	0.533	0.584	0.452	0.690	0.402	0.811
Exit top 2	0.669	0.491	0.574	0.562	0.481	0.738	0.427	0.886

Table 26. The Thermal Effectiveness and the Cooling Parameter Values of the PSLSP Configuration.

Configura	II2PSLSP		II4PSLSP		II6PSLSP		II8PSLSP	
	ReD = 7396		ReD = 15014		ReD = 29938		ReD = 59464	
Paramete	ε	ξ	ε	ξ	ε	ξ	ε	ξ
Inlet row	0.413	0.513	0.307	0.522	0.263	0.618	0.226	0.726
Row 2	0.465	0.365	0.354	0.399	0.305	0.484	0.264	0.600
Row 3	0.677	0.335	0.530	0.362	0.452	0.444	0.397	0.550
Row 4	0.431	0.426	0.339	0.481	0.291	0.550	0.255	0.638
Row 5	0.565	0.528	0.449	0.597	0.380	0.702	0.332	0.805
Row 6	0.506	0.516	0.401	0.618	0.346	0.721	0.300	0.843
Row 7	0.609	0.508	0.495	0.609	0.423	0.724	0.368	0.863
Row 8	0.571	0.636	0.464	0.716	0.401	0.844	0.346	0.963
Exit	0.689	0.427	0.567	0.565	0.493	0.738	0.428	0.911
Exit top 1	0.660	0.492	0.538	0.592	0.467	0.687	0.406	0.815
Exit top 2	0.703	0.466	0.576	0.589	0.499	0.719	0.433	0.867

Table 27. The Thermal Effectiveness and the Cooling Parameter Values of the PSLMP Configuration.

Configura	II2PSLMP		II4PSLMP		II6PSLMP		II8PSLMP	
	ReD = 7481		ReD = 14880		ReD = 29466		ReD = 59574	
Paramete	ε	ξ	ε	ξ	ε	ξ	ε	ξ
Inlet row	0.440	0.484	0.331	0.500	0.277	0.571	0.238	0.678
Row 2	0.492	0.334	0.379	0.368	0.320	0.440	0.278	0.555
Row 3	0.712	0.300	0.558	0.352	0.469	0.394	0.414	0.518
Row 4	0.450	0.402	0.359	0.446	0.301	0.512	0.265	0.594
Row 5	0.592	0.498	0.474	0.557	0.397	0.651	0.345	0.750
Row 6	0.464	0.517	0.374	0.599	0.317	0.695	0.275	0.817
Row 7	0.571	0.540	0.466	0.639	0.393	0.753	0.345	0.900
Row 8	0.549	0.642	0.451	0.713	0.382	0.840	0.328	0.966
Exit	0.670	0.436	0.553	0.571	0.475	0.732	0.415	0.914
Exit top 1	0.634	0.517	0.525	0.600	0.451	0.703	0.395	0.806
Exit top 2	0.676	0.505	0.562	0.612	0.483	0.730	0.421	0.885

Table 28. The Heat Transfer Effectiveness and the Cooling Parameter Values of the PSLPM Configuration.

Configura	II2PSLPM		II4PSLPM		II6PSLPM		II8PSLPM	
	ReD = 7366		ReD = 15075		ReD = 29459		ReD = 59546	
Paramete	ε	ξ	ε	ξ	ε	ξ	ε	ξ
Inlet row	0.462	0.477	0.332	0.486	0.286	0.574	0.247	0.683
Row 2	0.517	0.332	0.383	0.372	0.331	0.447	0.288	0.560
Row 3	0.748	0.303	0.569	0.369	0.492	0.428	0.423	0.542
Row 4	0.471	0.406	0.370	0.466	0.317	0.525	0.276	0.599
Row 5	0.622	0.483	0.492	0.569	0.420	0.637	0.348	0.888
Row 6	0.601	0.478	0.483	0.545	0.407	0.640	0.374	0.754
Row 7	0.721	0.455	0.583	0.548	0.495	0.649	0.451	0.774
Row 8	0.533	0.617	0.439	0.712	0.376	0.827	0.333	0.938
Exit	0.656	0.525	0.543	0.663	0.470	0.836	0.421	1.022
Exit top 1	0.619	0.519	0.513	0.585	0.441	0.683	0.398	0.791
Exit top 2	0.665	0.509	0.550	0.625	0.475	0.744	0.425	0.903

Table 29. The Heat Transfer Effectiveness and the Cooling Parameter Values of the PMLPM Configuration.

Configura	II2PMLPM		II4PMLPM		II6PMLPM		II8PMLPM	
	ReD = 7418		ReD = 15075		ReD = 29459		ReD = 59546	
Paramete	ε	ξ	ε	ξ	ε	ξ	ε	ξ
Inlet row	0.393	0.462	0.290	0.487	0.251	0.575	0.216	0.684
Row 2	0.446	0.337	0.335	0.373	0.290	0.448	0.252	0.561
Row 3	0.661	0.342	0.498	0.370	0.431	0.429	0.370	0.543
Row 4	0.419	0.405	0.324	0.467	0.277	0.526	0.241	0.600
Row 5	0.548	0.467	0.431	0.571	0.368	0.638	0.304	0.889
Row 6	0.525	0.476	0.423	0.546	0.356	0.641	0.327	0.755
Row 7	0.628	0.452	0.510	0.549	0.434	0.650	0.395	0.776
Row 8	0.530	0.611	0.440	0.712	0.376	0.827	0.333	0.938
Exit	0.652	0.517	0.544	0.663	0.470	0.836	0.421	1.022
Exit top 1	0.614	0.518	0.514	0.585	0.441	0.683	0.398	0.791
Exit top 2	0.659	0.506	0.551	0.625	0.475	0.744	0.425	0.903

Table 30. The Heat Transfer Effectiveness and the Cooling Parameter Values of the PMLPL Configuration.

Configura	II2PMLPL		II4PMLPL		II6PMLPL		II8PMLPL	
	ReD = 7450		ReD = 14882		ReD = 30060		ReD = 58936	
Paramete	ε	ξ	ε	ξ	ε	ξ	ε	ξ
Inlet row	0.472	0.424	0.384	0.488	0.314	0.541	0.266	0.625
Row 2	0.418	0.322	0.346	0.394	0.286	0.449	0.245	0.560
Row 3	0.636	0.367	0.532	0.420	0.438	0.505	0.385	0.598
Row 4	0.463	0.382	0.386	0.462	0.322	0.525	0.280	0.616
Row 5	0.600	0.435	0.505	0.546	0.420	0.628	0.366	0.725
Row 6	0.587	0.450	0.502	0.540	0.420	0.637	0.369	0.773
Row 7	0.703	0.425	0.603	0.531	0.508	0.638	0.447	0.791
Row 8	0.506	0.599	0.441	0.714	0.370	0.826	0.324	0.944
Exit	0.630	0.550	0.549	0.649	0.466	0.824	0.413	1.018
Exit top 1	0.589	0.522	0.519	0.574	0.438	0.672	0.384	0.816
Exit top 2	0.634	0.527	0.555	0.620	0.470	0.746	0.416	0.909

REFERENCES

[1] Sheikhmohamed,A.A., Soma, L.W., and Ames, F.E., 2017, "Heat transfer and Pressure Drop Measurements In a High Solidity Pin Fin Array with Variable Hole Size Incremental Impingement" ASME Paper No. GT2017-65046.

[2] Mitch L.Bushe, Leolein P.Moualeu, Natis Chowdhury, Clement Tang and Forrest E.Ames, 2012, " Heat Transfer and Pressure Drop Measurements in High Solidity Pin Fin Cooling Array with Incremental Replenishment" ASME Journal of Turbomachinery, Vol 135, Paper No.GT2012-69289

[3] F. E. Ames and L. A. Dvorak, 2005, "Turbulent Transport in Pin Fin Array: Experimental Data and Predictions" ASME Journal of Turbomachinery, Vol 128, Paper No.GT2005-68180

[4] Forrest E. Ames, Chad Norquist and Lindsay A.Dvorak ,2007, " Endwall Heat Transfer Measurements in A Staggered Pin Fin Array with an Adiabatic Pin" ASME PAPER NO. GT2007-27432

[5] F. E. Ames, L. A. Dvorak and M. J. Morrow,2005, " Turbulent Augmentation of Internal Convection Over Pins In Staggered-Pin Fin Array" ASME Journal of Turbomachinery, Vol 127, paper No. 2004-GT-53889

[6] B. A.Brigham and G.J.Vanfossan, 1983, "Length to Diameter Ratio and Row Number Effect of Short Pin Fin Heat Transfer", ASME, Journal of Engineer for Gas Turbine and Power, Vol 106, Paper No.241-244

[7] M.K.Chyu, 1989, " Heat Transfer and Pressure Drop For Short Pin-Fin Arrays with Pin-Endwall Fillet" ASME, Paper No.89-GT-99

[8] A.B.Jubran, M.A Hamdan and R.M. Abdualh,1993 "Enhanced Heat Transfer, Missing Pin, and Optimization for Cylindrical Pin Fin Arrays", ASME, Vol 115, Paper No.576-583

[9] R.D.V Prasad, G.Narasa Raju, M.S.Ssrinivisa Roa and Vasudeva Roa,2013 "Steady State Thermal & Structural Analysis of Gas Turbine Blade Cooling Systems", International Journal of Engineering and Research & Technology, Vol 2, ISSN:2278-0181

[10] G.J.Vanfossen,1981, "Heat Transfer Coefficient for Staggered Array of Short Pin Fins" ASME, Paper No.81-GT-75

[11] I. Jaswal and F. E. Ames, 2009,"Heat Transfer and Pressure Drop Measurements in Constant and Converging Section Pin and Diamond Pedestal Arrays" ASME Journal of Thermal Science, Vol 3, Paper No.GT2009-59834

[12] D.M.Kercher and W.Tabakoff,1970, “Heat Transfer by a Square Array of Round Air Jets Impinging a Perpendicular to a Flat Surface Including the Effect of Spent Air”,ASME, Journal of Ingineering for Power, Vol 92,Paper No.73-92

[13] D.E.Metzger and R.J.Korstad,1971, “Effects of Crossflow on Impingement Heat Transfer” ASME paper No.71-GT-1

[14] Mats O Annerfeldt and Johan L Persson, 2001, “Experimental Investigation of Impingement Cooling With Tabulators Or Surface Enlargement Elements”. ASME Paper No. 2001-GT-0149

[15] L.W.Florschuetz, D.E.Metzger and C.C. Su,1983, “Heat Transfer Characteristics for Jet Impingement With Initial Crossflow” ASME Paper No.83-GT-28

[16] R.A.A. Abdul Hussain and G.E. Andrews,1991,“ Enhanced Full Coverage Impingement Heat Transfer With Obstacles in the Gap” ASME Paper No. 91-GT-346

[17] G.E.Andrews , R.A.A.Abdul Hussain and M.C.M Kpadi,2004, “ Enhanced Impingement Heat Transfer: The Influence of Impingement X/D For Interrupted Rib Obstacles (Rectangular Pin Fin)” Energy and Resource Research Institute School of Process, Environment and Material Engineering of The University Of Leeds, UK

[18] M.K.Chyu, Y.C.Hsing, T.I. Shih and V.Natarjan,1998, “Heat Transfer Contribution of Pins and Endwall in Pin-Fin Arrays:Effect of Thermal Boundary Condition Modeling”,ASME,Vol 4, Paper No.98-GT-175

[19] D.E.Mestzger, W.B.Shepard and S. W.Haley, 1986,“Row Resolved Heat Transfer Variations in Pin-Fin Array Including the Effect of Non-Uniform Arrays and Flow Convergence”,ASME, Paper No. 86-GT-132

[20] Susheel Singh, Sumanta Acharya and Forres E. Ames, 2017, “Numerical Investigation of Local Cooling Enhancement Using Pin-Finned Channel with Incremental Impingement”, ESME, Journal of Turbomachinery, Paper No. GT2017-65083

[21] Changmin Son, David Gillespie , Peter Ireland and Geoffrey M. Dailey, 2001, “ Heat Transfer and Flow Characteristics of an Engine Representative Impingement Cooling System”,ASME, Journal Turbomachinery, Vol 123, Paper No.154-160

[22] Susheel Singh et al, 2016, “Effect of Inlet Flow condition on Heat Transfer in Pin-Fin cooling Configuration”, AIAA SciTech,4-8 January, San Diego, CA,AIAA Paper No.2329665.

[23] F. E. Ames and L. A. Dvorak, 2006, "The Influence of Reynolds Number and Row Position on Surface Pressure Distributions In Staggered Pin Fin Arrays," ASME Paper No. GT2006-90170.

[24] Jeffrey Armstrong and David Winstanley,1988, “A Review of Staggered Pin Fin Array Heat Transfer for Turbine Cooling Applications” ASME Journal of Turbomachinery, Vol 110, PP 94-103.